

Dating circulations of hydrothermal fluids in the crystalline basements of unconformity-related metal deposits using *in situ* Rb/Sr geochronology : proof of concept

Quentin Boulogne^{1,2*}, Gaétan Milesi^{1,2}, Chantal Peiffert¹, Emmy Fischer^{1,2}, Christophe Ballouard¹, Mehdi Serdoun^{1,3}, Thomas Obin^{1,2}, Andreï Lecomte¹, Pierre Martz³, Andrew Kaczowka⁴ and Julien Mercadier^{1,2}

¹Université de Lorraine, CNRS, GeoRessources, F-54000 Nancy, France

²LabCom CREGU, GeoRessources, CNRS, Université de Lorraine, Vandœuvre-lès-Nancy, France

³Orano Canada, Saskatoon, Canada

⁴Cameco Corporation, Saskatoon, Canada

Correspondence to: Quentin Boulogne (quentin.boulogne@univ-lorraine.fr)

Abstract. The use of *in situ* Rb–Sr geochronology has boomed in recent years following its implementation using LA-ICP-MS/MS technology, which enables fast, *in situ* analyses at the micron scale on selected minerals. The Rb–Sr geochronometer applied to micas is now commonly used to date the crystallization or cooling of metamorphic and magmatic rocks, based on the assumptions of a closed isotope system after passing the closure temperature and of a homogeneous Sr isotopic composition at the time of crystallization. *In situ* Rb–Sr geochronology applied to micas and related alteration products in geological contexts involving hydrothermal fluid circulation affecting micas after crystallization could provide a new way to decipher the timing and duration of fluid circulation in various settings such as mountain belts or sedimentary basins. The behavior and applicability of the Rb–Sr system in such contexts are, however, poorly understood, as the system may be partially reopened with differential redistribution of Rb and Sr at the grain scale. To test this hypothesis, we selected a case study related to unconformity-related U deposits from the Athabasca Basin (Canada), which formed through intense hydrothermal fluid circulation at the interface between crystalline basement and siliciclastic sedimentary rocks and represent archetypes of unconformity-related metal deposits. Muscovite grains from metamorphic and magmatic rocks were targeted across a range of alteration states, from hydrothermally unaltered to strongly altered domains. We focused on a specific hydrothermal alteration linked to the formation of hydrothermal illite and sudoite at the expense of metamorphic or magmatic minerals. In unaltered zones, muscovite displays variable but high Rb/Sr ratios, whereas the ⁸⁷Sr/⁸⁶Sr intercepts derived from Rb–Sr regressions are scattered and are not interpreted as meaningful initial isotopic compositions. The resulting ages range from ca. 1870 to ca. 1720 Ma and are consistent with the geological context. In distal-to-proximal alteration halos of U deposits, muscovite and related alteration products yield lower ⁸⁷Rb/⁸⁶Sr ratios and highly variable regression intercepts. The mean age calculated across the different samples and investigated sites clusters around ~1640 Ma, a value previously obtained by Ar–Ar geochronology on illite

35 and U–Pb geochronology on other hydrothermal phases and proposed to correspond to a major hydrothermal event
36 linked to a geodynamic reorganization affecting the Canadian Shield at the circum-Laurentian scale. The ~1640
37 Ma age is geologically meaningful in the studied context and is interpreted as reflecting partial, micrometric-scale
38 resetting of the Rb–Sr system in muscovite during this hydrothermal event. The wide range of regression intercept
39 values commonly observed in disturbed Rb–Sr systems is interpreted as an apparent result of open-system
40 behavior, reflecting partial system reopening and non-conservative redistribution of Rb and Sr at the grain scale,
41 rather than as a physically meaningful initial isotopic composition. These results demonstrate that detailed analysis
42 of Rb–Sr system perturbations in altered muscovite and related alteration products can constrain the timing of
43 ancient hydrothermal activity and the spatial dynamics of fluid-rock interaction. This approach provides a valuable
44 complement to conventional fluid-tracing methods and opens new perspectives for reconstructing paleo-
45 hydrothermal systems in ancient basement terrains.

46 Key words: Rb–Sr geochronology, Muscovite alteration, Hydrothermal fluid circulation, Athabasca Basin, *In situ*
47 LA-ICP-MS/MS, Isotopic resetting

48 **1. Introduction**

49 Crystalline basements are environments in which multiple types of fluids can circulate over geological timescales,
50 depending on the conditions under which these basements formed and later evolved. These fluids may originate
51 from highly diverse sources (magmatic, metamorphic, basin-derived, meteoric, etc.) and display a wide range of
52 physicochemical properties and compositions. Their circulation is primarily driven by first-order geological
53 processes (geodynamic, tectonic, sedimentological, etc.) and is considered to be largely controlled by structural
54 networks, particularly faults, that enhance permeability and enable surface-derived fluids, for instance, to reach
55 depths of several kilometers. Beyond faults and their associated damage zones, fluids may also migrate through
56 broader networks of inherited microfractures and permeable structures within crystalline rocks (e.g., Sibson, 1990;
57 Faulkner et al., 2010; Viswanathan et al., 2022). These fluids can remain stored for millions of years and may be
58 mobilized and/or mixed in response to changes in mechanical conditions (e.g., Anders et al., 2014; Frey et al.,
59 2022). They interact in various ways with the lithologies and mineral assemblages of the basement, inducing
60 mineralogical, chemical, and/or isotopic modifications that may ultimately lead to the formation of various
61 resources such as metal deposits or reservoirs of geothermal waters and metal-rich brines (e.g., Etheridge et al.,
62 1983; Yardley, 1983). Over the past decades, scientific studies have demonstrated, contrary to earlier assumptions,
63 that crystalline basements represent favorable environments for fluid circulation and storage (e.g., Juhász et al.,
64 2002; Walter et al., 2018).

65 Fluids therefore play a key role in the evolution of crystalline basements, and it is of major scientific importance
66 to identify and date the various episodes of fluid circulation in these environments (e.g., Sibson, 1990; Holness,
67 2000; Yardley and Bodnar, 2014). Radiometric dating represents a first-order challenge in such contexts, where
68 multiple fluid types may have circulated successively through the same zone in response to large-scale (tectonic)
69 or local-scale (fault-related) geological changes (e.g., Rasmussen et al., 2023; Saito et al., 2018; Weinberg et al.,
70 2020). Each fluid-flow event can leave specific mineralogical markers, often small in size and intermixed with
71 pre-existing minerals. Isotopic dating is also challenging due to the presence of inherited minerals and initial
72 isotopic signatures within the basement, which must be distinguished from those specifically related to each fluid
73 episode (e.g., Dodson, 1973; Grand’Homme et al., 2016). Significant advances have been achieved through the

74 development and application of *in situ* U–Pb dating of hydrothermal minerals (phosphates, titanium oxides,
75 carbonates, etc.) (e.g., Rasmussen et al., 2001; Rasmussen et al., 2006; Davis et al., 2011; Rabiei et al., 2017;
76 Adlakha and Hattori, 2021). Recent methodological developments in K–Ar dating of clay minerals emphasize the
77 systematic separation of multiple grain-size fractions, combined with detailed mineralogical, crystallographic, and
78 polytype characterization (1Md-1M vs. 2M1 illite), in order to deconvolve mixed detrital and authigenic illite
79 populations and extract meaningful age information related to distinct crystallization or recrystallization events
80 (e.g., Reynolds and Thomson, 1993; Velde and Christophe, 1996; Clauer et al., 1997; Hueck et al., 2022; Gerardin
81 et al., 2024). Such an integrated K–Ar-polytype approach has notably been applied to fault gouges, where dating
82 different clay fractions allows the timing of synkinematic hydrothermal fluid-faulting episodes to be constrained,
83 thereby resolving the temporal evolution of brittle deformation and fluid circulation in fault-controlled
84 hydrothermal systems (e.g., Aldega et al., 2019; Campanha et al., 2026; Schmitz et al., 2025). A limitation of this
85 approach lies in the fact that these minerals are accessory phases, generally present in limited quantities and/or at
86 small spatial scales, which creates difficulties in targeting and identification and often requires the use of costly
87 and time-intensive microscopic techniques, or that they are restricted to specific lithologies or structural contexts.

88 The development of *in situ* Rb–Sr geochronology over the past decade has led to a resurgence of interest in the
89 use of micas and feldspars as chronometers in crystalline basements, where they are ubiquitous (e.g., Gyomlai et
90 al., 2023; Jegal et al., 2022; Młynarska et al., 2024; Muñoz-Montecinos et al., 2024). Several studies have
91 demonstrated the relevance of this approach for dating magmatic (e.g., Larsen and Sundvoll, 2008; Tichomirowa
92 et al., 2019; Scott Anderson et al., 2015; Bevan et al., 2021) or metamorphic (e.g., Jenkin et al., 2001; Willigers et
93 al., 2004; Eberlei et al., 2015) events responsible for the crystallization of these minerals, as well as for dating
94 subsequent thermal and/or fluid-related events that affected these primary minerals after their formation, such as
95 in the context of hydrothermal gold deposits (Olierook et al., 2020; Liebmann et al., 2022; Ribeiro et al., 2023a,
96 b; Qiu et al., 2024). These pioneering studies have suggested that the Rb–Sr chronometer may be partially to
97 completely reset within inherited minerals during post-crystallization fluid and/or thermal events. Furthermore,
98 this approach could allow direct dating of hydrothermal circulations affecting basement environments using
99 metamorphic and/or magmatic minerals and their alteration products.

100 The objective of this contribution is to test this hypothesis in the context of paleo-hydrothermal systems developed
101 at the interface between a crystalline basement and a sedimentary basin. These systems have generated, throughout
102 Earth history, metal deposits of various commodities such as Pb, Zn, Cu, U, F, and Ba (e.g., Boiron et al., 2010;
103 Cathelineau et al., 2012; Oummouch et al., 2017). The case study focuses on the unconformity-related uranium
104 deposits of the Athabasca Basin (Saskatchewan, Canada), which host the world’s highest-grade uranium deposits.
105 These deposits have been the subject of intensive scientific research for over sixty years, and much is known about
106 the typology, age, and geological context of the associated alterations and mineralization. Uranium mineralization
107 formed during hydrothermal episodes that postdated basin deposition and was active in both basin and basement
108 settings. These events led to the formation of localized zones of clay-rich alteration, mainly illite and chlorite,
109 surrounding the orebodies, and are thought to result from interactions between host rocks and evaporitic brines
110 derived from the basin. Although the formation mechanisms are broadly similar to those responsible for other
111 unconformity-related metalliferous deposits worldwide, the interpretation of geochronological data in such long-
112 lived and overprinted hydrothermal systems remains problematic. Existing chronometers commonly yield complex
113 or equivocal age signatures that do not directly correspond to discrete alteration events. This persistent challenge

114 underscores the need to evaluate alternative mineral-isotope system, such as Rb–Sr signatures recorded by
115 basement micas and related hydrothermal products, to more accurately constrain the chronology of alteration
116 associated with the uranium mineralization.

117 **2. Geological settings**

118 **2.1. Geological history of the Wollaston-Mudjatik Transition Zone**

119 The Athabasca Basin unconformably overlies the Archean to Paleoproterozoic basement rocks known as the
120 Western Churchill Structural Province (WSP). The WSP is divided into two lithostructural subprovinces: the Rae
121 Subprovince to the west and the Hearne Subprovince to the east (Annesley et al., 2005) (Fig. 1A). The Trans-
122 Hudson Orogeny (THO), which represents a major Paleoproterozoic belt, is linked to the collision between the
123 Rae, Hearne, and Superior cratons. The beginning of this orogeny is characterized by the amalgamation between
124 1920 and 1840 Ma of the Rae and Hearne cratons, leading to the formation of the Western Churchill Structural
125 Province (WSP) and to an oceanic arc in the Manikewan Ocean (Ansdell, 2005; Corrigan, 2012; Corrigan et al.,
126 2005, 2009). The gradual closure of the Manikewan Ocean led to the successive accretion of juvenile crustal
127 segments between 1880 and 1860 Ma. The final stage of the THO resulted in the complete closure of the
128 Manikewan Ocean and in the continental collision between the margin of the Hearne craton bordered by the
129 accreted juvenile arcs and the northern edge of the Superior craton between 1830 and 1800 Ma (Corrigan et al.,
130 2009). Finally, the latter stages of THO deformation are marked by the emplacement at ca. 1800 and 1720 Ma of
131 pegmatites and aplites, in relation to sinistral deformation along shear bands in a transpressional context (e.g.,
132 Chiarenzelli, 1989; Bickford et al., 1990; Chiarenzelli et al., 1998; Bickford et al., 2005; Schneider et al., 2007).

133 The western margin of the Hearne Craton comprises two distinct domains of Paleoproterozoic age: the Mudjatik
134 domain and the Wollaston domain (Fig. 1A). The Mudjatik domain is predominantly composed of Archean
135 tonalite-trondhjemite felsic gneiss domes (2640–2580 Ma; Annesley et al., 1997a, 1997b, 1999). In contrast, the
136 Wollaston domain is composed mainly of Paleoproterozoic metasediments attributed to the Wollaston Supergroup
137 (deposited at ca. 2050–1860 Ma; Yeo and Delaney, 2007; Tran et al., 2008), including paragneisses, banded iron
138 formations, quartzites, and marbles. These units are interpreted as evidence of sedimentation initially controlled
139 by a passive-margin setting, which evolved into a back-arc basin and then into a foreland basin in response to
140 tectonic processes related to the collision phase (Annesley et al., 2005; Jeanneret et al., 2016). The two lithotectonic
141 domains are separated by the Wollaston-Mudjatik Transition Zone (WMTZ), within which the present study area
142 is located (Fig. 1A). This zone exhibits an anastomosed structure oriented from northeastern to southwestern, a
143 trait that was inherited from the THO. The deformation phases associated with the various stages of THO formation
144 mentioned above can be observed within this zone.

145 The basement rocks underwent three tectono-metamorphic events. The first event (M1–D1) is dated from ca. 1840
146 to 1813 Ma based on U–Pb dating of monazite and zircon from migmatitic metapelites of the Wollaston
147 Supergroup. These rocks host a garnet-cordierite ± sillimanite assemblage that experienced partial melting at peak
148 conditions of 750–825 °C and ≤1 GPa (Annesley et al., 1992, 1997a,b,c, 1999a,b; Jeanneret et al., 2017; Toma et
149 al., 2024). The second event (M2–D2), dated from ca. 1813 to 1770 Ma, is recorded within migmatites and
150 pegmatites. It corresponds to an isothermal decompression down to 0.5–0.9 GPa at temperatures of 750–825 °C,
151 within the stability field of cordierite under suprasolidus conditions, as constrained by U–Pb dating of monazite

152 and zircon (Annesley et al., 1992, 1997a,b,c, 1999a,b; Jeanneret et al., 2017; Toma et al., 2024). The third event
153 corresponds to an exhumation and orogenic cooling phase. Although its onset is poorly constrained, this phase is
154 generally considered to extend from ca. 1770 Ma (750 °C, 0.5 GPa) to ca. 1720 Ma (350 °C, 0.2 GPa), as
155 documented by several studies (Annesley and Madore, 1994; Annesley et al., 1992, 1997a,b,c, 2005; Jeanneret et
156 al., 2017; Martz, 2017). This exhumation phase is characterized by pronounced retrograde transformations linked
157 to early-stage hydrothermal activity. These include the breakdown of cordierite in favour of phyllosilicates, biotite
158 chloritization, remobilization and precipitation of sulfides, graphite, and muscovite, circulation of quartz-rich
159 fluids, and dissolution-reprecipitation processes affecting monazite and zircon (Card, 2012, 2014; Card and Noll,
160 2016). This phase is further constrained by cooling ages derived from biotite Rb–Sr (Worden et al., 1985; Schneider
161 et al., 2007), muscovite K–Ar (Philippe et al., 1993), and muscovite Ar–Ar systems (Alexandre et al., 2009).

162 **2.2. Geological history of the Athabasca Basin**

163 The Paleoproterozoic to Mesoproterozoic Athabasca Basin is a large intracratonic basin located in northern
164 Saskatchewan and Alberta (Ramaekers et al., 2007). The sedimentary sequence of this basin, known as the
165 Athabasca Supergroup, was deposited between ca. 1760–1720 Ma (Ramaekers et al., 2007; Jeanneret et al., 2016)
166 and 1541 Ma for the youngest known age (Creaser and Stasiuk, 2007). Stratigraphic, geochronological, and fluid-
167 inclusion *P-T* data indicate that the basin reached a maximum depth of 2 to 5 km depending on the methods
168 considered (Pagel et al., 1975a, b; Chi et al., 2018), with a preserved thickness of 1.5 km today (Hobson and
169 MacAulay, 1969). The stratigraphic sequence is organized into four major clastic sedimentary sequences that
170 record a progressive deepening of the basin (Jefferson et al., 2007). The first sequence, represented by the Fair
171 Point Formation, consists of conglomerates and quartz-pebble arenites infilling the Jackfish Sub-basin, located in
172 the western part of the basin, during the initial sag phase around 1760 Ma (e.g., Ramaekers et al., 2007; Pehrsson
173 et al., 2023). The second sequence, including the Smart/Read and Manitou Falls formations, fills the Cree Sub-
174 basin, situated in the eastern and southeastern parts of the basin, and reflects the development of a shallow half-
175 graben with NW-directed palaeoflow between 1680 and 1650 Ma (Ramaekers et al., 2007; Jeanneret et al., 2016;
176 Pehrsson et al., 2023). The third sequence, represented by the Lazenby Lake and Wolverine Point formations,
177 shows vertical fining and records a major paleoenvironmental shift around 1640 Ma, characterized by abrupt
178 deepening in the western basin, a marine incursion, and a transition to axial palaeocurrents sourced from the north
179 or east (Rainbird et al., 2007; Ramaekers et al., 2007), as indicated by vitric tuff layers dated at 1644 ± 13 Ma (U-
180 Pb zircon; Rainbird et al., 2007). The final sequence, which includes the Locker Lake, Otherside, Douglas, and
181 Carswell formations, reflects detrital and marine sedimentation during continued subsidence and tectonic
182 reorganization associated with the Kuungmi rifting (Pehrsson et al., 2023), notably recorded by organic-rich black
183 shales of the Douglas Formation dated by Re–Os at 1541 ± 13 Ma (Creaser and Stasiuk, 2007). Overall, the basin
184 maintains a largely coherent oval geometry with minimal deformation, except for the Ordovician Carswell impact
185 structure, which locally disrupts the Athabasca Supergroup (Ramaekers et al., 2007; Pehrsson et al., 2023).

186 **2.3. Petrographic and metallogenic characteristics of unconformity-related uranium deposits in the** 187 **Athabasca Basin**

188 The Athabasca Basin unconformity-related uranium deposits are globally renowned for their exceptionally high
189 grades, reaching up to 20 wt. % U₃O₈. The principal uranium deposits are concentrated in the eastern part of the
190 Athabasca Basin and are spatially associated with a NE-SW-trending anastomosed transition zone inherited from

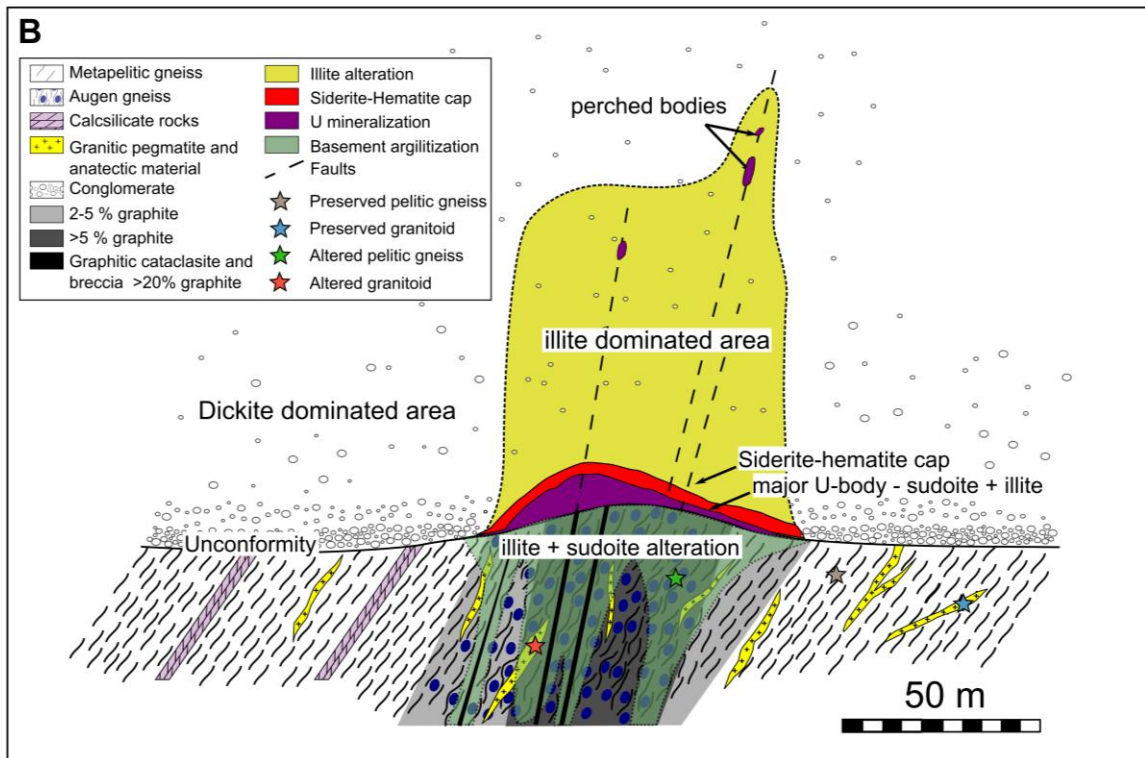
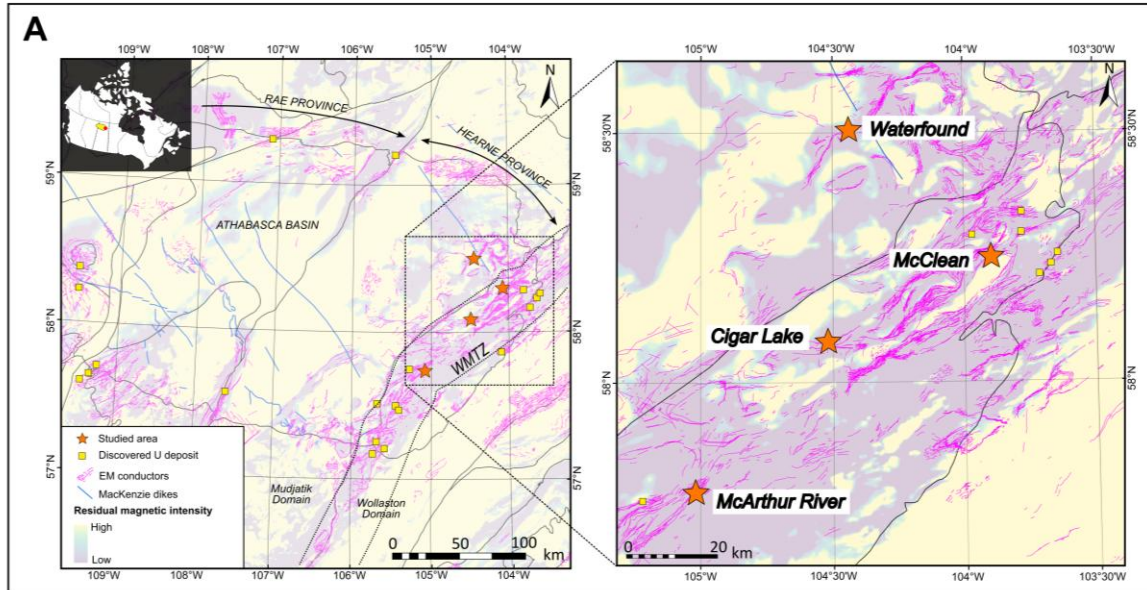
191 the Trans-Hudsonian Orogeny (THO), commonly referred to as the Wollaston-Mudjatik Transition Zone. This
192 structural corridor comprises a ca. 50-km-wide network of graphite-rich shear zones, typically described as
193 graphite conductors, as they exhibit high electrical conductivity, a physical property that allows their detection by
194 electromagnetic geophysical methods used for uranium exploration (Fig. 1). The uranium deposits are spatially
195 associated with graphite-rich shear zones, and uranium orebodies show diverse morphologies and structural
196 associations depending on their location: (i) at the unconformity, within the first meters of sandstones and
197 conglomerates; (ii) within the basement, extending several hundred meters below the unconformity along shear
198 zones; or (iii) as perched deposits located tens to hundreds of meters above the unconformity within the
199 sedimentary sequence. The mineralized zones are surrounded by hydrothermal alteration halos that can extend
200 several tens of meters into both the basin and the basement and serve as critical geochemical and mineralogical
201 guides for U exploration. In the basin, alteration halos overlying basement-hosted deposits or surrounding
202 sandstone-hosted mineralization are dominated by illite, with variable amounts of kaolinite, sudoite (tri-
203 dioctahedral Mg-chlorite), and dravite (magnesian tourmaline), depending on the deposit.

204 Within the basement, three principal alteration types are superimposed, as exemplified by the world-class Cigar
205 Lake deposit (Fig. 1C). The first type corresponds to retrograde metasomatic alteration related to the final
206 exhumation and orogenic cooling phase of the Trans-Hudsonian Orogeny (THO). It is marked by partial to
207 complete biotite chloritization, discrete quartz and muscovite crystallization, and hydrothermal graphite formation.
208 These alteration types and their associated petrographic features have been extensively documented in the vicinity
209 of unconformity-related uranium deposits within the Athabasca Basin (e.g., Carl et al., 1992; Derome et al., 2005;
210 Cloutier et al., 2011; Mercadier et al., 2011; Alexandre et al., 2012; Adlakha et al., 2015; Martz et al., 2019a;
211 Menier et al., 2020; Powell et al., 2022). The second type corresponds to regolith alteration developed within the
212 upper tens of meters of the basement following its exhumation after the Trans-Hudsonian Orogeny. It is
213 characterized by a laterally correlative weathering profile comprising four zones: (i) a bleached kaolinite-rich and
214 hematite-depleted zone at the unconformity; (ii) a highly oxidized hematite-rich zone; (iii) a red-green transitional
215 zone characterized by hematite and chlorite; and (iv) a thicker green-to-red zone enriched in illite, chlorite, and
216 hematite (e.g., Macdonald, 1980; Halter, 1988). The third type corresponds to post-basin-deposition hydrothermal
217 alteration, which represents the most extensive alteration type. It is proposed to be linked with uranium
218 mineralization and is characterized by the massive replacement of primary minerals by an illite- and sudoite-
219 dominated clay assemblage.

220 The main accepted model for the formation of these deposits is known as “diagenetic-hydrothermal” and involves
221 the circulation of oxidized brines of marine origin containing NaCl-CaCl₂ at temperatures of around 120–200 °C
222 in the basin and underlying bedrock (Derome et al., 2005; Richard et al., 2011, 2013, 2015). The interaction of
223 these brines with basin and/or basement rocks favors the formation of alteration halos and mobilizes uranium in
224 its oxidized form (U⁶⁺), which is transported through fractures and reactivated graphitic structures. Uranium
225 precipitates within structural and physicochemical traps, where dissolved hexavalent uranium (U⁶⁺) is reduced to
226 tetravalent uranium (U⁴⁺) (Hoeve and Sibbald, 1978; Jefferson et al., 2007).

227 Published absolute ages for the precipitation of primary uranium mineralization at the scale of the basin span a
228 broad range, from ca. 1590 to 1200 Ma. These estimates derive from U–Pb analyses of UO₂ and from K–Ar or
229 Ar–Ar geochronology of clay minerals (Cumming and Krstic, 1992; Philippe et al., 1993; McGill et al., 1993;

230 Fayek and Riciputi, 2002; Alexandre et al., 2009; Cloutier et al., 2011; Powell et al., 2022). Building on these age
231 constraints, an alternative hypothesis invoking an earlier episode of uranium mineralization and/or hydrothermal
232 alteration merits consideration. Numerous studies have shown that U–Pb systematics of uraninite and associated
233 alteration minerals in unconformity-related deposits are commonly overprinted by multiple fluid-flow events,
234 resulting in partial Pb loss and a broad dispersion of apparent ages (Kotzer and Kyser, 1990; Fayek and Kyser,
235 1997; Fayek et al., 2002; Fayek and Riciputi, 2002; Kyser et al., 2015). Consequently, the existence of an older
236 hydrothermal system, potentially active in the ca. 1640–1680 Ma interval, cannot be ruled out and may be cryptic
237 due to subsequent alteration, uranium remobilization, and isotopic resetting during younger tectono-hydrothermal
238 episodes. This interpretation is consistent with evidence for repeated basin-scale fluid circulation and late-stage
239 meteoric fluid ingress documented in the Athabasca Basin, processes that are known to modify both clay mineral
240 K–Ar/Ar–Ar ages and uraninite U–Pb signatures. A similarly complex temporal evolution is recognized in
241 unconformity-related uranium systems of northern Australia, where *in situ* U–Pb analyses of uraninite suggest
242 initial mineralization or hydrothermal alteration as early as ca. 1680–1640 Ma, followed by multiple younger
243 resetting events extending into the Mesoproterozoic and Paleozoic (Clauer et al., 2015; Skirrow et al., 2016).



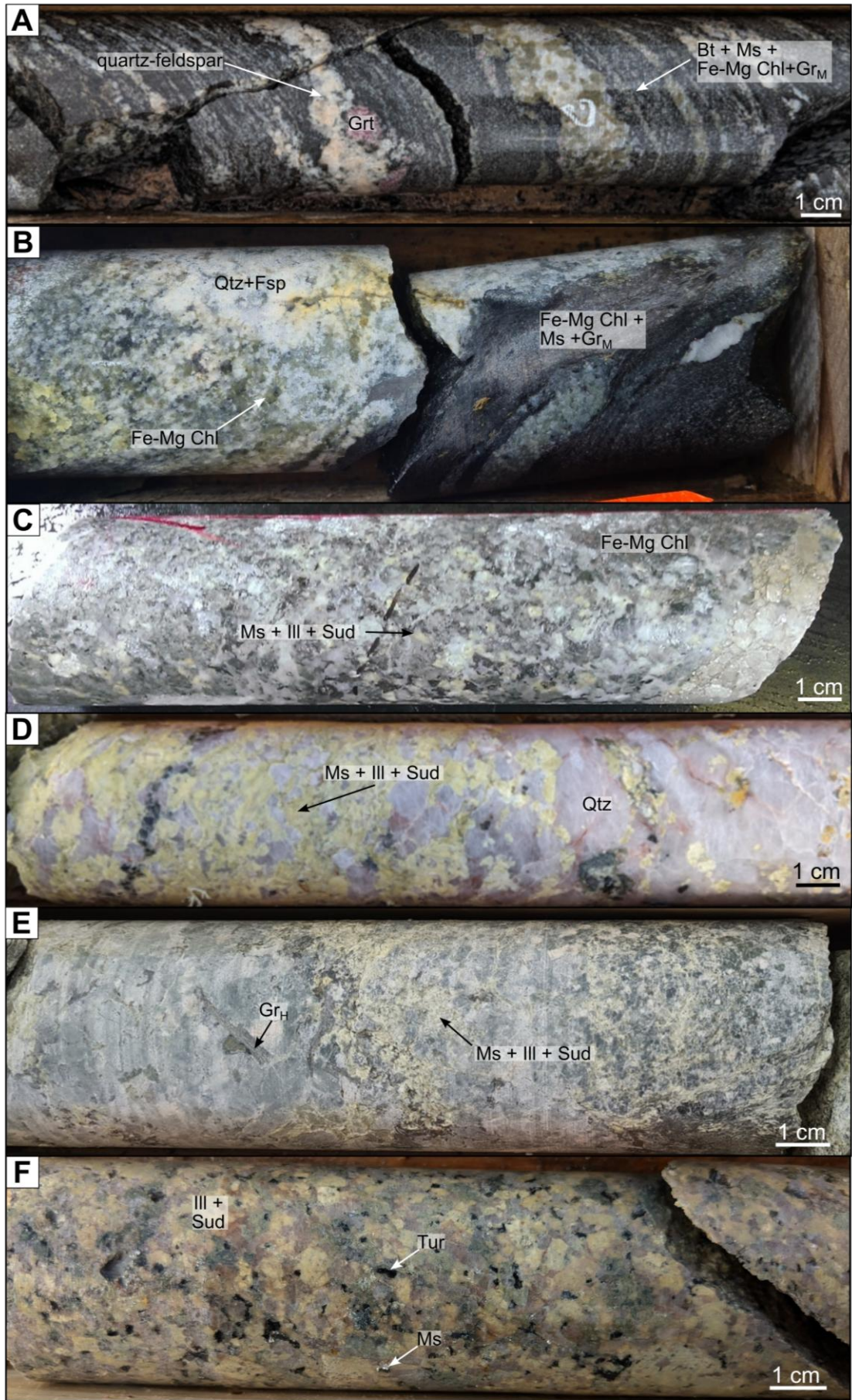
244

245 **Figure 1:** (A) Left: map of the Athabasca Basin (Saskatchewan, Canada) with the outline of the different lithotectonic
 246 units forming the basement. Right: zoom of the study area located in the eastern part of the Athabasca Basin along the
 247 WMTZ. The graphitic conductors (in magenta) are interpreted from electromagnetic (EM) data by the Saskatchewan
 248 Geological Survey (SGS) from airborne EM surveys, and correspond to graphitic-rich shear zones hosting uranium
 249 mineralization. The yellow squares represent deposits or mineralizations with economic potential, and the blue stars
 250 represent the studied sites. Data source: Saskatchewan Geological Survey (electromagnetic data). Map created using
 251 ArcGIS Pro. Coordinate Reference System (CRS): WGS 84. (B) Schematic cross-section through the main ore body of
 252 Cigar Lake, archetype of unconformity-related U deposits. U is located at the unconformity above a ductile-brittle
 253 graphitic shear zone (modified after Martz et al., 2019a) and is associated with an alteration halo dominated by illite
 254 and sudoite in both basin and basement. The theoretical locations of the four types of samples examined in this study
 255 are indicated by colored stars.

256 **3. Materials and methods**

257 **3.1. Sampling strategy**

258 Four study areas located in the northeastern segment of the Wollaston-Mudjatik Transition Zone (WMTZ) were
259 selected to evaluate the applicability of in-situ Rb–Sr geochronology to date the main hydrothermal alteration
260 (illite-sudoite) associated with the U mineralisation within the basement rocks. From north to south, these areas
261 comprise the Waterfound (WF) and McClean South (MCS) prospects, and the Cigar Lake (CL) and McArthur
262 River (MAC) deposits. All samples from WF, MCS, and CL analyzed in this study were obtained from drill cores
263 collected during the past five years as part of U exploration programs conducted by Orano Canada Inc., whereas
264 samples from MAC were provided by Cameco Corporation. The sampling strategy at the four study sites was
265 designed to ensure both lateral and vertical representativeness, spanning from unaltered basement zones (Fig. 2A,
266 B) to hydrothermally altered domains characterized by illite-sudoite assemblages associated with the
267 mineralization (Fig. 2C, D, E, F). For MCS, five drill holes were considered from west to east: MCS-03, MCS-05,
268 MCS-34, MCS-35C and MCS-31 (mineralized conductor). For WF, six drill holes were considered from southwest
269 to northeast: WF-93, WF-98, WF-66, WF-77 and WF-75 (mineralized conductor) and WF-100 (outside the La
270 Rocque Conductive Corridor). For CL, two drill holes were considered from west to east: WC-449 (mineralized
271 conductor) and WC-473 (non-mineralized conductor). For MAC, five drill holes were considered from west to
272 east: MC-408, MC-408-01, MC-418, MC-410-01, MC-410-02 (mineralized conductor). Pelitic gneisses and
273 anatectic granitoids represent the two dominant lithologies within the WMTZ, particularly within the graphite-rich
274 shear zones that host mineralization, which justifies their selection for this study. Across all investigated sites, four
275 samples of pelitic gneisses unaffected by illite-sudoite alteration were analyzed, together with five samples of
276 anatectic granitoids and/or associated leucosomes that were likewise preserved from this alteration. Their altered
277 equivalents comprise ten samples of pelitic gneisses affected by illite-sudoite alteration and nineteen samples of
278 anatectic granitoids and/or leucosomes exhibiting the same alteration signature. All samples were specifically
279 selected based on their high muscovite modal abundances and the presence of muscovite grains of sufficient size
280 to enable *in situ* Rb–Sr analyses by LA-ICP-MS.



282 **Figure 2. Macroscopic pictures of drill cores intervals sampled for this study (A) Anatectic pelitic gneiss containing**
283 **metamorphic graphite (Gr_M), biotite (Bt), muscovite (Ms) and Fe-Mg chlorite (Fe-Mg Chl) within the restite; the contact**
284 **between the quartz-feldspar leucosome (Qtz+Fsp) and the restite is marked by garnet. Evidence of retro-metamorphic**
285 **alteration is visible within the quartz-feldspar leucosome and is characterized by a fir-green coloration [MC-408_591.3**
286 **m]. (B) Anatectic pelitic gneiss showing an accumulation of metamorphic graphite in the restite; the quartz-feldspar**
287 **leucosome exhibits retro-metamorphic alteration features, with Fe-Mg chlorite imparting a dark green coloration to**
288 **the core rock [MCS-05_285.5 m]. The restite is composed of metamorphic graphite, biotite, muscovite. (C) Strongly**
289 **altered granitoid characterized by nearly complete replacement of feldspars and plagioclase by illite and sudoite**
290 **(Ill+Sud), while quartz and ferromagnesian chlorites remain preserved. Here, muscovite is embedded within the illite-**
291 **sudoite assemblage and is not macroscopically observable [WC-449_434.4 m]. (D) Granitoid exhibiting pervasive illite-**
292 **sudoite alteration, within which muscovite is entirely incorporated into the fine-grained alteration matrix and is not**
293 **discernible at the macroscopic scale [MC-410-02_687.4 m]. (E) Anatectic pelitic gneiss hosting hydrothermal graphite**
294 **(Gr_H) concentrations within the leucosome, associated with the retrograde metamorphic features and an illite-sudoite**
295 **alteration matrix in which muscovite is cryptic and not macroscopically distinguishable. [MCS-34_273.7 m]. (F)**
296 **Granitoid exhibiting intense illite-sudoite alteration of primary minerals, imparting an apple-green coloration to the**
297 **entire drill core, with muscovite and tourmaline (Tur) also locally preserved and macroscopically visible [WF-93_581.0**
298 **m].**

299 **3.2. Methods**

300 Scanning electron microscopy (SEM), electron probe microanalysis (EPMA), and micro-X-ray fluorescence
301 (μ XRF) analyses were performed at the Service Commun de Microscopies Électronique et de Microanalyse X
302 (SCMEM) in Nancy, France, whereas *in situ* Rb–Sr isotopic analyses were carried out on the ICP platform at
303 GeoRessources, Université de Lorraine (Nancy, France).

304 **3.2.1. Petrography - Optical and SEM**

305 Samples were first observed using a conventional optical microscope under transmitted light. Thin-section scale
306 mapping was conducted using a Keyence VHX-2000 optical microscope. Muscovite and associated minerals were
307 imaged using a TESCAN VEGA 3 LM scanning electron microscope (SEM). This SEM is equipped with a
308 conventional tungsten filament and is coupled to two Bruker XFlash 6–30 mm² EDS detectors. The backscattered
309 electron (BSE) images were obtained using the following parameters: an accelerating voltage of 15 kV, a working
310 distance (WD) of 15 mm, a beam current of 0.5 nA, and an acquisition speed of 1 ms per pixel.

311 **3.2.2. X-ray fluorescence (XRF)**

312 Thin sections were analyzed using a BRUKER M4 TORNADO micro-XRF, which enables localized analysis of
313 elements ranging from sodium to uranium, with a maximum spatial resolution of approximately 20 μ m and a
314 sensitivity varying from around one percent for light elements (Na) to several tens of ppm for more sensitive
315 elements (Zr). The device is equipped with a rhodium X-ray tube, polycapillary optics to focus the beam and two
316 Bruker SDD-type EDS detectors to enhance acquisition speed, allow for the identification of diffraction peaks,
317 and reduce shadowing effects. Mapping parameters included a 35 μ m step size, with a dwell time of 10 ms,
318 corresponding to a scan speed of 3.5 mm/s. X-ray tube parameters were set to 400 μ A and 50 kV, under a 2 Pa
319 vacuum. μ -XRF data were subsequently processed using the M4 TORNADO software to generate elemental maps.

320 **3.2.3. Electron probe microanalysis (EPMA)**

321 X-ray elemental maps of K ($K\alpha$), Rb ($K\alpha$), Mg ($K\alpha$), Al ($K\alpha$), Ca ($K\alpha$), F ($K\alpha$), Fe ($K\alpha$), Mn ($K\alpha$) and Na ($K\alpha$)
322 on selected areas in thin sections were carried out using a CAMECA SX5 TACTIS electron microprobe, equipped
323 with a LaB₆ tip and five vertical WDS spectrometers. The analytical conditions included a beam current of 100
324 nA, an accelerating voltage of 25 kV, and a counting time of 20 ms per pixel.

325 3.2.4. In situ Rb–Sr isotopic analysis (LA-ICP-MS/MS)

326 *In situ* Rb–Sr analyses on muscovite were carried out using a LA-ICP-MS/MS system. The $^{87}\text{Rb}/^{86}\text{Sr}$ and $^{87}\text{Sr}/^{86}\text{Sr}$
327 ratios of the studied samples and reference materials were determined using an Agilent 8900 ICP-MS/MS coupled
328 with a 193 nm ArF excimer laser ablation system ESI 193 nm ArF with a TwoVol2 dual-volume ablation cell. All
329 samples were ablated employing a 50 μm spot size for 90 to 110 s (30 to 40 s of gas blank measurement and 30 to
330 40 s of ablation time followed by 30 s of sample washout), with a repetition rate of 10 Hz and a laser energy density
331 of 6 $\text{J}\cdot\text{cm}^{-2}$. Helium at a flow rate of 700 $\text{mL}\cdot\text{min}^{-1}$ was used as a carrier gas in the ablation cell, then mixed with
332 N_2 via a Y connector at a flow rate of 4 $\text{mL}\cdot\text{min}^{-1}$ and argon nebulization gas at a flow rate of 700 $\text{mL}\cdot\text{min}^{-1}$ before
333 entering the ICP-MS torch. The reaction gas N_2O was used to overcome isobaric interferences to separate ^{87}Sr
334 from ^{87}Rb due to the efficiency of N_2O in reacting with Sr^+ to form SrO^+ ions, which was not the case for Rb^+ .
335 The following isotopes were measured (integration time in parentheses): $^{28}\text{Si} \rightarrow ^{28}\text{Si}$ (2 ms), $^{84}\text{Sr} \rightarrow ^{84}\text{Sr}$ (5 ms),
336 $^{84}\text{Sr} \rightarrow ^{100}\text{SrO}$ (120 ms), $^{85}\text{Rb} \rightarrow ^{85}\text{Rb}$ (20 ms), $^{85}\text{Rb} \rightarrow ^{101}\text{Rb}$ (5 ms), $^{86}\text{Sr} \rightarrow ^{86}\text{Sr}$ (5 ms), $^{86}\text{Sr} \rightarrow ^{102}\text{SrO}$ (120 ms),
337 $^{87}\text{Sr} \rightarrow ^{87}\text{Sr}$ (5 ms), $^{87}\text{Sr} \rightarrow ^{103}\text{SrO}$ (120 ms), $^{88}\text{Sr} \rightarrow ^{88}\text{Sr}$ (5 ms), $^{88}\text{Sr} \rightarrow ^{104}\text{SrO}$ (120 ms). A scan of all isotopes
338 (sampling period) took approximately 565 ms. Seven sessions were conducted to analyze all samples. The NIST
339 SRM 610 glass (Woodhead and Hergt, 2001) and MicaMg mica (Hogmalm et al., 2017, Jegal et al., 2022) were
340 used as external standards for the correction of the $^{87}\text{Sr}/^{86}\text{Sr}$ and $^{87}\text{Rb}/^{86}\text{Sr}$ ratios, respectively. Although matrix
341 effects between phlogopite and natural muscovite cannot be entirely excluded when using MicaMg as primary
342 reference material for $^{87}\text{Rb}/^{86}\text{Sr}$ correction (Glorie et al., 2024), its use currently remains unavoidable as it
343 represents the only widely available and internationally distributed nano-powder reference material specifically
344 designed and validated for *in situ* Rb–Sr dating by LA-ICP-MS/MS. La Posta biotite was used as a secondary
345 reference material to monitor the stability of the instrumental setup and the long-term reproducibility of the
346 analytical protocol. It has a reported weighted mean age of 93.8 ± 2.5 Ma and an initial $^{87}\text{Sr}/^{86}\text{Sr}$ ratio of 0.70483
347 ± 0.0005 (ID-TIMS, Walawender et al., 1990). The Sr/Sr_i value for La Posta calculated using NIST 610 is
348 consistent and further confirmed by the value calculated for MicaMg via NIST 610. Reproducing both the
349 reference age and the initial Sr isotopic composition provides an independent assessment of analytical accuracy.
350 To quantitatively evaluate long-term reproducibility, La Posta analyses acquired over a three-year period were
351 grouped by analytical session. For each session, an isochron age was calculated independently. The resulting
352 session ages were then combined using a weighted mean, in which each session age was weighted by the inverse
353 square of its internal uncertainty, and the dispersion of individual session ages around this weighted mean,
354 quantified as the standard deviation of the weighted residuals, yields an external reproducibility of approximately
355 1.6% (2σ), which is adopted as a realistic estimate of long-term analytical uncertainty (Supplementary Figure S1).
356 Final age uncertainties reported in this study incorporate both the internal analytical uncertainty and this external
357 reproducibility through quadrature propagation, such that $\sigma_{\text{total}} = \sqrt{(\sigma_{\text{internal}}^2 + \sigma_{\text{reproducibility}}^2)}$. The
358 overall weighted mean age is 93.9 ± 1.2 Ma (2σ) with an MSWD of 0.38. In addition, regression intercepts from
359 individual sessions were compiled to calculate a weighted mean initial $^{87}\text{Sr}/^{86}\text{Sr}$ ratio of 0.7045 ± 0.0018 (2σ). This
360 value is in excellent agreement with the ID-TIMS constrained value of 0.70483 reported by Walawender et al.
361 (1990). The consistency of both age and intercept values over three years demonstrates robust long-term stability
362 of Sr isotopic measurements. These results indicate no evidence for significant instrumental drift, calibration bias,
363 or matrix-dependent effects, and effectively exclude an analytical origin for the anomalously low initial $^{87}\text{Sr}/^{86}\text{Sr}$
364 values observed in some samples. LA-ICP-MS/MS data reduction was performed using Iolite 4 (Paton et al., 2011).

365 The processed and calibrated data for $^{87}\text{Sr}/^{86}\text{Sr}$ and $^{87}\text{Rb}/^{86}\text{Sr}$ ratios were plotted in conventional isochron and radial
366 plots and used to calculate Rb–Sr isochron ages and corresponding regression intercepts using IsoplotR
367 (Vermeesch, 2018). In the following, regression intercepts refer strictly to the mathematical intercepts of Rb–Sr
368 regressions and are not interpreted as true initial $^{87}\text{Sr}/^{86}\text{Sr}$ ratios.

369 Concentrations of ^{87}Rb , ^{86}Sr , and ^{87}Sr were calculated from LA-ICP-MS isotopic measurements using a
370 reproducible procedure that accounts for isotopic abundances, measured Rb–Sr ratios, and matrix effects. Total
371 ^{87}Rb concentrations (ppm) were derived from the measured ^{85}Rb signal by correcting for the natural isotopic
372 abundances ($^{85}\text{Rb} = 0.7217$, $^{87}\text{Rb} = 0.2783$) of Rb according to Eq. (1):

$$373 \quad (1) \quad ^{87}\text{Rb} = ^{85}\text{Rb}_{\text{measured}} \times \frac{0.7217}{0.2783}$$

374 Concentrations of ^{86}Sr were then calculated from the measured $^{87}\text{Rb}/^{86}\text{Sr}$ ratios obtained from the Rb–Sr regression
375 diagrams according to Eq. (2):

$$376 \quad (2) \quad ^{86}\text{Sr} = \frac{^{87}\text{Rb}}{(^{87}\text{Rb}/^{86}\text{Sr})_{\text{measured}}}$$

377

378 Subsequently, ^{87}Sr concentrations were calculated using the measured $^{87}\text{Sr}/^{86}\text{Sr}$ ratios according to Eq. (3):

$$379 \quad (3) \quad ^{87}\text{Sr} = (^{87}\text{Sr}/^{86}\text{Sr})_{\text{measured}} \times ^{86}\text{Sr}$$

380

381 To correct for instrumental fractionation and sample–standard differences, a matrix correction factor of 0.532038
382 was applied to all calculated concentrations according to Eq. (4):

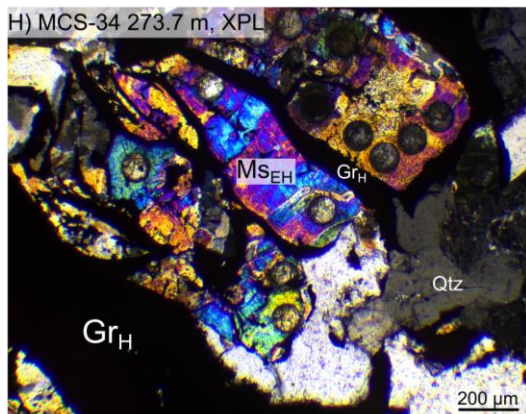
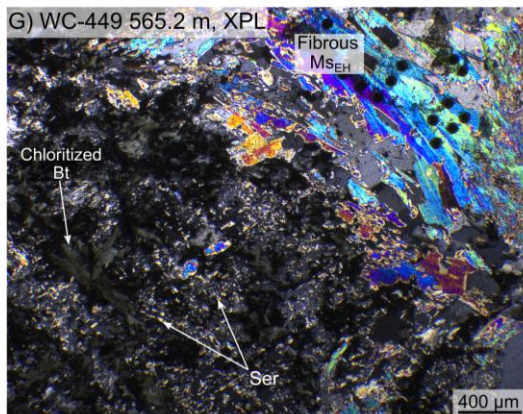
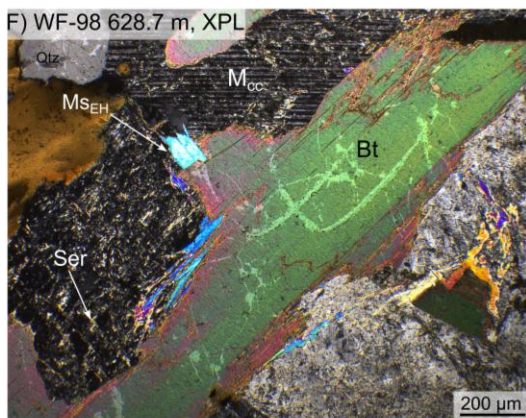
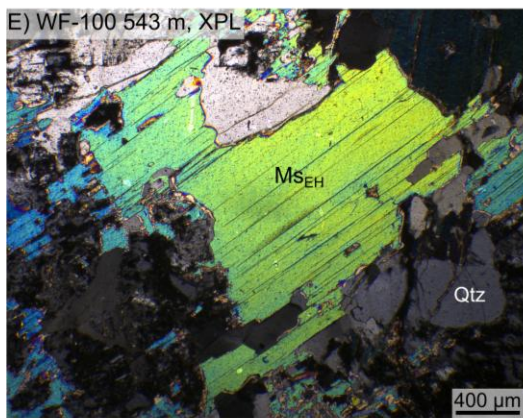
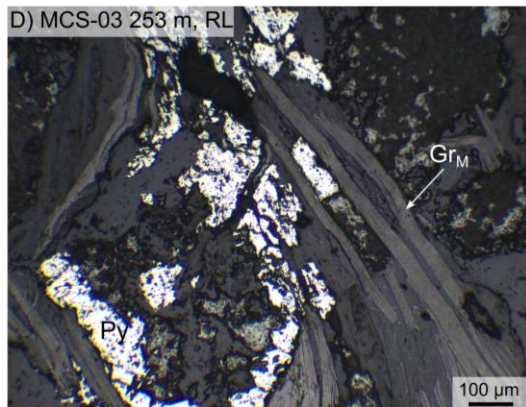
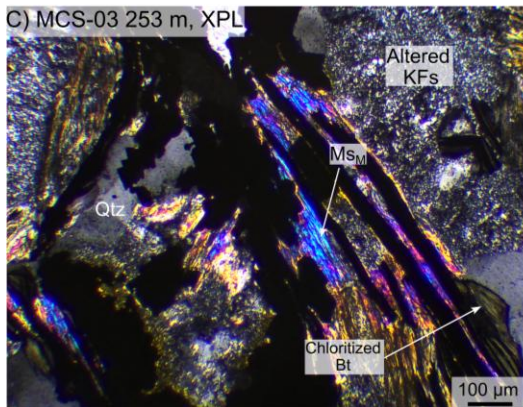
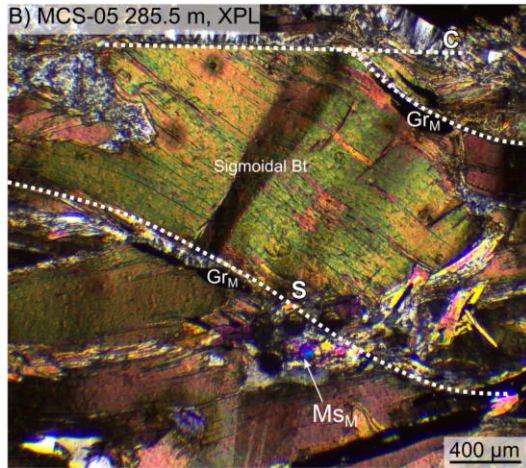
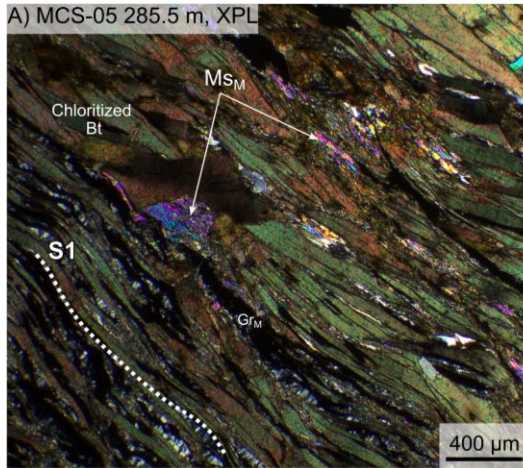
$$383 \quad (4) \quad C_{\text{corrected}} = C_{\text{calculated}} \times 0.532038$$

384 This factor was determined from the internal standard MicaMg by comparing the measured ^{85}Rb concentration
385 with its published reference value (Jegal et al., 2022) and then applied proportionally to ^{87}Rb , ^{87}Sr , and ^{86}Sr in all
386 samples. The complete dataset of raw Rb–Sr isotope ratios, single-spot ages, uncertainties, and matrix-corrected
387 elemental concentrations is provided in Supplement Table S1.

388 4. Results

389 Two types of muscovite, identified in the least altered zones of the metasomatic halos, are investigated (Fig. 2A
390 and B): (i) (retro-)metamorphic muscovite associated with the retrograde mineral assemblage within metamorphic
391 rocks and (ii) early hydrothermal muscovite within magmatic rocks as a secondary phase. All of the studied
392 samples exhibit evidence of a first alteration associated with the retrograde metamorphism and are variably
393 overprinted by a second hydrothermal alteration that is described below.

394



396 **Figure 3. (A-B) Graphitic pelitic gneiss [MCS-05_285.5 m]. (A) Pelitic gneiss displaying a well-developed foliation.**
397 **Biotite (Bt) and thick flakes of metamorphic graphite (Gr_M) are aligned along the S1 foliation, while retrograde**
398 **metamorphic muscovite (M_{SM}) crystallizes at the rims of biotite, perpendicular to S1. (B) Plastically deformed biotite**
399 **marking a C-S fabric, with fine-grained metamorphic muscovite precipitating around biotite and within biotite pressure**
400 **shadows. (C-D) Graphitic pelitic gneiss with retrograde mineral assemblage [MCS-03_253 m]. Assemblage of quartz**
401 **(Qtz), K-feldspar (KFs), metamorphic muscovite, pyrite (Py), and metamorphic graphite, that has undergone**
402 **chloritization related to retrograde metamorphic alteration. Metamorphic muscovite is aligned with tabular flakes of**
403 **metamorphic graphite. (E-F) Granitoid rocks. (E) Subhedral early hydrothermal muscovite (M_{SEH}) crystals [WF-**
404 **100_543 m]. (F) Assemblage of biotite, quartz, and microcline (M_{cc}), showing early stages of sericitization (Ser). Early**
405 **hydrothermal muscovite precipitated as a secondary phase along biotite grain boundaries and has locally replaced, now**
406 **altered and sericitized, K-feldspar [WF-98_628.7 m]. (G) Leucosome of metapelitic gneiss characterized by fibrous**
407 **aggregates of early hydrothermal muscovite crosscutting partially to completely chloritized biotite [WC-449_565.2 m].**
408 **(H) Leucosome of metapelitic gneiss with early hydrothermal muscovite associated with large flakes of hydrothermal**
409 **graphite (Gr_H) [MCS-34_273.7 m].**

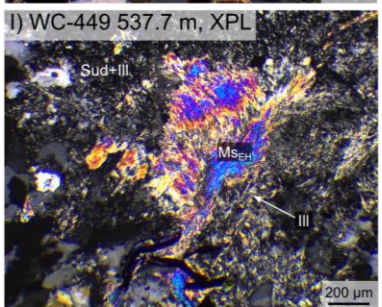
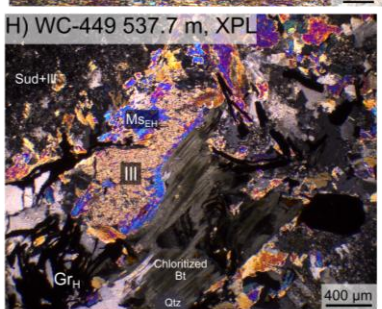
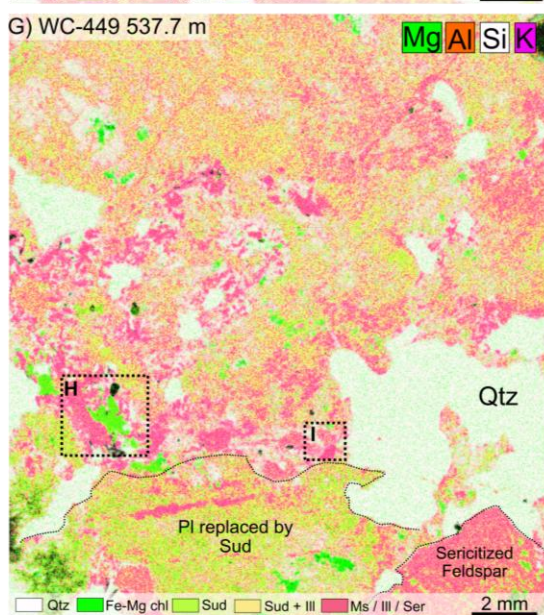
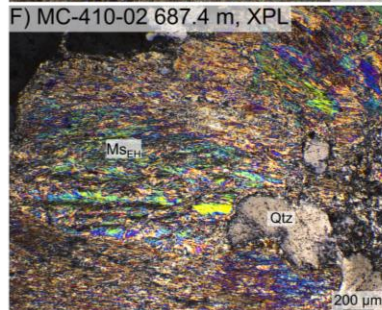
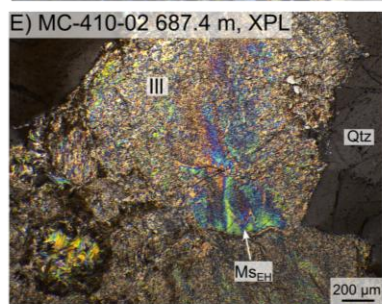
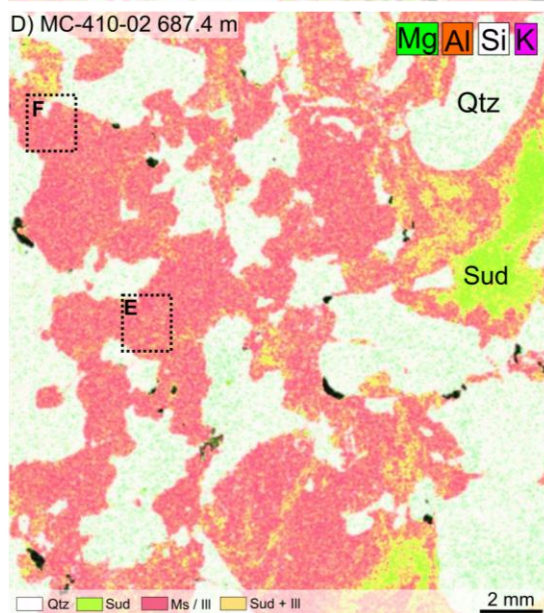
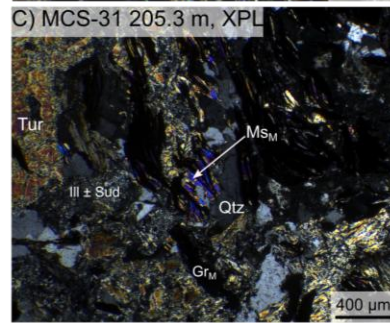
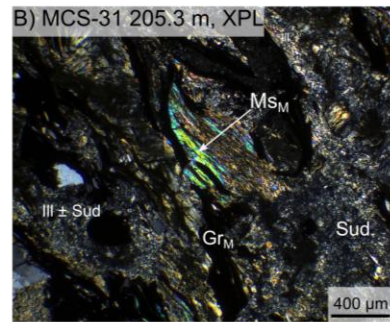
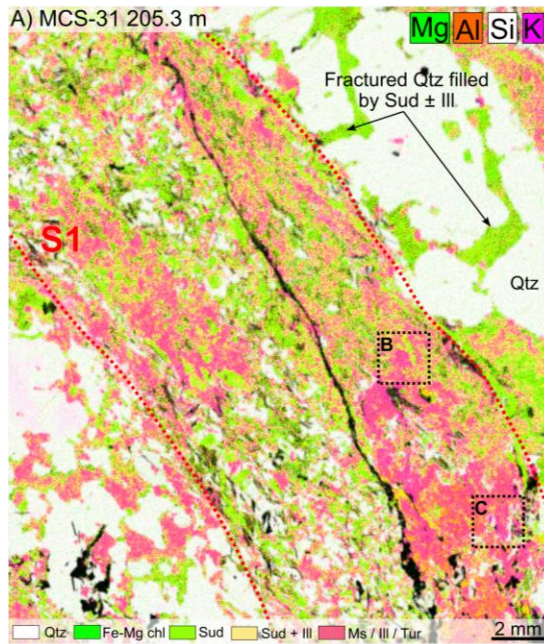
410 **4.1. Metamorphic muscovite**

411 Metamorphic muscovite is exclusively developed along the foliation planes of Paleoproterozoic metapelites (Fig.
412 2A,B) (e.g., Schneider et al., 2007; Skipton et al., 2016; Jeanneret et al., 2017; Martz, 2017). These rocks are
413 characterized by quartz and sericitized K-feldspar, and are bounded by graphite-rich shear zones containing biotite,
414 muscovite, and pyrite (Fig. 3A). Biotite occurs as lath-shaped crystals, locally plastically deformed showing C-S
415 planes, ranging from 0.5 to 1 mm in length, and oriented parallel to the subvertical S1 foliation. Muscovite is
416 present as euhedral to subhedral crystals, predominantly crystallizing along the rims of metamorphic biotite, with
417 an orientation perpendicular to the S1 foliation, suggesting a crystallization stage postdating biotite growth
418 possibly along the retrograde *P-T* path (Fig. 3A). Muscovite is also present within pressure shadows around biotite
419 mica-fish, suggesting that muscovite crystallization was contemporaneous with ductile deformation (Fig. 3B).
420 Metamorphic biotites are locally pseudomorphosed by Fe-Mg chlorite, a marker of retrograde metamorphism or
421 fluid-induced alteration (Fig. 3C). The metamorphic muscovite is commonly associated with medium-sized,
422 euhedral to tabular flakes of metamorphic graphite aligned along the foliation. Sulfides such as pyrite and
423 chalcopyrite are frequently associated with this metamorphic graphite (Fig. 3D).

424 **4.2. Early hydrothermal muscovite**

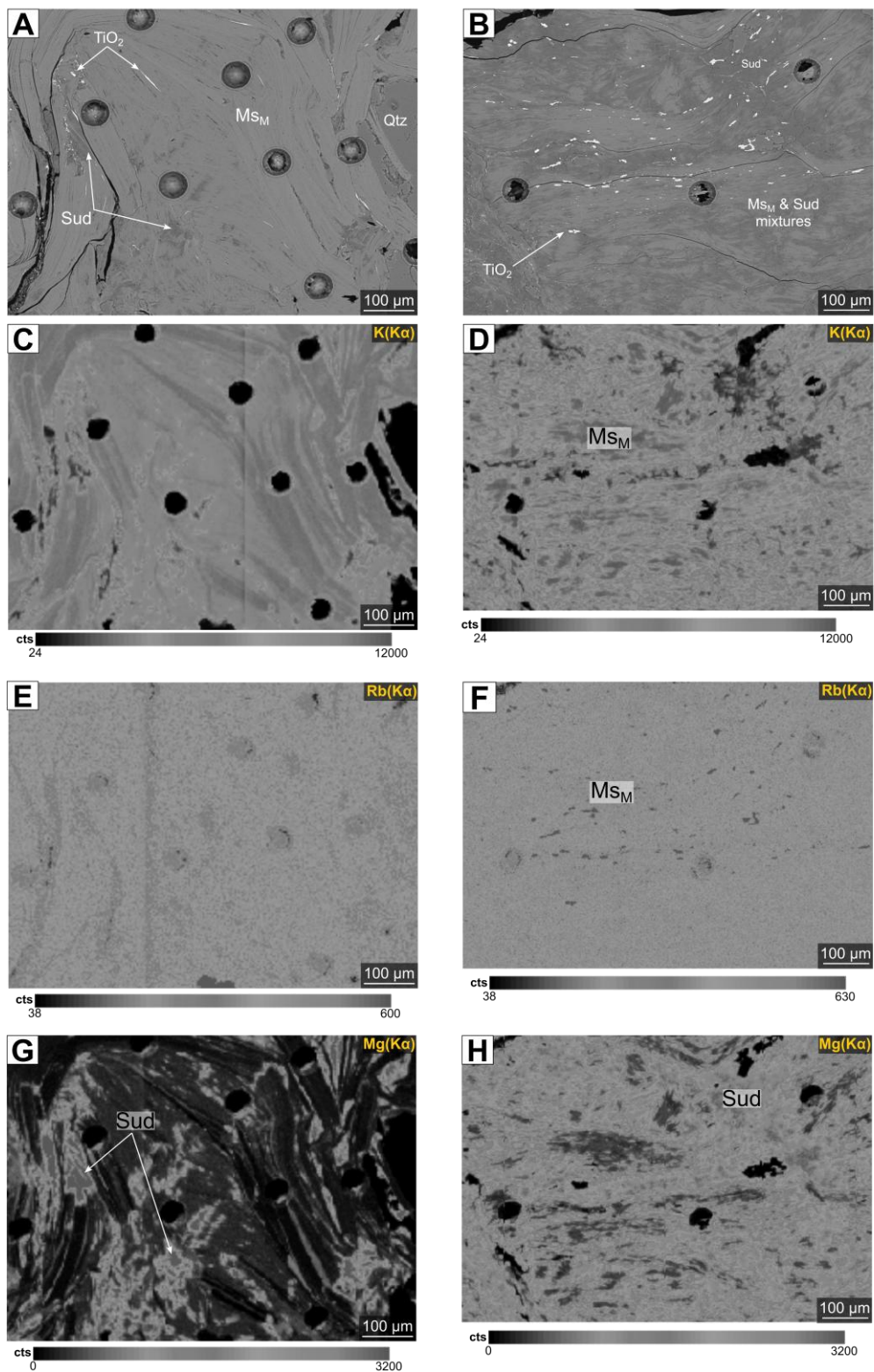
425 Early hydrothermal muscovite occurs within anatectic granitoids or within the leucosomes of metapelitic gneisses
426 (Fig. 2C, D, E, F) (e.g., Schneider et al., 2007; Skipton et al., 2016; Martz, 2017; Obin, 2025). These lithologies
427 are primarily composed of quartz, K-feldspar of the microcline type, often altered to sericite forming very fine
428 microlamellar aggregates with a shimmering whitish-grey appearance, plagioclase, and biotite laths, which are
429 partially to completely pseudomorphosed by Fe-Mg chlorite (Fig. 3E, F). Muscovite in these rocks occurs either
430 as subhedral crystals or as fibrous aggregates that may have partially to completely replaced chloritized biotite or
431 have precipitated along biotite grain boundaries as fine-grained crystals (Fig. 3E, F, G). It may also have locally
432 replaced K-feldspar (Fig. 3F). Muscovite is frequently associated with hydrothermal graphite, which occurs as
433 large flakes (up to 0.5 cm) precipitating interlayered with muscovite within late fractures or forming radiating
434 patterns in granitic leucosomes (Fig. 3H). These lithologies may also be locally enriched in tourmaline, occurring
435 as euhedral to subhedral crystals with strong relief and second-order yellow to green interference colors. Accessory
436 phases include zircon, monazite, and apatite, present as subhedral crystals or as veinlets crosscutting the
437 aforementioned minerals.

438 **4.3. Petrographic characteristics of altered muscovites**



440 **Figure 4. (A) Micro-X-ray fluorescence (μ -XRF) elemental maps of a thin section showing the distribution of Mg, Al, Si,**
441 **and K within a migmatitic graphitic pelitic gneiss including a leucosome [MCS-31_205.3 m]. Illite (Ill)-sudoite (Sud)**
442 **alteration is hosted along the mylonitic foliation planes of pelitic gneisses and occurs pervasively within the leucosome.**
443 **Sudoite also precipitates within fractures crosscutting the quartz (Qtz) vein. (B-C) Magnified views of (A) showing illite-**
444 **sudoite alteration affecting metamorphic muscovite (M_{SM}). (D) μ -XRF elemental mapping displaying the Mg, Al, Si,**
445 **and K distribution within an anatectic granitoid [MC-410-02_687.4 m]. Illite/sudoite ratios vary across the sample, with**
446 **domains that are fully illitized and others enriched in sudoite. (E-F) Magnified views of (D) illustrating the illitization**
447 **of early hydrothermal muscovite (M_{SEH}). (G) μ -XRF elemental maps showing the Mg, Al, Si, and K distribution within**
448 **an anatectic granitoid [WC-449_537.7 m]. Illite and sudoite crystallize pervasively, with spatial variations in the**
449 **illite/sudoite ratio. (H-I) Magnified views of (G) showing early hydrothermal muscovite illitization and the coexistence**
450 **of illite-sudoite replacing early minerals. Biotite associated with early hydrothermal muscovite is completely chloritized.**

451 This hydrothermal alteration affects both metamorphic muscovite (Figs. 4A-C) and early hydrothermal muscovite
452 (Figs. 4D-I). This Mg-K-type alteration pervasively affects the two lithologies that constitute the graphite-rich
453 shear zones, whether through the mylonitic foliation planes of pelitic gneisses (Figs. 4A-C), the grain boundaries
454 of magmatic to early hydrothermal minerals in anatectic granitoids and leucosomes (Figs. 4D-I), or through
455 fracture networks indiscriminately crosscutting the two lithologies. At the microscopic scale, this alteration is
456 expressed by the extensive replacement of primary and retro-metamorphic minerals by a clay assemblage
457 predominantly composed of micrometric illite, spatially associated with sudoite (a magnesium-rich trioctahedral
458 chlorite). However, this alteration is not uniformly distributed within the different lithologies, and the illite/sudoite
459 ratio varies between lithologies and within the same lithology (Figs. 4D, G). In anatectic granitoids and
460 leucosomes, the alteration is marked by the partial replacement of K-feldspar and the complete replacement of
461 plagioclase, which are more prone to alteration, by this clay assemblage (Figs. 4D-I). Fractures crosscutting quartz
462 and feldspars are commonly filled with illite and/or sudoite crystals (Fig. 4A). The cleavage planes of muscovite
463 are partially to completely disrupted, and their birefringence colors approach those of illite, reflecting the onset of
464 muscovite illitization, particularly visible along grain margins (Figs. 4E, F, H, I). Under cross-polarized light, illite
465 occurs as lath-shaped crystals (Figs. 4E, F, H, I). Sudoite appears as needle-like crystals with low relief, generally
466 <2 μ m in length (Figs. 4B, C, H, I). Figure 5 highlights the effect of illite-sudoite alteration within a single sample
467 (MC-410-01, 677.9 m), comparing a relatively preserved zone showing the onset of alteration (Fig. 5A) with a
468 fully altered zone (Fig. 5B). Backscattered electron (BSE) images reveal that in the least altered area, muscovite
469 retains its characteristic cleavage planes (Fig. 5A), whereas in the most altered area, muscovite has completely lost
470 its original morphology and is replaced by sudoite \pm illite. Mixtures of these two phases can be distinguished
471 through grayscale contrast variations (Fig. 5B). Elemental X-ray maps obtained by EPMA further emphasize these
472 mineralogical and chemical transformations (Fig. 5C-H). In the least altered zone, muscovite exhibits variable K
473 (K α) intensities, with maximum values in the most preserved domains and progressively decreasing intensities in
474 areas showing incipient alteration (Fig. 5C). The Rb (K α) signal follows a similar pattern, reaching its highest
475 values in the K-rich zones (Fig. 5E). This decrease in K and Rb intensities correlates with the occurrence of Mg
476 (K α)-rich areas associated with sudoite formation along fracture zones (Fig. 5G). In the most altered zone,
477 muscovite relics (or “ghosts”) are identified by their relatively high K (K α) and Rb (K α) intensities (Fig. 5D, F),
478 which are spatially anti-correlated with the Mg (K α) signal. The latter reaches its maximum intensity within the
479 sudoite matrix that surrounds these muscovite remnants (Fig. 5H).



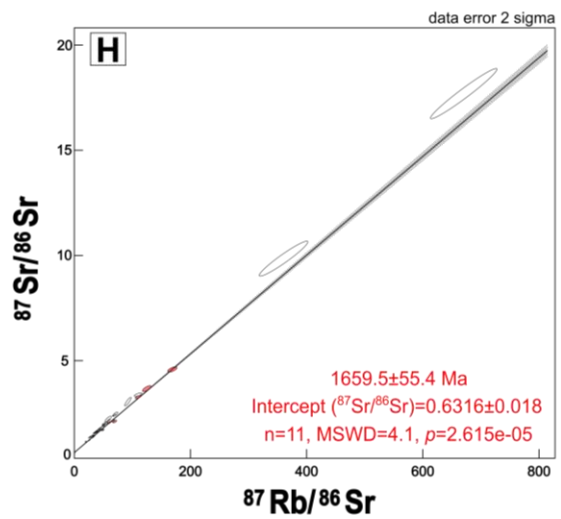
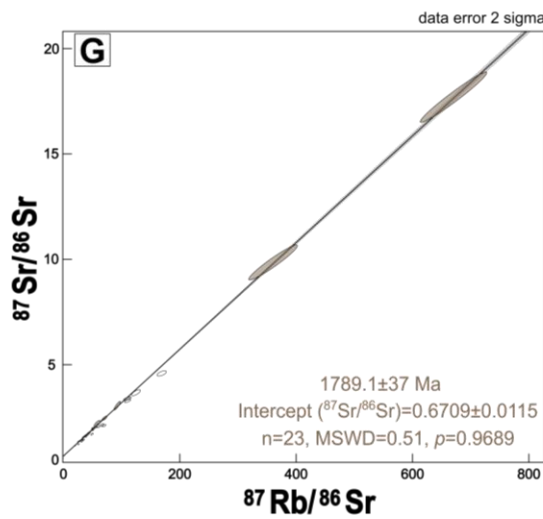
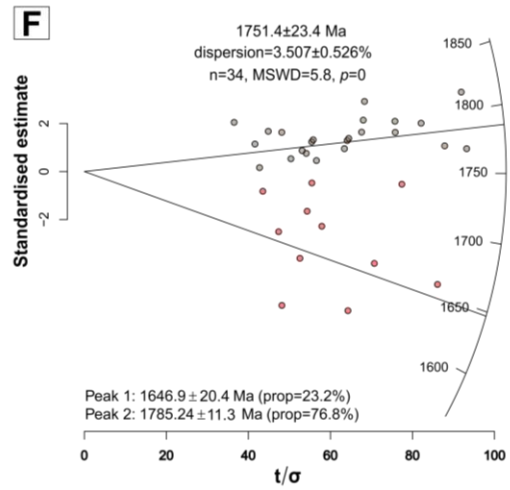
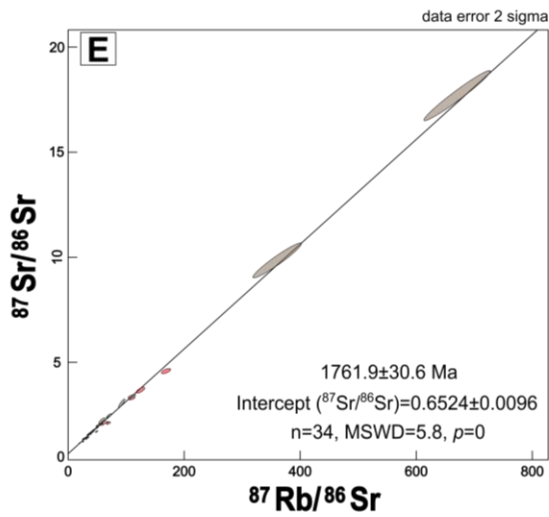
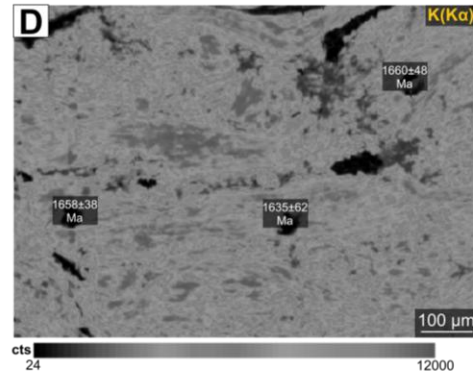
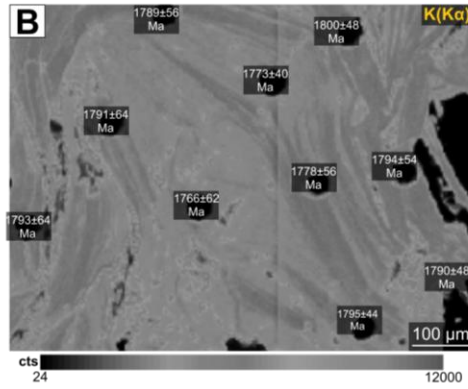
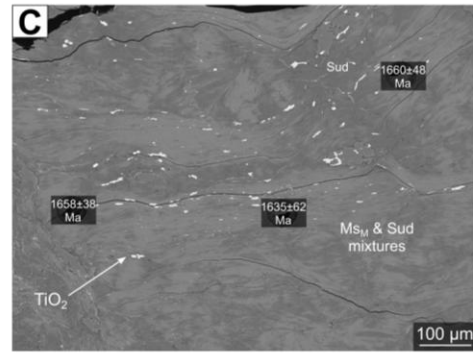
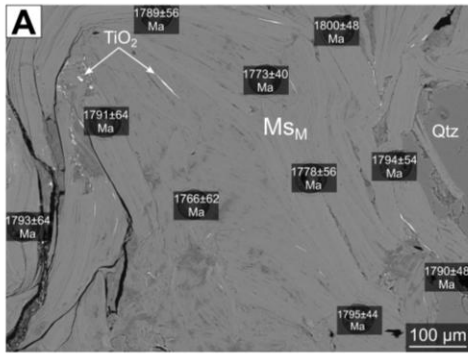
480

481 **Figure 5. Two zones within the same pelitic gneiss sample [MC-410-01, 677.9 m] are shown, ranging from weakly altered**
 482 **(A, C, E, G) to strongly altered by sudoite (B, D, F, H). (A) Preserved to partially preserved metamorphic muscovite**
 483 **(Ms_M) showing the onset of alteration to sudoite along fractures, expressed by darker grey tones. (B) Strongly altered**

484 metamorphic muscovite replaced by a sudoite-dominated matrix, containing very fine (<1 μm) TiO_2 exsolution lamellae
485 that formed from the alteration of muscovite. Circular holes correspond to 50- μm -diameter laser ablation pits. (C-D)
486 X-ray elemental maps of K ($\text{K}\alpha$) for (A) and (B), respectively. (C) Gradual decrease in apparent K concentration from
487 the fully preserved zone toward the incipiently altered domain. (D) K-enriched “ghosts” of muscovite, whereas altered
488 zones are strongly to entirely depleted in K. (E-F) X-ray elemental maps of Rb ($\text{K}\alpha$) acquired by EPMA for (A) and (B),
489 respectively. Apparent Rb concentration is higher in the most preserved zones in (E) and within muscovite ghosts in (D)
490 compared with illite-sudoite zones. (G-H) X-ray elemental maps of Mg ($\text{K}\alpha$) acquired by EPMA for (A) and (B),
491 respectively. (G) Zones filled with sudoite are highlighted by high apparent Mg concentrations. (H) Apparent Mg
492 concentration is maximal in sudoite-rich areas and anticorrelated with the K distribution shown in (D).

493 4.4. In situ Rb–Sr geochronology

494 Rb–Sr isotopic analyses were performed on metamorphic and early hydrothermal muscovite sampled from both
495 unaltered and illite-sudoite-altered zones, and from the two investigated lithologies (Supplement Table S1). To
496 assess the impact of the illite-sudoite alteration on the isotope system of basement minerals, a representative sample
497 of a pelitic gneiss (MC-410-01, at a depth of 677.9 m) containing both well-preserved (Fig. 6A, B) and partially
498 preserved to altered muscovite grains (Fig. 6C, D) was selected for detailed *in situ* analysis by LA-ICP-MS/MS.
499 The complete Rb–Sr dataset obtained from this sample defines a Rb–Sr regression corresponding to a date of
500 1761.9 ± 30.6 Ma ($n = 34$, MSWD = 5.8, $p \approx 0$, 2σ internal; ± 41.6 Ma including external reproducibility), with
501 $^{87}\text{Rb}/^{86}\text{Sr}$ ratios ranging from 19.62 to 670.44 and a corresponding $^{87}\text{Sr}/^{86}\text{Sr}$ intercept of 0.6524 ± 0.0096 (Fig. 6E).
502 The elevated MSWD value and the null probability associated with the reduced χ^2 test indicate significant excess
503 scatter in the isotopic data, consistent with heterogeneous isotopic behavior at the grain scale. Given this
504 dispersion, Rb–Sr single-spot dates were calculated for each laser ablation point following the approach of Röseler
505 and Zack (2022), allowing for a direct comparison between isotopic data, petrographic observations, and elemental
506 mapping. The resulting single-spot dates display a systematic relationship with K ($\text{K}\alpha$) intensity maps, showing a
507 decrease in apparent dates with decreasing K intensity, consistent with the progressive alteration of muscovite (Fig.
508 6B, D). Radial plots illustrating the distribution of single-spot dates and isotope ratios (Galbraith, 1988, 1990;
509 Röseler and Zack, 2022) reveal two statistically distinguishable populations with partial overlap: a dominant
510 population at 1785.2 ± 11.2 Ma (76.8%), corresponding predominantly to the least altered muscovite domains, and
511 a younger population at 1646.9 ± 20.4 Ma (23.2%), associated with increasingly altered domains (Fig. 6F). When
512 plotted separately on Rb–Sr regression diagrams, analyses from the least altered muscovite domains yield a
513 statistically robust regression corresponding to a date of 1789.1 ± 37 Ma ($n = 23$, MSWD = 0.51, $p = 0.9689$, 2σ
514 internal; ± 47 Ma including external reproducibility), with a $^{87}\text{Sr}/^{86}\text{Sr}$ intercept of 0.6709 ± 0.0115 (Fig. 6G). In
515 contrast, analyses from the more altered and mixed domains define a less statistically reliable regression at 1659.5
516 ± 55.4 Ma ($n = 11$, MSWD = 4.1, $p = 2.6 \times 10^{-5}$, internal; ± 61 Ma including external reproducibility), associated
517 with a $^{87}\text{Sr}/^{86}\text{Sr}$ intercept of 0.6316 ± 0.018 (Fig. 6H). The elevated MSWD values obtained for the altered domains
518 again indicate substantial isotopic scatter. On the basis of these observations and the coexistence of mixed isotopic
519 populations within a single sample, the analytical approach applied to the entire dataset, supported by petrographic
520 and microstructural evidence, consisted of distinguishing the most preserved metamorphic and early hydrothermal
521 muscovite from those more strongly altered by an illite-sudoite clay assemblage, in order to constrain the
522 crystallization dates of these two muscovite types and the potential timing(s) of alteration (Fig. 7A-E).



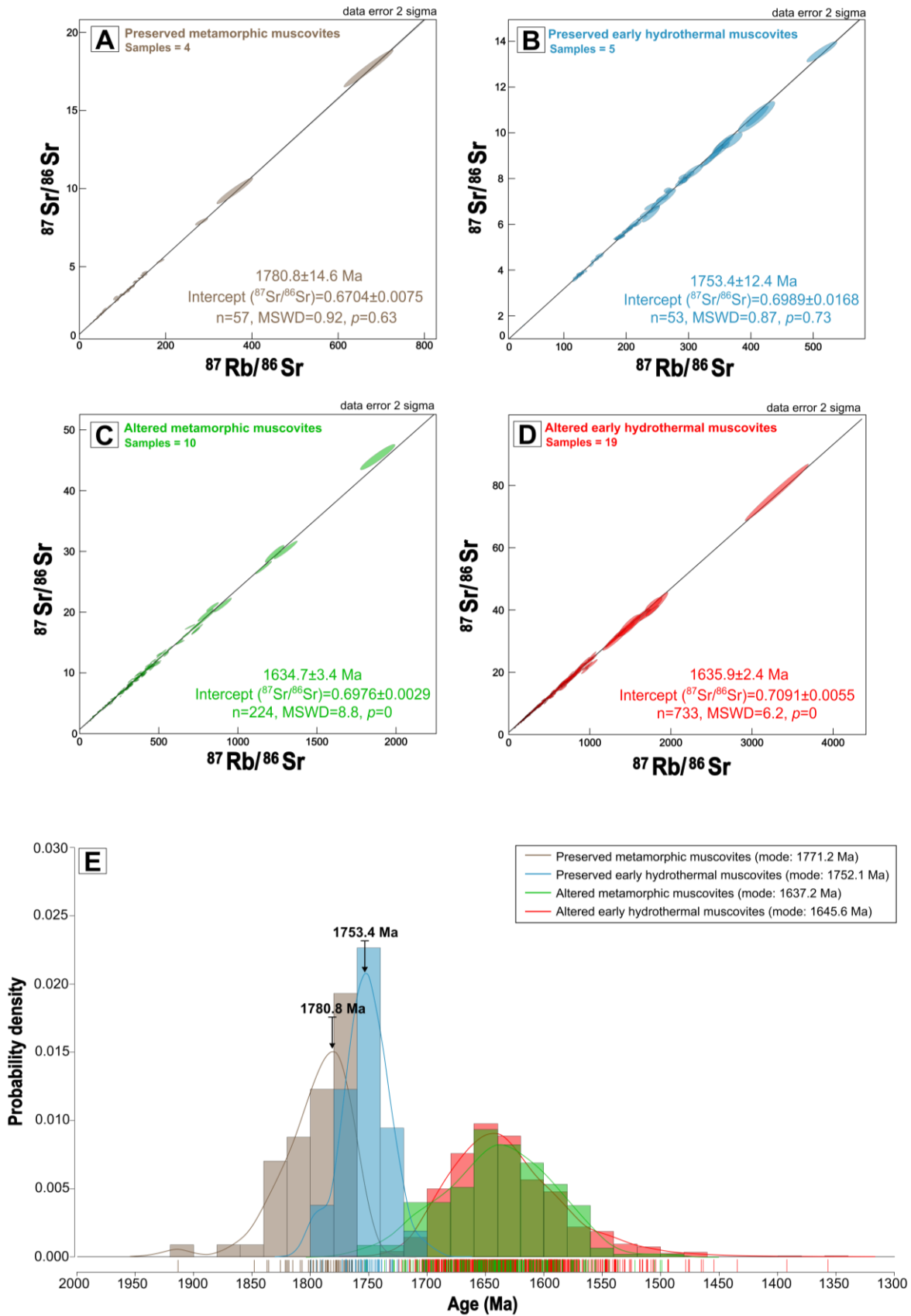
524 **Figure 6. (A-D) BSE images and corresponding X-ray elemental maps of K ($K\alpha$) acquired by EPMA for the pelitic gneiss sample [MC-**
525 **410-01, 677.9 m] shown in Fig. 5, displaying the calculated Rb–Sr single-spot dates (Rösel and Zack, 2022) for each ablation pit. (A-B)**
526 **The calculated Rb–Sr single-spot dates decrease toward zones exhibiting reduced apparent K concentrations. (C-D) The calculated**
527 **Rb–Sr single-spot dates are significantly younger in domains fully altered to sudoite compared to those in (A) and (B), which**
528 **correspond to preserved to partially preserved zones. (E) Muscovite Rb–Sr isochrons for the sample [MC-410-01, 677.9 m] obtained**
529 **from both preserved and altered areas. (F) Radial plot showing the dispersion of isotope ratios and calculated single-spot dates in**
530 **preserved and altered domains (Galbraith, 1988, 1990; Rösel and Zack, 2022), revealing two main populations. (G) Muscovite Rb–Sr**
531 **isochrons for preserved domains of the sample [MC-410-01, 677.9 m]. (H) Muscovite Rb–Sr isochrons for altered domains of the same**
532 **sample. Brown symbols correspond to preserved muscovite, and red symbols correspond to partially to completely altered muscovite.**
533 **All errors are reported at 2σ .**

534 **4.4.1. Rb–Sr dating of metamorphic muscovite**

535 The weighted mean of the Rb–Sr data obtained from all preserved metamorphic muscovite grains (four samples)
536 defines a composite Rb–Sr regression at 1780.8 ± 14.6 Ma ($n = 57$, $MSWD = 0.92$, $p = 0.63$, 2σ internal; ± 32 Ma
537 including external reproducibility), associated with a $^{87}\text{Sr}/^{86}\text{Sr}$ intercept of 0.6704 ± 0.0075 and overall $^{87}\text{Rb}/^{86}\text{Sr}$
538 ratios ranging from 19 to 671 (Fig. 7A). Rb–Sr single-spot dates for preserved metamorphic muscovite were
539 calculated using a fixed $^{87}\text{Sr}/^{86}\text{Sr}$ reference value of 0.6704, corresponding to the intercept of the composite
540 regression. This value is used here as an operational reference parameter; owing to its low magnitude, reasonable
541 variations in this parameter exert only a minor influence on the calculated dates, as previously demonstrated by
542 Rösel and Zack (2022). The resulting single-spot dates range from 1760 ± 30 Ma to 1914 ± 88 Ma and define a
543 single statistically coherent population with a modal value of 1771.2 Ma (Fig. 7E). Matrix-corrected elemental
544 concentrations (using an applied correction factor of 0.532038) range from 33 to 145 ppm (average: 81 ppm) for
545 ^{87}Rb , from 0.19 to 2.46 ppm (average: 1.03 ppm) for ^{86}Sr , and from 1.28 to 4.50 ppm (average: 2.73 ppm) for ^{87}Sr .

546 **4.4.2. Rb–Sr dating of early hydrothermal muscovite**

547 The weighted mean of the Rb–Sr data obtained from preserved early hydrothermal muscovite (five samples)
548 defines a composite regression at 1753.4 ± 12.4 Ma ($n = 53$, $MSWD = 0.87$, $p = 0.73$, 2σ internal; ± 31 Ma
549 including external reproducibility), associated with a $^{87}\text{Sr}/^{86}\text{Sr}$ intercept of 0.6989 ± 0.0168 and overall $^{87}\text{Rb}/^{86}\text{Sr}$
550 ratios ranging from 34 to 514 (Fig. 7B). Rb–Sr single-spot dates for preserved early hydrothermal muscovite were
551 calculated using the same fixed $^{87}\text{Sr}/^{86}\text{Sr}$ reference value of 0.6704, which has a negligible influence on the
552 resulting dates (e.g., Rösel and Zack, 2022). The calculated single-spot dates span from 1701.9 ± 57.6 Ma to 1799.5
553 ± 42.8 Ma and cluster into a single statistically consistent population with a modal value of 1752.1 Ma (Fig. 7E).
554 Matrix-corrected elemental concentrations (using an applied correction factor of 0.532038) range from 60.5 to
555 144.7 ppm (average: 111.3 ppm) for ^{87}Rb , from 0.22 to 2.26 ppm (average: 0.55 ppm) for ^{86}Sr , and from 1.82 to
556 3.97 ppm (average: 3.15 ppm) for ^{87}Sr .



557

558 Figure 7. (A) Rb–Sr isochrons for metamorphic muscovite preserved from illite-sudoite alteration, represented by four samples. (B)
559 Rb–Sr isochrons for early hydrothermal muscovite preserved from illite-sudoite alteration, represented by five samples. (C) Rb–Sr

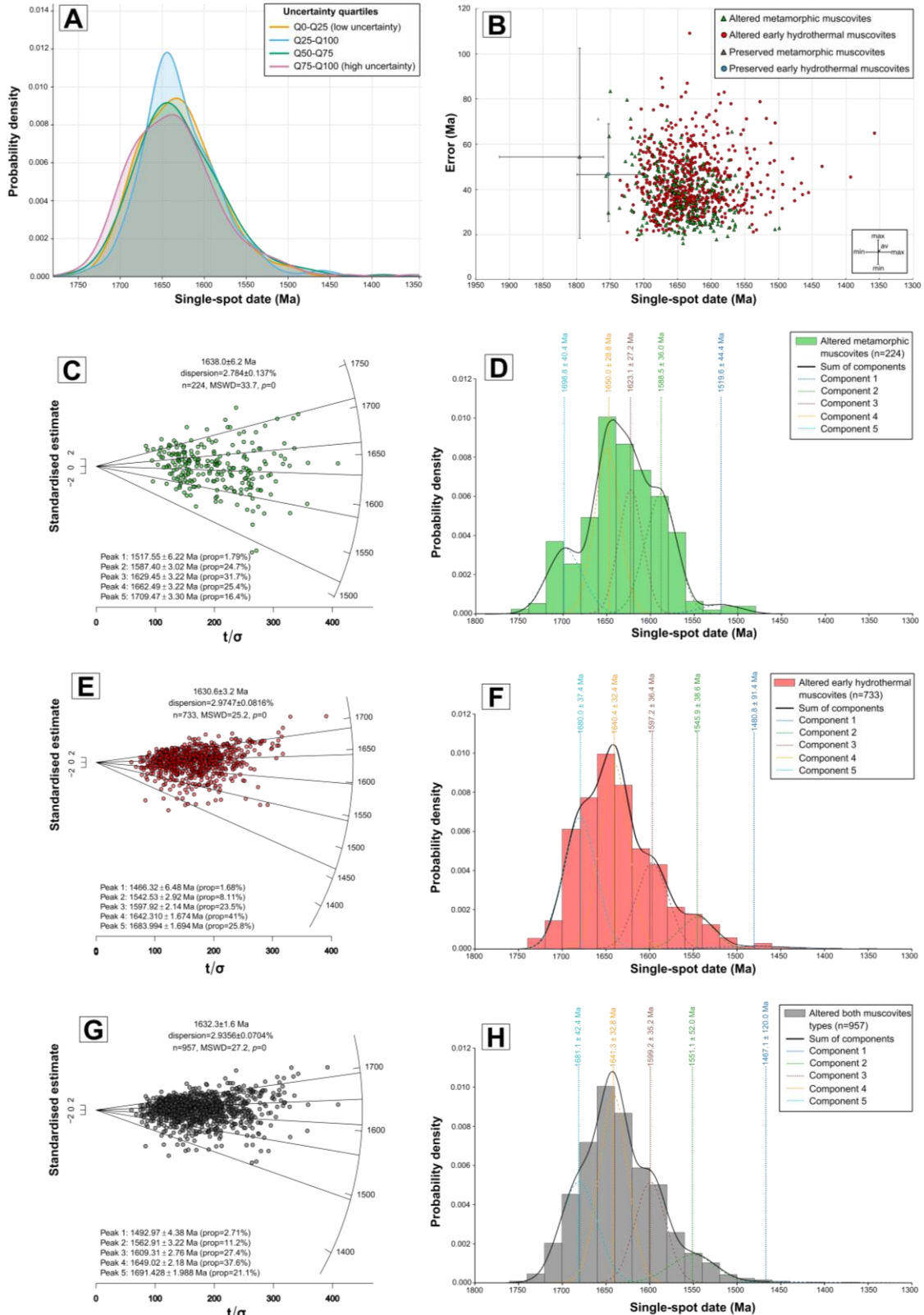
560 isochrons for metamorphic muscovite affected by illite-sudoite alteration, represented by ten samples. (D) Rb–Sr isochrons for early
561 hydrothermal muscovite affected by illite-sudoite alteration, represented by nineteen samples. (E) Density diagram constructed from
562 individual single-spot dates obtained for preserved metamorphic muscovite (brown), preserved early hydrothermal muscovite (blue),
563 illite-sudoite altered metamorphic muscovite (dark red), and illite-sudoite altered early hydrothermal muscovite (red). A bin width of
564 20 Ma was used for the histogram. The isochron dates calculated in (A) and (B) are indicated by bold arrows for the preserved
565 metamorphic and early hydrothermal muscovite.

566 4.4.3. Rb–Sr dating of altered muscovites

567 The weighted mean of the dates obtained for the metamorphic muscovite affected by illite-sudoite hydrothermal
568 alteration defines regressions at ca. 1635 Ma for metamorphic muscovite (ten samples, $n = 224$, $MSWD = 8.8$, p
569 $= 0$, 2σ internal; ± 26 Ma including external reproducibility) and at ca. 1636 Ma for early hydrothermal muscovite
570 (nineteen samples, $n = 733$, $MSWD = 6.2$, $p = 0$, 2σ internal; ± 26 Ma including external reproducibility),
571 associated with $^{87}\text{Sr}/^{86}\text{Sr}$ intercepts of 0.6976 ± 0.0029 and 0.7091 ± 0.0055 , respectively (Fig. 7C, D). The elevated
572 $MSWD$ values and null probabilities indicate significant excess scatter in both datasets for both muscovite types.
573 Single-spot Rb–Sr dates obtained from altered muscovite display a broad and erratic distribution, ranging from
574 1498.6 ± 22.8 Ma to 1756.2 ± 45.8 Ma (modal value of 1637.2 Ma) for metamorphic muscovite, and from 1357.0
575 ± 64.8 Ma to 1735.1 ± 43.8 Ma (modal value of 1645.6 Ma) for early hydrothermal muscovite (Fig. 7E). Matrix-
576 effect-corrected concentrations for the metamorphic muscovite range from 21.7 to 213.6 ppm (mean: 99.9 ppm)
577 for ^{87}Rb , from 0.10 to 3.74 ppm (mean: 0.62 ppm) for ^{86}Sr , and from 0.9 to 5.8 ppm (mean: 2.76 ppm) for ^{87}Sr .
578 Matrix-effect-corrected concentrations for the early hydrothermal muscovite range from 9.18 to 3222.9 ppm
579 (mean: 190.4 ppm) for ^{87}Rb , from 0.05 to 15.8 ppm (mean: 0.82 ppm) for ^{86}Sr , and from 0.44 to 75.4 ppm (mean:
580 4.95 ppm) for ^{87}Sr .

581 The analysis of calculated single-spot Rb–Sr dates as a function of uncertainty quartiles reveals an overall
582 homogeneous distribution, with moderate variations in central values and dispersion across uncertainty levels (Fig.
583 8A). The dataset was divided into four groups corresponding to the uncertainty quartiles (Q0–Q25, Q25–Q50,
584 Q50–Q75, and Q75–Q100). The group with the lowest uncertainty (Q0–Q25) comprises 241 observations, yielding
585 a mean date of 1633.3 Ma ($\sigma = 45.3$ Ma). The second quartile (Q25–Q50) includes 239 samples, with a mean date
586 of 1630.7 Ma ($\sigma = 44$ Ma). In the third quartile (Q50–Q75), the mean remains stable at 1630.6 Ma, although the
587 standard deviation increases slightly ($\sigma = 51.5$ Ma), reflecting greater variability. Finally, the quartile with the
588 highest uncertainty (Q75–Q100) encompasses 239 data points, showing a slightly higher mean date (1637.2 Ma)
589 and the greatest dispersion ($\sigma = 53.9$ Ma). Examination of the minimum and maximum values indicates a gradual
590 broadening of the single-spot Rb–Sr date distribution with increasing uncertainty, ranging from 1493.8 to 1752.7
591 Ma in the first quartile to 1357.0 to 1751.5 Ma in the last. This trend suggests that measurements associated with
592 higher uncertainties encompass a wider range of dates (Fig. 8B). Overall, the kernel density estimates (KDE) of
593 single-spot date distributions by quartile display relatively similar patterns, indicating no major bias related to
594 analytical uncertainty, although a slight increase in variability is observed. This observation highlights that, while
595 individual uncertainties do not significantly affect the mean of the single-spot dates, they are associated with
596 greater dispersion in the extreme values. To address the heterogeneous distribution of single-spot dates and the
597 variability of their individual uncertainties, a statistical approach based on a Gaussian Mixture Model (GMM) was
598 applied (McLachlan and Peel, 2000; Melnykov and Melnykov, 2012; Glodek et al., 2013; Nguyen and McLachlan,
599 2015; McLachlan et al., 2019). The GMM, applied to the logarithmically transformed Rb–Sr single-spot dates of

600 both muscovite types, enables the decomposition of the overall dataset into multiple components characterized by
601 distinct probabilistic centers. A suite of GMMs with varying numbers of Gaussian components was evaluated, with
602 model performance assessed using the Bayesian Information Criterion (BIC), which balances goodness of fit
603 against model complexity. Although solutions with different numbers of components were obtained, the five-
604 component model emerged most consistently across repeated runs and is therefore presented here. This
605 configuration is compatible with the number of populations identified from IsoplotR radial plots (Galbraith, 1988,
606 1990), providing a coherent basis for methodological comparison. The GMM-derived components were
607 subsequently examined in relation to the statistically coherent clusters defined by the radial plot approach, which
608 explicitly accounts for individual analytical uncertainties. Statistical analyses conducted on the hydrothermally
609 altered muscovite show good overall consistency between the date clusters identified by the radial plots (IsoplotR)
610 and those inferred from the GMM. For altered metamorphic muscovite, the radial plot reveals five statistical
611 groupings (Fig. 8C): 1517.6 ± 6.2 Ma (1.8 % of analyses), 1587.4 ± 3.0 Ma (24.7 %), 1629.5 ± 3.2 Ma (31.7 %),
612 1662.5 ± 3.2 Ma (25.4 %), and 1709.5 ± 3.4 Ma (16.4 %). The corresponding GMM also distinguishes multiple
613 components, including a dominant one at 1650.0 ± 28.8 Ma (33.3 %), and secondary components at 1698.8 ± 40.4
614 Ma (18.9 %), 1623.1 ± 27.2 Ma (24.5 %), 1585.5 ± 36.0 Ma (21.0 %), and 1519.6 ± 44.4 Ma (2.4 %) (Fig. 8D).
615 For altered early hydrothermal muscovite, the radial plot identifies five statistical clusters (Fig. 8E): 1466.3 ± 6.4
616 Ma (1.7 % of analyses), 1542.5 ± 3.0 Ma (8.1 %), 1597.9 ± 2.2 Ma (23.5 %), 1642.3 ± 1.6 Ma (41 %), and 1684.0
617 ± 1.6 Ma (25.8 %). The corresponding GMM also resolves several components, including a main one at $1640.4 \pm$
618 32.4 Ma (38.4 %), and secondary components at 1680.0 ± 37.4 Ma (31.7 %), 1597.2 ± 36.4 Ma (19.7 %), 1545.9
619 ± 38.6 Ma (8.1 %), and 1480.8 ± 91.4 Ma (1.8 %) (Fig. 8F). When combining the results for illite-sudoite zones
620 of both muscovite types, the radial plot identifies five statistical clusters (Fig. 8G): 1493.0 ± 4.4 Ma (2.7 % of
621 analyses), 1562.9 ± 3.2 Ma (11.2 %), 1609.3 ± 2.8 Ma (27.4 %), 1649.0 ± 2.2 Ma (37.6 %), and 1691.4 ± 2.0 Ma
622 (21.1 %). The corresponding GMM also distinguishes several components, including a dominant one at $1641 \pm$
623 32.8 Ma (37.6 %), and secondary components at 1681.1 ± 42.4 Ma (28.2 %), 1599.2 ± 35.2 Ma (23.7 %), $1551 \pm$
624 52 Ma (9.6 %), and 1467 ± 120 Ma (0.9 %) (Fig. 8H).



625

626

627

628

629

630

Figure 8. (A) Kernel density estimates (KDE) of calculated Rb–Sr single-spot dates for metamorphic and early hydrothermal muscovite affected by illite-sudoite alteration, sorted according to the quartiles of individual analytical uncertainties. The shape of the single-spot date distributions varies slightly with uncertainty level. Low uncertainties correspond to tightly clustered and homogeneous Rb–Sr single-spot dates, whereas high uncertainties are associated with greater dispersion and more pronounced asymmetry. (B) Scatter plot of analytical uncertainties versus Rb–Sr single-spot dates for altered metamorphic and early hydrothermal muscovite. For the

631 preserved metamorphic and early hydrothermal muscovites, the mean values of single-spot Rb–Sr dates and their associated analytical
632 uncertainties are reported, together with their respective maximum and minimum values. (C) Radial plot illustrating the dispersion of
633 isotope ratios and calculated single-spot dates for altered metamorphic muscovite. Five statistical populations are identified in the
634 radial plot. (D) Gaussian mixture model (GMM) applied to log-transformed dates, representing the distribution of Rb–Sr single-spot
635 dates of altered metamorphic muscovite, weighted by their uncertainties, together with the five components identified by the GMM.
636 (E) Radial plot showing the dispersion of isotope ratios and calculated single-spot dates for altered early hydrothermal muscovite. Five
637 statistical populations are identified. (F) Gaussian mixture model applied to log-transformed dates representing the distribution of
638 Rb–Sr single-spot dates for altered early hydrothermal muscovite, weighted by uncertainties, together with the five components
639 identified by the GMM. (G) Radial plot showing the dispersion of isotope ratios and calculated single-spot dates for altered
640 metamorphic and early hydrothermal muscovite combined. Five statistical populations are identified. (H) Gaussian mixture model
641 applied to log-transformed dates representing the distribution of combined altered metamorphic and early hydrothermal muscovite
642 Rb–Sr single-spot dates, weighted by uncertainties, as well as the five components identified by the GMM. The components identified
643 by the GMM closely correspond to the statistical populations defined by the radial plots, taking into account the associated
644 uncertainties. A bin width of 20 Ma was used for each GMM, consistent with the average of the individual analytical uncertainties
645 calculated for each spot.

646 **5. Discussion**

647 **5.1. Behavior of Rb and Sr and related Rb/Sr isotope system in muscovite from basement lithologies** 648 **affected by post-crystallization hydrothermalism**

649 The study of basement lithologies along a gradient from non-hydrothermally altered to strongly hydrothermally
650 altered zones beneath unconformity-type uranium deposits reveals significant mineralogical, geochemical, and
651 isotopic modifications. Across the four investigated sites, this alteration, macroscopically characterized by an
652 apple-green color affecting the foliation planes of metapelitic gneisses, leucosomes, and granitoids, as well as
653 filling fractures crosscutting the host lithologies (Figs. 2C, D, E, F and 4), manifests microscopically as the
654 progressive replacement of primary and retro-metamorphic minerals (plagioclase, K-feldspars, muscovite, biotite,
655 Fe-Mg chlorite) by an assemblage of illite and sudoite. Textural evidence suggests that these two minerals
656 crystallized synchronously or nearly synchronously (Pacquet and Weber, 1993; Percival and Kodama, 1989). This
657 alteration induces pronounced mineralogical transformations in both metamorphic and early hydrothermal
658 muscovite, involving a partial to complete breakdown of their crystal structure. This process is expressed either as
659 illitization initiated along the cleavage planes of muscovite, synchronous or quasi-synchronous with sudoite
660 precipitation, or as massive sudoite crystallization enveloping muscovite relics (Figs. 4 and 5B). Illite-sudoite
661 alteration constitutes the most pervasive and intense hydrothermal alteration affecting both the Athabasca Basin
662 sandstones and the underlying basement in the vicinity of unconformity-related uranium mineralization, and has
663 long been recognized as a robust exploration vector for U deposits (e.g., Carl et al., 1992; Derome et al., 2005;
664 Cloutier et al., 2009; Ng et al., 2013; Martz, 2017; Kaczowka, 2021; Powell et al., 2022). This alteration is
665 associated with a loss of Al, Na, K and Sr and a gain in Mg, Li and B (Martz et al., 2019a). The loss of K, Na, Al
666 and Sr is easily explained by the K-feldspars and plagioclases replacement by illite plus sudoite. Some of these
667 elements remain in the system and are in situ transferred to the newly-formed clays, whereas the rest leave the
668 system. This process results from the circulation of marine-derived basinal brines, generated during early to middle
669 diagenesis of the sedimentary basin (Hoeve and Sibbald, 1978; Kotzer and Kyser, 1995; Kyser et al., 2000).

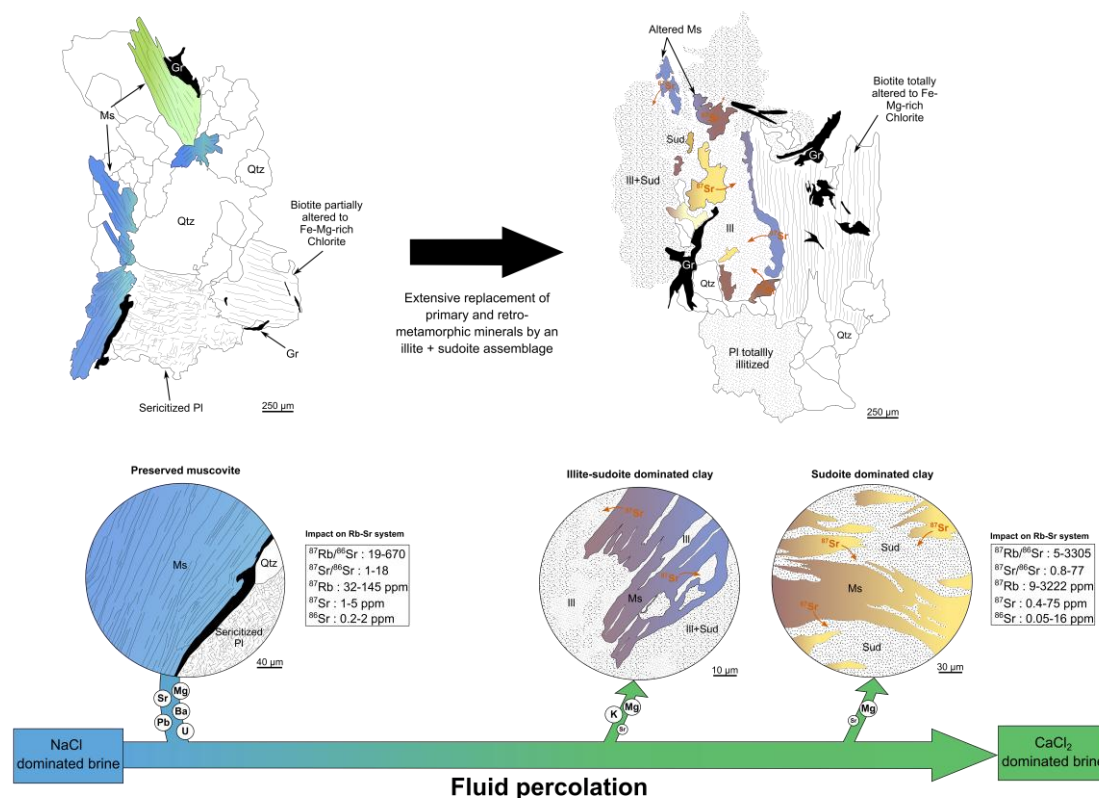
670 This illite + sudoite assemblage formed at temperatures between 150 and 220 °C, under pressures corresponding
671 approximately to the base of the sedimentary basin (ca. 0.1–0.3 GPa) (Halter, 1988; Kotzer and Kyser, 1995;

672 Cloutier et al., 2009; Martz, 2017). It is associated with important chemical modifications of the host rocks, notably
673 the loss of K, Na, Al, and Sr due to destabilization of primary feldspars and micas, and the concomitant gain in
674 Mg, Li, B, and Ca reflecting the composition of the basinal brine and its prolonged interaction with silicates. The
675 observed B and Mg enrichments are attributed to the intrinsic composition of the basinal fluid (Mercadier et al.,
676 2012; Richard et al., 2011) rather than to a local metamorphic source. Variations in the illite/sudoite ratio reflect
677 changes in thermal gradient (Beaufort et al., 2005; Kotzer and Kyser, 1995; Martz, 2017), in fluid composition
678 (Cloutier et al., 2009), notably the K^+/Mg^{2+} ratio, as well as in host rock lithology (Bruneton, 1993; Pacquet and
679 Weber, 1993; Mercadier et al., 2012; Cuney and Kyser, 2015; Martz, 2017) and system pH (Kyser et al., 2000;
680 Kister et al., 2005; Mercadier et al., 2012; Martz, 2017). The illite-sudoite alteration is not related to the
681 recrystallization of new generations of metamorphic or early hydrothermal muscovite but instead results from fluid
682 circulation that induces mineralogical, geochemical, and isotopic modifications. Isotopically, progressive
683 alteration leads to systematic variations in Rb–Sr systematics, as mineralogical transformations modify both
684 elemental concentrations and isotope ratios. The range of $^{87}Rb/^{86}Sr$ ratios broadens from 20–670 to 5–3305, while
685 $^{87}Sr/^{86}Sr$ ratios shift from 1.18 to 1.78, with corresponding single-spot dates decreasing from 1701.9–1914.8 to
686 1357.0–1756.2 Ma (Fig. 9). The behaviour of the Rb–Sr geochronometer in the presence of fluid-rock interaction
687 is best understood in terms of fluid-mediated recrystallization and open-system isotopic exchange, rather than
688 purely thermally-activated volume diffusion (Villa, 1998; Villa, 2022).

689 The observed shift in Rb–Sr systematics is primarily attributed to the partial to complete loss of radiogenic ^{87}Sr
690 from the system in response to fluid circulation associated with illite-sudoite alteration. This process results in
691 partial to complete resetting of the Rb–Sr isotope system (Matheney et al., 1990; Kalt et al., 1994; Evans et al.,
692 1995; Eberlei et al., 2015). Elemental maps further demonstrate that Rb is also mobile; however, the mobility of
693 radiogenic ^{87}Sr is significantly greater than that of Rb and non-radiogenic Sr. This contrast in mobility accounts
694 for the observed variations in both Rb/Sr ratios and Sr isotopic compositions (Fig. 5E and F) and could explain the
695 erratic data distribution. The structural destabilization of metamorphic and early hydrothermal muscovite during
696 hydrothermal alteration, facilitated by illitization and/or sudoitization along cleavage planes, may have enhanced
697 diffusion and leaching of radiogenic ^{87}Sr . This process likely promoted the transfer of ^{87}Sr into clay phases and/or
698 the fluid phase (Fig. 9). In addition, radiogenic ^{87}Sr produced in situ occupies the interlayer (I-site) in muscovite,
699 substituting for monovalent cations such as K^+ or Rb^+ (Brigatti and Guggenheim, 2002), whereas common Sr (^{86}Sr ,
700 ^{88}Sr) is predominantly hosted in the octahedral (M-site), where divalent cations are stable. This crystallochemical
701 distinction means that preferential removal of radiogenic ^{87}Sr from the I-site alone would be expected to drive the
702 regression intercept toward chondritic or higher values, not toward the sub-chondritic values observed here. The
703 anomalously low intercept values (~ 0.67) are therefore better interpreted as the result of isochron rotation under
704 open-system conditions involving non-conservative, grain-scale redistribution of both Rb and Sr (Brooks et al.,
705 1976; Villa, 1998; Villa, 2022), rather than as a direct consequence of selective I-site ^{87}Sr loss. As demonstrated
706 by Villa (1998, 2022), fluid-mediated recrystallization operates orders of magnitude faster than thermally-activated
707 volume diffusion and represents the dominant mechanism of isotopic exchange in micas affected by hydrothermal
708 fluids. In this framework, the structural destabilization of muscovite along cleavage planes during illitization and
709 sudoitization, facilitated by the circulating Ca-Cl₂-dominated brines, promoted fluid-assisted dissolution-
710 reprecipitation and non-conservative redistribution of Rb and Sr at the grain scale, consistent with the
711 hydrochronological framework described by Villa (2022). The transfer of Sr into the fluid phase is independently

712 supported by Sr enrichment documented in fluid inclusions from the Athabasca Basin brines (Mercadier et al.,
 713 2012; Richard et al., 2011; Martz, 2017).

714 Furthermore, the measured isotope ratios $^{87}\text{Rb}/^{86}\text{Sr}$ and $^{87}\text{Sr}/^{86}\text{Sr}$, as well as ^{87}Rb and ^{87}Sr concentrations, are
 715 significantly higher in altered muscovites than in unaltered muscovites. The simultaneous increase in $^{87}\text{Rb}/^{86}\text{Sr}$
 716 and $^{87}\text{Sr}/^{86}\text{Sr}$ ratios in muscovites affected by alteration or fluid circulation reflects reopening of the Rb–Sr system
 717 and selective mass redistribution of Sr during the hydrothermal event. Glodny and Grauert (2009) and Eberlei et
 718 al. (2015) demonstrate that such concurrent increases do not require mica recrystallization but rather result from a
 719 combination of dynamic fluid-rock interaction processes. These include: (i) a net loss of Sr through accelerated
 720 diffusion along defects (microfractures, cleavage planes, subgrains, dislocations), favoring the preferential loss of
 721 radiogenic Sr from transient interlayer sites or defect-related positions in muscovite; (ii) a decrease in the molar
 722 fraction of Sr, which automatically increases the $^{87}\text{Rb}/^{86}\text{Sr}$ ratio since Rb is relatively immobile; and (iii) a minor
 723 incorporation of Sr, possibly more radiogenic, from the matrix reservoir or from the fluid (e.g., derived from
 724 feldspar alteration) into altered muscovite, which can slightly increase the measured $^{87}\text{Sr}/^{86}\text{Sr}$ ratio.



725
 726 **Figure 9.** Schematic representation of the effect of illite-sudoite alteration on the Rb–Sr geochronometer in basement-hosted muscovite
 727 within the context of unconformity-related uranium deposits, resulting from the percolation of a Ca–Cl₂-dominated brine and fluid-
 728 rock interaction. This hydrothermal episode induces extensive replacement of primary and retro-metamorphic minerals by an illite-
 729 sudoite clay assemblage whose modal proportions vary among samples. The alteration fluid, which may circulate along pre-existing
 730 pathways generated during retro-metamorphic alteration of primary minerals, disrupts the crystal lattice of muscovite along cleavage
 731 planes. This structural breakdown leads to the loss of radiogenic ^{87}Sr from muscovite, which is redistributed into the fluid and/or the
 732 newly formed clay phases. Systematic fluid-inclusion studies (e.g., Mercadier et al., 2012; Richard et al., 2011; Martz, 2017) reveal that
 733 the regional brine, initially seawater-derived and NaCl-dominated, became progressively enriched in K, Sr, Mg, and B, and evolved
 734 toward a CaCl₂-dominated composition through prolonged interaction with the host rocks. This alteration episode also results in

735 increased Rb/Sr isotope ratios in muscovite, together with elevated ^{87}Rb and ^{87}Sr contents, which may be explained by Sr loss from the
736 muscovite molar fraction and by minor incorporation of Sr derived from either the rock matrix reservoir or the circulating fluid.

737 **5.2. Assessing the reliability and applicability of the Rb–Sr system in metamorphic and early** 738 **hydrothermal muscovite**

739 The characterization of well-preserved micro-domains enables the acquisition of statistically robust isotopic ages
740 for both the metamorphic muscovite associated with the foliation of metapelitic gneisses and the early
741 hydrothermal muscovite from anatectic granitoids or occurring in the leucosomes of metapelitic gneisses. These
742 muscovite grains preserved from illite-sudoite alteration define well-correlated Rb–Sr regressions yielding dates
743 of 1780.8 ± 14.6 Ma (2σ internal; ± 32 Ma including external reproducibility) and 1753.4 ± 12.4 Ma (2σ internal;
744 ± 31 Ma including external reproducibility), respectively (Fig. 7A, B). It should be noted that in open-system Rb–
745 Sr behaviour, fluid-rock interaction can rotate an originally valid isochron through non-conservative redistribution
746 of Rb and Sr at the grain scale, yielding geologically meaningful slopes but mathematically anomalous intercepts
747 that fall below physically feasible initial $^{87}\text{Sr}/^{86}\text{Sr}$ values (Brooks et al., 1976; Villa, 1998; Villa, 2022). As
748 demonstrated by Villa (1998, 2022), the isotopic perturbations formerly attributed to thermally-driven volume
749 diffusion in micas have since been shown to reflect fluid-mediated recrystallization, which operates orders of
750 magnitude faster than pure Fickian diffusion and represents the dominant mechanism of isotopic exchange in micas
751 affected by hydrothermal fluids. Such rotation does not invalidate the age information recorded by the slope of the
752 regression. However, the corresponding regression intercepts (0.6704 ± 0.0075 and 0.6989 ± 0.0168) fall below
753 the minimum $^{87}\text{Sr}/^{86}\text{Sr}$ value of the solar system (~ 0.698) and therefore cannot represent physically meaningful
754 initial isotopic compositions. These intercepts are thus not interpreted as true initial $^{87}\text{Sr}/^{86}\text{Sr}$ ratios but rather as
755 apparent values resulting from disturbed Rb–Sr systematics. Low MSWD values (< 1) and high p-values ($p \gg$
756 0.05) indicate strong internal coherence of the datasets, suggesting that the regressions are statistically robust
757 despite their anomalous intercepts. Such features are characteristic of rotated or disturbed isochrons formed under
758 open-system conditions, in which Rb and Sr are redistributed in a non-conservative manner (Brooks et al., 1976;
759 Faure and Mensing, 2013; Dickin, 2018). Proportional loss of Rb relative to Sr, selective Sr mobility during fluid-
760 rock interaction, or partial isotopic resetting during metamorphism may rotate an originally valid isochron, yielding
761 geologically reasonable slopes but non-physical intercepts (Brooks et al., 1976; DePaolo, 1981; Villa, 1998; Villa,
762 2022; Faure and Mensing, 2013). The reproducibility of measured $^{87}\text{Sr}/^{86}\text{Sr}$ ratios for the NIST SRM 610 reference
763 material, together with the consistency of the regression intercept obtained for the La Posta biotite reference
764 material, indicates that the measured $^{87}\text{Sr}/^{86}\text{Sr}$ ratios and derived regression intercepts are not attributable to
765 analytical bias or standardization issues, thereby effectively excluding an analytical or calibration-related origin.
766 Accordingly, the anomalously low intercept values are interpreted as mathematical artefacts arising from open-
767 system Rb–Sr behavior and isochron rotation under fluid-mediated conditions, rather than as geologically
768 meaningful isotopic signatures or evidence of an analytical artefact. In contrast, the slopes of the regressions may
769 still record geologically significant timing information related to muscovite crystallization or partial isotopic
770 resetting, as has been documented in other disturbed Rb–Sr systems (Brooks et al., 1976; Villa, 1998; Villa, 2022;
771 Zack and Hogmalm, 2016).

772 The single-spot ages obtained from metamorphic muscovite developed along foliation planes in Paleoproterozoic
773 pelitic gneisses (e.g., Schneider et al., 2007; Skipton et al., 2016; Jeanneret et al., 2017; Martz, 2017) range from

774 1914 ± 44 Ma to 1760 ± 15 Ma, with a modal value of 1771.2 Ma and an isochron age of 1780.8 ± 14.6 Ma (2σ
775 internal; ±32 Ma including external reproducibility) (Fig. 10). The mean age derived from single-spot analyses,
776 together with the isochron age, falls within the temporal window of the M2-D2 event, which generated the
777 northeast-striking structural trend of the WMTZ and formed under a sinistral transpressional tectonic regime
778 during the late stages of the oblique Hudsonian collision, between ca. 1813 and 1770 Ma (Fig. 10).
779 Thermobarometric estimates indicate that rocks of the study area were re-equilibrated under conditions of ca. 0.5
780 GPa and 750–825 °C at this time (Annesley et al., 1992, 1997a,b,c, 1999a,b; Jeanneret et al., 2017; Toma et al.,
781 2024). The M2-D2 temporal interval is supported by geochronological constraints derived from other mineral
782 phases using various U–Pb chronometers, including monazite (Pb diffusion at ca. 500–800 °C; e.g., Cherniak et
783 al., 2004; McFarlane and Harrison, 2006), zircon (>900 °C; Cherniak and Watson, 2001), and titanite (500–800
784 °C; Kohn, 2017). The distribution of Rb–Sr single-spot ages in metamorphic muscovite is shifted toward the lower
785 limit of this time window (Fig. 10) and reflects the neof ormation of muscovite along the retrograde *P-T* path
786 (≤~700 °C), possibly in the presence of fluids and the cooling of muscovite below the closure temperature of the
787 Rb–Sr system, estimated at ca. 450–600 °C (Dodson, 1973). Above this closure temperature, Sr diffusion remains
788 sufficiently rapid to maintain an open isotope system, allowing equilibration with the surrounding matrix or
789 between minerals.

790 In contrast, the single-spot ages measured in early hydrothermal muscovite crystallized within anatectic granitoids
791 or within leucosomes of metapelitic gneisses (e.g., Schneider et al., 2007; Skipton et al., 2016; Martz, 2017) range
792 from 1799.5 ± 21.4 Ma to 1701.9 ± 28.8 Ma, with a mode at 1752.1 Ma and an isochron age of 1753.4 ± 12.4 Ma
793 (2σ internal; ±31 Ma including external reproducibility) (Fig. 10). The mean age derived from single-spot
794 analyses, together with the isochron age, falls within the temporal window of the exhumation and orogenic cooling
795 phase of the Trans-Hudsonian orogen, a period characterized by the end of migmatization with the crystallization
796 of leucosomes, the emplacement of leucogranitic intrusions, and the onset of hydrothermal activity associated with
797 the cooling phase. Although its precise duration remains poorly constrained, this cooling interval is typically
798 considered to span from ca. 1770 Ma (750 °C, 0.5 GPa) to ca. 1720 Ma (350 °C, 0.2 GPa), as documented in
799 several studies (Annesley and Madore, 1994; Annesley et al., 1992, 1997a, b, c; Annesley et al., 2005; Jeanneret
800 et al., 2017; Martz, 2017). The end of this period is associated with pronounced retrograde transformations,
801 including the breakdown of cordierite to phyllosilicates, biotite chloritization, sulfide, graphite and muscovite
802 precipitation, quartz-rich fluid circulation, and dissolution-reprecipitation of monazite and zircon (Card, 2012,
803 2014; Card and Noll, 2016). These processes are further constrained by cooling ages obtained from Rb–Sr biotite
804 (Worden et al., 1985; Schneider et al., 2007), K–Ar muscovite (Philippe et al., 1993), and Ar–Ar muscovite
805 (Alexandre et al., 2009). This timeframe has also been interpreted as reflecting a late thermal event associated with
806 the emplacement of the Kivalliq Igneous Suite (KIS) to the northeast of the Athabasca Basin, with the Wollaston
807 Domain being intruded by the Nueltin Granite of the same suite (ca. 1770–1730 Ma), which may have reset U–Pb
808 metamorphic rutile ages (Adlakha and Hattori, 2021). Additionally, hydrothermal graphite, commonly spatially
809 associated with early hydrothermal muscovite within the Wollaston-Mudjatik Transition shear zones, yields highly
810 precise (<1 %) Re–Os isochron ages of 1731.5 ± 7.4 Ma (2σ; MSWD = 1.3). These ages are interpreted to record
811 graphite formation during the exhumation and orogenic cooling phase of the THO (Martz, 2017) and/or a period
812 of elevated heat flow associated with the KIS emplacement (Adlakha and Hattori, 2021), wherein aqueous fluids
813 mobilized carbon from adjacent wall rocks into semi-brittle to brittle-ductile shear zones (Toma et al., 2022).

814 Overall, the Rb–Sr single-spot ages of early hydrothermal muscovite are consistent with the exhumation and
815 orogenic cooling stage of the THO, during which anatectic granitoids were emplaced and/or magmatic activity of
816 the Kivalliq Igneous Suite occurred, and they further align with the circulation of carbon-bearing aqueous fluids
817 responsible for the formation of hydrothermal graphite. Comparison of the Rb–Sr ages obtained from alteration-
818 free metamorphic and early hydrothermal muscovite with existing literature datasets indicates that the Rb–Sr
819 system constitutes a suitable geochronometer in this geological context, as evidenced by the reproducibility of
820 comparable Rb–Sr ages across four distinct sites within the WMTZ of the THO (Fig. 10).

821 **5.3. Assessing the reliability and applicability of the Rb–Sr system to date hydrothermal system in** 822 **crystalline basement**

823 Variably altered muscovite crystals occurring in illite-sudoite hydrothermal alteration zones in the four study sites
824 along the WMTZ in the eastern Athabasca Basin display highly scattered Rb–Sr single-spot dates and substantial
825 individual uncertainties, ranging from 1756.2 ± 45.8 to 1357.0 ± 64.8 Ma. Despite this variability, muscovite from
826 both altered pelitic and granitic protoliths shows comparable Rb–Sr single spot data distributions. Gaussian
827 Mixture Modelling (GMM) and radial plot analysis define five statistically coherent populations shared by both
828 muscovite generations affected by illite-sudoite alteration. However, their geochronological resolution is
829 intrinsically limited because the analytical uncertainties are large. This reflects the inherent difficulty of precisely
830 dating Paleoproterozoic geological events, as all isotope system tend to yield significant errors at such ancient ages
831 (e.g., Fayek and Riciputi, 2002; Alexandre et al., 2005; Rainbird et al., 2007; Schneider et al., 2007; Davis et al.,
832 2011; Jeanneret et al., 2017; Adlakha and Hattori, 2021; Toma et al., 2022). The identification of five sub-
833 populations does not imply that this is the only possible partitioning, but rather the one favored by the model under
834 the present configuration, given the single-spot age values and their associated uncertainties. Small sub-
835 populations should likewise be interpreted cautiously: although they may correspond to genuine age modes, they
836 may also reflect asymmetries, outliers, or an artificial segmentation of an otherwise continuous distribution.
837 Several studies have demonstrated that Gaussian mixture models can generate artificial components when fitting
838 continuous or asymmetric distributions (McLachlan & Peel, 2000; Bishop, 2006; Hastie et al., 2001). When
839 substantial overlap exists between Gaussian components, the model often represents a single underlying population
840 using multiple components (Fraley & Raftery, 2002). Ultimately, the components should be regarded primarily as
841 probabilistic centers, which we attempt to compare with published datasets from the literature (Figs. 8, 10). It
842 should be noted that BIC-based GMM algorithms tend to overestimate the number of populations with increasing
843 sample size (Vermeesch, 2018), and that the present data are equally consistent with a smaller number of broader,
844 partially overlapping distributions. The age components identified here are therefore not interpreted as discrete
845 geological events but as probabilistic centers whose significance is evaluated through their correspondence with
846 independently dated tectono-hydrothermal events documented in the regional record.

847 A dominant population at ca. 1640 Ma, representing the majority of the dataset and potentially overlooked without
848 prior petrographic constraints, is consistently recorded across four independent sites within the WMTZ of the
849 THO, supporting the regional significance and robustness of this age population. This main cluster is accompanied
850 by subordinate age groups at ca. 1680 Ma, ca. 1600 Ma, ca. 1550 Ma, and by a minor population near ca. 1467
851 Ma, which display limited inter-site variability and likely reflect local heterogeneities or superimposed geological
852 processes. These ages fall within the post-Athabasca Basin evolution, following basin deposition between ca. 1760

853 and 1720 Ma (Ramaekers et al., 2007; Jeanneret et al., 2016) and continuing until ca. 1541 Ma (Creaser and
854 Stasiuk, 2007). The data obtained in strongly illite-sudoite-altered zones of the basement, spatially associated with
855 the uranium mineralization, record extensive mineralogical transformations and major geochemical and isotopic
856 modifications driven by the circulation of basinal brines; i.e., the same fluids responsible for the characteristic
857 illite-sudoite alteration halos observed around all unconformity-related uranium deposits in the eastern Athabasca
858 Basin. The spread of the Rb–Sr single-spot dates may reflect either a single, long-lived fluid-rock interaction event
859 with a paroxysm at ca. 1640 Ma, or a sequence of pulsed hydrothermal episodes represented by the GMM and
860 radial plot populations.

861 The main peak at ca. 1640 Ma is widely recognized across the basin as marking a major sedimentary reorganization
862 event associated with a rapid westward deepening and the deposition of deeper-water successions (ca. 1664–1590
863 Ma; e.g., Pehrsson et al., 2023). This structural tilting correlates with the Racklan-Forward orogeny (ca. 1660–
864 1590 Ma; e.g., Furlanetto et al., 2016; Pehrsson et al., 2023), a far-field intracontinental compressional event that
865 reactivated deep crustal faults and deformed the northern Laurentian basement. Within the same time interval,
866 zircon extracted from reworked tuff intraclasts of the Wolverine Point Formation (member b) yields a weighted
867 mean $^{207}\text{Pb}/^{206}\text{Pb}$ age of 1644 ± 13 Ma (2σ), interpreted as the crystallization age of the original tuff layers
868 (Rainbird et al., 2007; Fig. 10). These tuffs are considered to be correlative with the Yavapai and Mazatzal
869 Paleoproterozoic orogens, particularly within the Cochise block of the Mazatzal orogen, where juvenile arc
870 terranes and syntectonic plutons range from ca. 1660 to 1600 Ma (Sims and Peterman, 1986; Karlstrom and
871 Bowring, 1988; Eisele and Isachsen, 2001; Rainbird et al., 2007). In a broader geodynamic framework, this event
872 may also be linked to the Racklan Orogeny of northwestern Laurentia, interpreted as the northwestern continuation
873 of the Mazatzal orogenic system. Together, these orogenic events define a large-scale Paleoproterozoic
874 accretionary system that affected the margins of the Canadian Shield and promoted significant crustal reworking,
875 consistent with the hypothesis of a circum-Laurentian orogenic belt (e.g., Furlanetto et al., 2013). U–Pb data
876 obtained from fluorapatite in the Athabasca Basin indicate a coherent phase of phosphate cementation, constrained
877 by weighted mean $^{207}\text{Pb}/^{206}\text{Pb}$ ages obtained on apatite with high radiogenic-to-common Pb ratios, and by Pb–Pb
878 regression lines that are independent of common Pb (e.g., Davis et al., 2011). Fluorapatite from the Smart, Manitou
879 Falls, and Wolverine Point formations of the Athabasca Basin yields ages of 1609 ± 30 Ma, 1638 ± 12 Ma, and
880 1625 ± 17 Ma, respectively, clustering around a mean age of approximately 1630 ± 9 Ma (e.g., Davis et al., 2011;
881 Fig. 10). These ages are interpreted to record a basin-wide circulation of warm, oxidizing, P-rich brines produced
882 by fluid-rock interactions between basinal brines and the altered crystalline basement during mesogenetic
883 diagenesis. This large-scale fluid circulation is likely tectonically driven and related to the regional geodynamic
884 evolution of the basin, as proposed by Pehrsson et al. (2023), and can be temporally constrained to ca. 1640 Ma
885 based on the concordance between Rb–Sr and U–Pb apatite ages.

886 Taken together, these observations support the interpretation of a major basin-wide hydrothermal event at ca. 1640
887 Ma. Illite-sudoite alteration dated at ca. 1640 Ma can be interpreted in two alternative, but not mutually exclusive,
888 ways. First, this alteration may predate the main stage of uranium oxide precipitation, commonly dated between
889 ca. 1590 and 1200 Ma based on U–Pb analyses of uraninite and K–Ar/Ar–Ar geochronology of clay minerals
890 (Cumming and Krstic, 1992; Philippe et al., 1993; McGill et al., 1993; Fayek and Riciputi, 2002; Alexandre et al.,
891 2009; Cloutier et al., 2011; Powell et al., 2022). In this scenario, the ca. 1640 Ma illite-sudoite alteration would
892 represent a basin-scale hydrothermal event that prepared the basement-basin interface for subsequent uranium

893 mineralization by enhancing permeability, redox reactivity, and uranium mobility. Alternatively, the 1640 Ma
894 alteration may record an early phase of uranium mineralization itself, subsequently overprinted and partially reset
895 by younger tectono-hydrothermal events. Such a model is consistent with studies demonstrating that the U–Pb
896 systematics of uraninite and associated alteration minerals in unconformity-related uranium deposits are
897 commonly affected by multiple fluid-flow episodes, leading to partial Pb loss and a wide dispersion of apparent
898 ages (Kotzer and Kyser, 1990; Fayek and Kyser, 1997; Fayek et al., 2002; Fayek and Riciputi, 2002; Kyser et al.,
899 2015). Consequently, an older hydrothermal and/or mineralizing system active during the ca. 1680–1640 Ma
900 interval cannot be excluded, but may remain cryptic due to subsequent uranium remobilization and isotopic
901 resetting during younger basin-wide fluid circulation events. This interpretation is further supported by analogues
902 from northern Australia, where *in situ* U–Pb analyses of uraninite indicate initial mineralization or hydrothermal
903 alteration as early as ca. 1680–1640 Ma, followed by multiple resetting episodes extending into the
904 Mesoproterozoic and Paleozoic (Clauer et al., 2015; Skirrow et al., 2016).

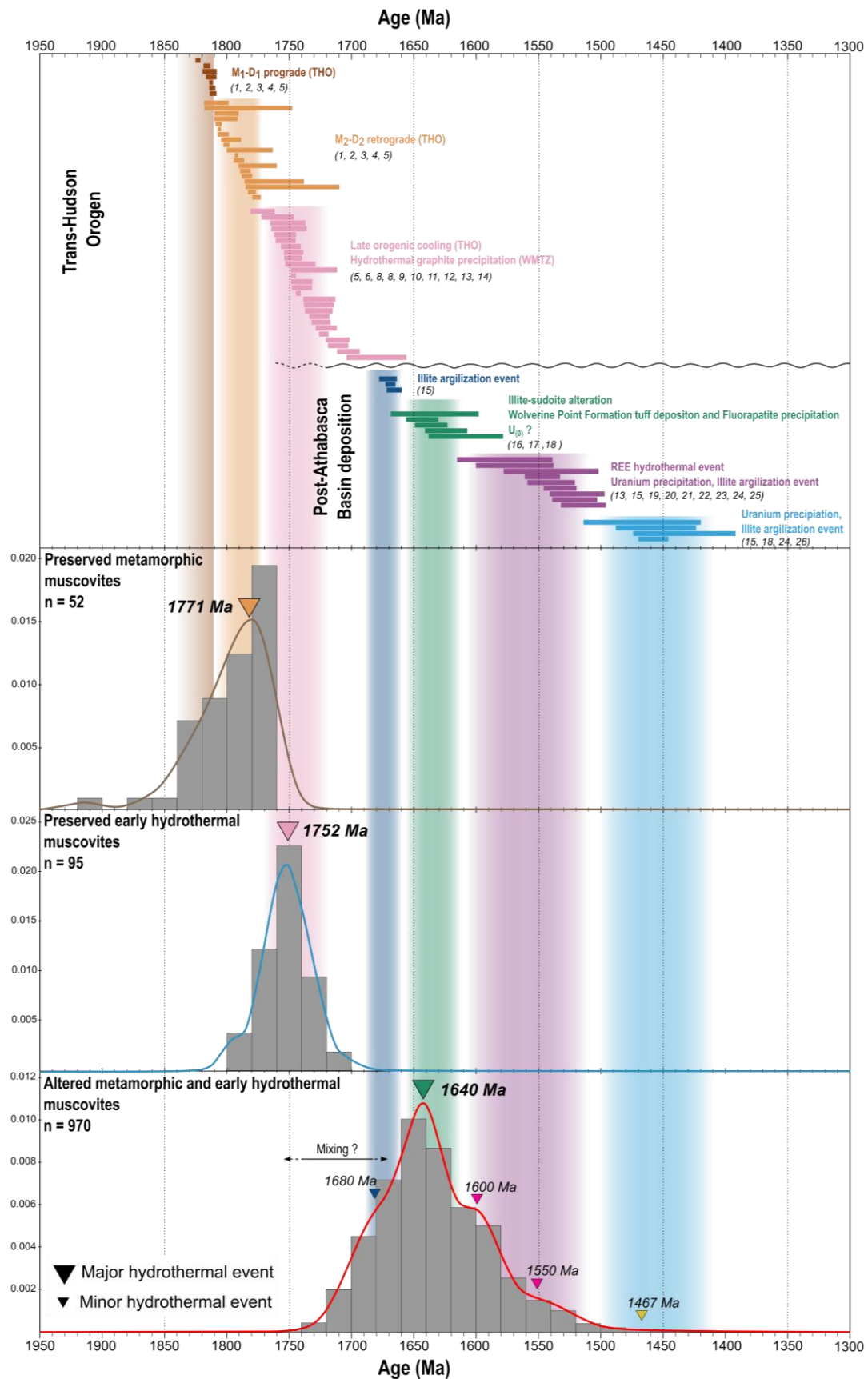
905 In addition to the main population associated with illite-sudoite alteration at ca. 1640 Ma, several consistent
906 statistical sub-populations are identified by the GMM. However, no chemical or mineralogical modifications are
907 observed in the zones where these single-spot data were measured. A first sub-population calculated around ca.
908 1680 Ma can be interpreted in two ways. It may represent a mixed population between preserved and altered data
909 (Fig. 6F), reflecting the onset of alteration and a partial loss of radiogenic ^{87}Sr caused by this early alteration stage
910 at ca. 1640 Ma. Such mixing would tend to skew the single-spot Rb–Sr dates of metamorphic muscovite, which
911 crystallized prior to early hydrothermal muscovite, toward older dates. Alternatively, this ca. 1680 Ma population
912 could correspond to an argillization episode dated to this period by Alexandre et al. (2009) using Ar–Ar analyses
913 on basement-hosted illite, which yields pseudo-plateau ages at McArthur River of 1669 ± 4 Ma, 1666 ± 6 Ma, and
914 1671 ± 7 Ma, interpreted as a pre-ore alteration event (Fig. 10). However, the actual geological significance of
915 each published age and its attribution to a specific event are often difficult to evaluate in this context, due to
916 successive episodes of intense fluid circulation and associated fluid-rock interaction processes that promote
917 substantial Ar loss and consequently yield younger ages (Chi et al., 2018). Nevertheless, during this time interval,
918 the basin is characterized by a half-graben architecture, with sediment transport predominantly directed toward the
919 northwest and enhanced sediment accumulation along the southeastern basin margin. This configuration reflects
920 an intracontinental extensional regime established after the THO orogeny, which may have facilitated the
921 circulation of early fluids within the basement and may also have reset the Rb–Sr system.

922 The younger age populations at ca. 1600–1550 Ma are consistent with hydrothermal and mineralizing events that
923 have been independently documented throughout the Athabasca Basin. The sub-populations at ca. 1600 Ma and
924 ca. 1550 Ma document hydrothermal activity previously identified in the Athabasca Basin and its underlying
925 basement, although it remains unclear whether they reflect a single event, a series of pulsatile episodes, or
926 processes potentially related to, or distinct from, the ca. 1640 Ma event. This hydrothermal activity is highlighted
927 in the basement by anatase precipitation, a low-pressure, low-temperature TiO_2 polymorph, yielding a weighted
928 mean $^{207}\text{Pb}/^{206}\text{Pb}$ age of 1569 ± 31 Ma (MSWD = 0.30, $n = 5$, 2σ ; Adlakha and Hattori, 2021, Fig. 10). This age
929 has been interpreted as reflecting the onset of oxidizing hydrothermal activity in the basement, contemporaneous
930 with U precipitation at the world-class McArthur River deposit, which has been dated by U–Pb analyses of U
931 oxides with two discordant ages of 1540 ± 19 Ma (Alexandre et al., 2009) and 1540 ± 38 Ma (Alexandre et al.,
932 2005). Additional ages at ca. 1520 Ma, including 1514 ± 18 Ma (Cumming and Krstic, 1992), 1519 ± 22 Ma

933 (Fayek and Riciputi, 2002), and 1521 ± 18 Ma (McGill et al., 1993), have been interpreted as minimum
934 crystallization ages for primary uraninite. An episode of argillization contemporaneous with these fluid-circulation
935 events has also been identified at 1577 ± 38 Ma (K–Ar muscovite from gneiss; Philippe et al., 1993) at Cigar Lake,
936 and at 1533 ± 13 Ma (Ar–Ar on illite; Alexandre et al., 2009) at McArthur River. A further rare-earth-phosphate
937 hydrothermal episode is documented in the eastern Athabasca Basin within the Maw Zone rare-earth-element
938 deposit. U–Pb dating of xenotime yields a $^{207}\text{Pb}/^{206}\text{Pb}$ age of 1547 ± 14 Ma (Rabiei et al., 2017; Fig. 10), and both
939 isotopic signatures and fluid-inclusion characteristics support the interpretation that the fluids responsible for
940 xenotime precipitation were part of the same oxidizing-reducing hydrothermal system involved in the development
941 of major uraninite mineralization across the Athabasca Basin. More broadly, these events are associated with a
942 renewed phase of subsidence and marine flooding, attributed to intracontinental rifting or extension and linked to
943 the emplacement of the Kuungmi Formation basalts in the adjacent Thelon Basin. This rifting episode coincides
944 with a reorganization of the Laurentian crust following the Australia-Laurentia collision, and precedes the
945 stabilization of Nuna, potentially promoting large-scale fluid circulation through both the basement and the basin,
946 capable of resetting the Rb–Sr geochronometer in muscovite.

947 Finally, the minor age population at ca. 1467 Ma may correspond to an early mineralization event, as recorded by
948 discordant U–Pb ages of 1467 ± 47 Ma at the Cigar Lake deposit (Fayek and Riciputi, 2002) and by weighted
949 mean $^{207}\text{Pb}/^{206}\text{Pb}$ ages of 1458 ± 12 Ma at the McArthur River deposit (Kister, 2003). An argillization event
950 contemporaneous with these fluid-circulation episodes has also been identified at 1456 ± 32 Ma (K–Ar on the <2
951 μm fraction from gneiss; Philippe et al., 1993) at Cigar Lake, and at 1433 ± 31 Ma (Ar–Ar on illite; Alexandre et
952 al., 2009) at McArthur River. Overall, current data do not allow discrimination between a single protracted fluid-
953 rock interaction episode at ca. 1640 Ma leading to the formation of an illite-sudoite alteration halo and multiple
954 episodic fluid pulses to account for the Rb–Sr single-spot age distribution in altered metamorphic and early
955 hydrothermal muscovite. Nevertheless, these results clearly demonstrate the applicability of the Rb–Sr
956 chronometer for constraining hydrothermal fluid circulation at basin-basement interfaces. The distinct age
957 populations identified in muscovite and alteration products correspond to tectono-hydrothermal events that are
958 independently recognized in the regional geological record and have been previously dated using other
959 geochronological methods. Comparable multi-stage fluid-thermal histories have been documented in other
960 hydrothermal systems, such as gold deposit systems, where primary mineral phases commonly preserve evidence
961 for repeated isotopic resetting, trace-element redistribution, and microstructural overprinting associated with
962 episodic fluid and heat input (e.g., Bevan et al., 2021; Chen et al., 2024; Drake et al., 2023; Huang et al., 2023;
963 Liu et al., 2018; Mao et al., 2013; Olierook et al., 2020; Redaa et al., 2021, 2022; Şengün et al., 2019; Wang et al.,
964 2022; Zametzer et al., 2022; Tian et al., 2024; Boschetti et al., 2025; Huang et al., 2025). Such behaviour
965 underscores the capacity of mineral-scale chronometers to resolve protracted hydrothermal evolution. In this
966 context, the present data suggest that the Rb–Sr system in muscovite and alteration minerals is sensitive to
967 successive hydrothermal events at basin-basement interfaces, highlighting its potential as a robust tool for
968 reconstructing the timing and duration of fluid circulation processes, while emphasizing the need for further work
969 to evaluate mineralogical and geochemical controls on system behaviour. Although these initial results are
970 promising, further work is required to assess potential mineralogical or geochemical specificities that may
971 influence the Rb–Sr system under such conditions.

972



973

974 **Figure 10. Compilation of published geochronological constraints for the Trans-Hudson orogen and the Athabasca Basin, integrated**
 975 **with the new Rb–Sr single-spot ages obtained in this study. The onset of sedimentation in the Athabasca Basin occurred at ca. 1760–**

976 1720 Ma (Ramaekers et al., 2007; Jeanneret et al., 2016). The diagram synthesizes available ages documenting the prograde
977 metamorphic path, the retrograde evolution, and the late-orogenic cooling stages of the Trans-Hudson orogen, together with the timing
978 of hydrothermal events recorded both in the Athabasca Basin and in its crystalline basement. Literature ages are derived from multiple
979 minerals and chronometers. Included datasets comprise: U–Pb on zircon and monazite from (1) Annesley et al., 1992; (2) Annesley et
980 al., 1997; (3) Annesley et al., 1999; (4) Toma et al., 2024; (5) Jeanneret et al., 2016; (6) Card, 2012; (7) Card, 2014; (8) Card and Noll,
981 2016); Rb–Sr on biotite from (9) Worden et al., 1985; (10) Schneider et al., 2007); U–Pb on rutile from (11) Adlakha and Hattori, 2021);
982 Ar–Ar on muscovite from (12) Alexandre et al., 2009); K–Ar on muscovite from (13) Philippe et al., 1993); Re–Os on graphite from
983 (14) Toma et al., 2024); Ar–Ar on illite from (15) Alexandre et al., 2009); U–Pb on zircon from (16) Rainbird et al., 2007); U–Pb on
984 fluorapatite from (17) Davis et al., 2011); K–Ar on <2 µm fractions from gneiss from (18) Philippe et al., 1993); U–Pb on xenotime from
985 (19) Rabiei et al., 2017); U–Pb on anatase from (20) Adlakha and Hattori, 2021); U–Pb on UO₂ from (21) Alexandre et al., 2009; (22)
986 Alexandre et al., 2005; (23) Cumming and Krstić, 1992; (24) Fayek and Riciputi, 2002; (25) McGill et al., 1993; (26) Kister, 2003).
987 Probability density distribution and histogram plots of Rb–Sr single-spot ages obtained from preserved early hydrothermal and
988 metamorphic muscovite unaffected by post-crystallization alteration are correlated with recognized Trans-Hudson orogenic events.
989 Probability density distribution and histogram plots of Rb–Sr single-spot ages derived from muscovites overprinted by post-
990 crystallization illite-sudoite alteration are presented along with the results of a Gaussian Mixture Model (GMM) used to identify
991 distinct age components. The central age population at ca. 1640 Ma is interpreted to record the main illite-sudoite hydrothermal
992 alteration event, whereas subordinate components may correspond to additional hydrothermal pulses documented in the literature.

993 6. Conclusions

994 This study tests the relevance and limitations of the Rb–Sr chronometer applied to muscovite from pelitic gneisses,
995 including migmatites, and granitoids from the Paleoproterozoic basement of the Wollaston-Mudjatik Transition
996 Zone, within the context of hydrothermal alteration (formed by an association of illite and sudoite) associated with
997 the formation of Athabasca Basin unconformity-related uranium deposits. The primary objective was to determine
998 to what extent this isotope system, conventionally used to date the crystallization or cooling of crustal rocks, can
999 also record and quantify late-stage fluid circulation events, despite the complexity induced by partial system
1000 reopening through fluid-rock interaction.

1001 Petrographic and isotopic analyses of preserved domains demonstrate that, in areas lacking illite-sudoite alteration,
1002 metamorphic and early hydrothermal muscovite yield ages of ca. 1780 Ma and ca. 1750 Ma, respectively. Retro-
1003 metamorphic muscovite specifically records the transition to temperatures below its closure temperature (450–600
1004 °C), marking cooling, possibly in the presence of fluids, following the peak metamorphism and isothermal
1005 decompression of the THO basement. Early hydrothermal muscovite, in turn, records the exhumation and orogenic
1006 cooling phase of the THO, during which anatectic granitoids were emplaced and/or magmatic activity of the
1007 Kivalliq Igneous Suite occurred. Its formation is also consistent with the circulation of carbon-bearing aqueous
1008 fluids that facilitated the development of hydrothermal graphite. These results demonstrate that, in minimally
1009 altered domains, the Rb–Sr system yields ages consistent with established geochronological constraints obtained
1010 from independent isotope system and mineral phases for both episodes, thereby confirming that the Rb–Sr
1011 chronometer remains fully reliable for dating the terminal Paleoproterozoic thermo-metamorphic events.

1012 In contrast, muscovite from pelitic gneiss or granitic protoliths affected by illite-sudoite alteration developed after
1013 the deposition of the Athabasca Basin displays deeply modified mineralogical, geochemical, and isotopic
1014 signatures. These signatures reflect the micrometre-scale reopening of the Rb–Sr isotope system through fluid-
1015 rock interaction during brine circulation, in response to the structural destabilization of muscovite during
1016 illitization and/or sudoitization. The preferential transfer of radiogenic ⁸⁷Sr into clay phases and/or the fluid phase
1017 constitutes the major mechanism driving isotopic resetting.

1018 The dominant population of Rb–Sr single spot data at ca. 1640 Ma reflects a major hydrothermal event. This age
1019 interval coincides with a first-order sedimentary reorganization of the basin and with crustal-scale reactivation
1020 related to the late Paleoproterozoic Racklan-Mazatzal orogenic system (ca. 1660–1590 Ma), which affected the
1021 northwestern to southern margins of Laurentia and the adjacent edge of the Canadian Shield. These tectonic
1022 processes are accompanied by widespread fluid circulation and diagenetic to hydrothermal events in the Athabasca
1023 Basin, as independently documented by U–Pb ages obtained on fluorapatite. Comparison with other
1024 geochronological constraints and regional geodynamic reconstructions supports the interpretation that the ages
1025 measured on altered muscovite and associated alteration products are geologically meaningful and temporally
1026 consistent. Rather than reflecting localized or spurious resetting, these ages are best interpreted as recording a
1027 geologically realistic and regionally significant hydrothermal event, broadly coeval with the Racklan-Mazatzal
1028 orogenic continuum, which represents the northwestern expression of a circum-Laurentian orogenic belt affecting
1029 the margins of the Canadian Shield. It corresponds to the principal illite-sudoite alteration event responsible for
1030 the mineralized halos around uranium deposits and represents the key event recorded by altered muscovites.
1031 Additional age populations reflect further hydrothermal episodes or fluid-reactivation phases: (i) ca. 1680 Ma,
1032 possibly linked to a pre-ore argillization event documented by Ar–Ar ages on illite, or to an initial stage of partial
1033 disturbance of the Rb–Sr system; (ii) ca. 1600 Ma and ca. 1550 Ma, corresponding to a major oxidizing
1034 hydrothermal phase concomitant with a mineralizing event, recognized from U–Pb ages on anatase, xenotime, and
1035 uraninite, notably at McArthur River; (iii) ca. 1467 Ma, associated with a major mineralizing episode recorded in
1036 the district (Cigar Lake).

1037 This study demonstrates that the *in situ* Rb–Sr geochronometer applied to muscovite and related alteration products
1038 constitutes a relevant tool not only for constraining late-metamorphic and late-magmatic and/or early hydrothermal
1039 histories in unaltered domains, but also for identifying and dating post-crystallization hydrothermal circulation
1040 events after basin sedimentation, associated with unconformity-related metal deposits. By coupling detailed
1041 petrographic analysis with *in situ* geochemical characterization, it becomes possible to distinguish preserved ages
1042 reflecting Paleoproterozoic crystallization or cooling from reset ages marking Mesoproterozoic hydrothermal
1043 episodes. The Rb–Sr chronometer thus emerges as a powerful and complementary tool within the existing suite of
1044 fluid tracers, opening new perspectives for the temporal and spatial reconstruction of paleo-hydrothermal systems
1045 across basin-basement interfaces.

1046 **Code and data availability**

1047 All data supporting the findings of this study are provided in the Appendix.

1048 **Supplement**

1049 All supplementary material are provided in the Appendix.

1050 **Author contributions**

1051 Conceptualization: QB, JM; Fieldwork: QB, GM, EF, TO, AK, JM; Methodology and data acquisition: QB, CP,
1052 AL, JM; Data curation: QB, MS, TO, CP, AL, JM; Writing (original draft preparation): QB, GM, EF, CB, AL, PM,
1053 JM; Funding acquisition: JM.

1054 **Competing interests**

1055 The authors declare that they have no conflict of interest.

1056 **Disclaimer**

1057 Publisher's note: Copernicus Publications remains neutral with regard to jurisdictional claims made in the text,
1058 published maps, institutional affiliations, or any other geographical representation in this paper. While Copernicus
1059 Publications makes every effort to include appropriate place names, the final responsibility lies with the authors.

1060 **Acknowledgements**

1061 The French Agence Nationale de la Recherche (ANR) and Orano are thanked for funding this project. The authors
1062 gratefully acknowledge Orano Canada and Cameco for providing access to the field sites, samples, and data
1063 transfer. Special thanks are extended to Charles Khairallah, Magdalena Anderson, Andrew Kaczowka, and Gerard
1064 Zaluski for their valuable assistance during the field missions and data sharing. The authors would like to thank
1065 the editor Klaus Mezger, the associate editor Noah M. McLean, and two reviewers (Jarred Lloyd and one
1066 anonymous reviewer) for their constructive comments and suggestions, which greatly improved the quality of this
1067 manuscript.

1068 **Financial support**

1069 This research has been supported by the French Agence Nationale de la Recherche (ANR) and Orano, under grant
1070 ANR-21-CHIN-0006 (project GeomIn3D).

1071 **References**

1072 Adlakha, E. E., and Hattori, K.: Compositional variation and timing of aluminum phosphate-sulfate minerals in
1073 the basement rocks along the P2 fault and in association with the McArthur River uranium deposit, Athabasca
1074 Basin, Saskatchewan, Canada, *Am. Mineral.*, 100, 1386-1399, 10.2138/am-2015-5069, 2015.

1075 Adlakha, E., and Hattori, K.: Thermotectonic events recorded by U–Pb geochronology and Zr-in-rutile
1076 thermometry of Ti oxides in basement rocks along the P2 fault, eastern Athabasca Basin, Saskatchewan, Canada,
1077 *Geol. Soc. Am. Bull.*, 134, 567-576, 10.1130/B35820.1, 2021.

1078 Aldega, L., Viola, G., Casas-Sainz, A., Marcén, M., Román-Berdiel, T., and van der Lelij, R.: Unraveling Multiple
1079 Thermotectonic Events Accommodated by Crustal-Scale Faults in Northern Iberia, Spain: Insights From K–Ar
1080 Dating of Clay Gouges, *Tectonics*, 38, 3629-3651, <https://doi.org/10.1029/2019TC005585>, 2019.

1081 Alexandre, P., Kyser, K., Polito, P., and Thomas, D.: Alteration mineralogy and stable isotope geochemistry of
1082 Paleoproterozoic basement-hosted unconformity-type uranium deposits in the Athabasca Basin, Canada, *Econ.*
1083 *Geol.*, 100, 1547-1563, 10.2113/gsecongeo.100.8.15473, 2005.

1084 Alexandre, P. and Kyser, T. K.: GEOCHEMISTRY OF URANIFEROUS BITUMEN IN THE SOUTHWEST
1085 ATHABASCA BASIN, SASKATCHEWAN, CANADA, *Economic Geology*, 101, 1605-1612,
1086 <https://doi.org/10.2113/gsecongeo.101.8.1605>, 2006.

1087 Alexandre, P., Kyser, K., Thomas, D., Polito, P., and Marlat, J.: Geochronology of unconformity-related uranium
1088 deposits in the Athabasca Basin, Saskatchewan, Canada and their integration in the evolution of the basin, *Miner.*
1089 *Deposita*, 44, 41-59, [10.1007/s00126-007-0153-3](https://doi.org/10.1007/s00126-007-0153-3), 2009.

1090 Alexandre, P., Jiricka, D., and Witt, G.: Formation and evolution of the Centennial unconformity-related uranium
1091 deposit in the south-central Athabasca Basin, Canada, *Econ. Geol.*, 107, 385-400, [10.2113/econgeo.107.3.385](https://doi.org/10.2113/econgeo.107.3.385),
1092 2012.

1093 Anders, M. H., Laubach, S. E., and Scholz, C. H.: Microfractures: A review, *Journal of Structural Geology*, 69,
1094 377-394, <https://doi.org/10.1016/j.jsg.2014.05.011>, 2014.

1095 Ansdell, K. M.: Tectonic evolution of the Manitoba-Saskatchewan segment of the Paleoproterozoic Trans-Hudson
1096 Orogen, Canada, *Can. J. Earth Sci.*, 42, 741-759, <https://doi.org/10.1139/e05-035>, 2005.

1097 Annesley, I., Madore, C., and Krogh, T. E.: U–Pb zircon, titanite, and monazite ages from the Wollaston Domain:
1098 A summary, Summary of Investigations, Saskatchewan Geological Survey, Saskatchewan Energy and mines,
1099 Miscellaneous Report 92-4, p. 61-65, 1992.

1100 Annesley, I.R., and Madore, C.: A geological study of the Wollaston-Mudjatik domain boundary in the Wollaston
1101 Lake area, Hearne Province, Saskatchewan, Saskatchewan Research Council, Publ. R-1230-6-C-94, 162 p., 1994.

1102 Annesley, I.R., Madore, C., and Shi, R.: Thermotectonic evolution of the Wollaston EAGLE Project Area ,
1103 Saskatchewan Research Council, Publ. R-1420-2-C-97, Part 1, 1-62, 1997a.

1104 Annesley, I., Madore, C., Shi, R., and Krogh, T.: U–Pb geochronology of thermotectonic events in the Wollaston
1105 Lake area, Wollaston Domain: A summary of 1994-1996 results, Summary of Investigations 1997, Saskatchewan
1106 Geological Survey, Saskatchewan Energy and Mines, 1, 162-173, 1997b.

1107 Annesley, I.R., Madore, C., and Krogh, T.E.: U–Pb geochronology of peraluminous pegmatites from the Wollaston
1108 Lake area, northern Saskatchewan, *Geol. Assoc. Can.-Mineral. Assoc. Can. Annual Meeting, Program with*
1109 *Abstracts*, 22, A-4, 1997c.

1110 Annesley, I.R., Madore, C., Shi, R., and Krogh, T.E.: U–Pb geochronology and thermotectonic history of the
1111 Wollaston Domain in the Wollaston Lake area, Hearne Province, Saskatchewan, *Geol. Assoc. Can.-Mineral. Assoc.*
1112 *Can. Annual Meeting, Program with Abstracts*, 21, A-4, 1999a.

1113 Annesley, I.R., Madore, C., Krogh, T.E., Kwok, Y.Y., and Kamo, S.L.: New U–Pb zircon and
1114 monazite geochronological results for Archean and Paleoproterozoic basement to the southeastern part of the
1115 Athabasca Basin, Saskatchewan, Saskatchewan Geological Survey, Misc. Rep. 99-4.2, 90-99, 1999b.

1116 Annesley, I. R., Madore, C., and Portella, P.: Geology and thermotectonic evolution of the western margin of the
1117 Trans-Hudson Orogen: evidence from the eastern sub-Athabasca basement, Saskatchewan, *Can. J. Earth Sci.*, 42,
1118 573-597, <https://doi.org/10.1139/e05-034>, 2005.

1119 Beaufort, D., Patrier, P., Laverret, E., Bruneton, P., and Mondy, J.: Clay Alteration Associated with Proterozoic
1120 Unconformity-Type Uranium Deposits in the East Alligator Rivers Uranium Field, Northern Territory, Australia,
1121 *Economic Geology*, 100, 515-536, <https://doi.org/10.2113/gsecongeo.100.3.515>, 2005.

1122 Bevan, D., Coath, C. D., Lewis, J., Schwieters, J., Lloyd, N., Craig, G., Wehrs, H., and Elliott, T.: In situ Rb–Sr
1123 dating by collision cell, multicollection inductively-coupled plasma mass-spectrometry with pre-cell mass-filter,
1124 (CC-MC-ICPMS/MS), *J. Anal. At. Spectrom.*, 36, 917-931, <https://doi.org/10.1039/D1JA00006C>, 2021.

1125 Boiron, M.-C., Cathelineau, M., and Richard, A.: Fluid flows and metal deposition near basement /cover
1126 unconformity: lessons and analogies from Pb-Zn-F-Ba systems for the understanding of Proterozoic U deposits,
1127 *Geofluids*, 10, 270-292, <https://doi.org/10.1111/j.1468-8123.2010.00289.x>, 2010.

1128 Boschetti, L., Boullerne, C., Rolland, Y., Schwartz, S., Milesi, G., Bienvegnant, D., Macret, E., Charpentier, D.,
1129 Münch, P., Mercadier, J., Iemmolo, A., Lanari, P., Rossi, M., and Mouthereau, F.: Shear zone memory revealed by
1130 in-situ Rb–Sr and $^{40}\text{Ar}/^{39}\text{Ar}$ dating of Pyrenean and Alpine tectonic phases in the external Alps, *Lithos*, 514-515,
1131 108168, <https://doi.org/10.1016/j.lithos.2025.108168>, 2025.

1132 Bickford, M., Chiarenzelli, J., Van Schmus, W., Collerson, K. D., and Lewry, J.: Proterozoic collisional tectonism
1133 in the Trans-Hudson orogen, Saskatchewan, *Geology*, 18, 14-18, [https://doi.org/10.1130/0091-7613\(1990\)018](https://doi.org/10.1130/0091-7613(1990)018)
1134 [%253C0014:PCTITT%253E2.3.CO;2](https://doi.org/10.1130/0091-7613(1990)018%253C0014:PCTITT%253E2.3.CO;2), 1990.

1135 Bickford, M. E., Mock, T. D., Steinhart Iii, W. E., Collerson, K. D., and Lewry, J. F.: Origin of the Archean Sask
1136 craton and its extent within the Trans-Hudson orogen: evidence from Pb and Nd isotopic compositions of basement
1137 rocks and post-orogenic intrusions, *Can. J. Earth Sci.*, 42, 659-684, <https://doi.org/10.1139/e04-064>, 2005.

1138 Bishop, C. M. and Nasrabadi, N. M.: *Pattern recognition and machine learning*, Springer, 2006.

1139 Brigatti, M. F. and Guggenheim, S.: Mica Crystal Chemistry and the Influence of Pressure, Temperature, and Solid
1140 Solution on Atomistic Models, *Reviews in Mineralogy and Geochemistry*, 46, 1-97,
1141 <https://doi.org/10.2138/rmg.2002.46.01>, 2002.

1142 Brooks, C., Hart, S. R., Hofmann, A., and James, D. E.: Rb–Sr mantle isochrons from oceanic regions, *Earth and*
1143 *Planetary Science Letters*, 32, 51-61, [https://doi.org/10.1016/0012-821X\(76\)90184-9](https://doi.org/10.1016/0012-821X(76)90184-9), 1976.

1144 Bruneton, P.: Geological environment of the Cigar Lake uranium deposit, *Can. J. Earth Sci.*, 30, 653-673,
1145 <https://doi.org/10.1139/e93-054>, 1993.

1146 Campanha, G. A. C., Hueck, M., Wemmer, K., Esteves, M. C. B., Joncew, H. C., Faleiros, F. M., and Veloso, R. S.
1147 S.: Foreland deformation of Brasiliano orogens at the eastern and western margins of the São Francisco Craton:
1148 K–Ar illite dating of the Araçuaí and Brasília fold-and-thrust belts, *JGS*, 183, jgs2025-138,
1149 <https://doi.org/10.1144/jgs2025-138>, 2026.

1150 Card, C.: *The Origins of Anomalously Graphitic Rocks and Quartzite Ridges in the Basement to the Southeastern*
1151 *Athabasca Basin*, 2012.

1152 Card, C.: *Altered Pelitic Gneisses and Associated " Quartzite Ridges " Beneath the Southeastern Athabasca Basin:*
1153 *Alteration Facies and their Relationship to Uranium Deposits along the Wollaston-Mudjatik Transition*, 2014.

1154 Card, C. and Noll, J.: *Host-Rock Protoliths, Pre-Ore Metasomatic Mineral Assemblages and Textures, and Exotic*
1155 *Rocks in the Western Athabasca Basin: Ore-System Controls and Implications for the Unconformity- Related*
1156 *Uranium Model*, <https://doi.org/10.13140/RG.2.2.26473.70241>, 2016.

1157 Carl, C., Pechmann, E. V., Höhndorf, A., and Ruhmann, G.: Mineralogy and U/Pb, Pb/Pb, and Sm/Nd
1158 geochronology of the Key Lake uranium deposit, Athabasca Basin, Saskatchewan, Canada, *Can. J. Earth Sci.*, 29,
1159 879-895, <https://doi.org/10.1139/e92-075>, 1992.

1160 Cathelineau, M., Boiron, M.-C., Fourcade, S., Ruffet, G., Clauer, N., Belcourt, O., Coulibaly, Y., Banks, D. A., and
1161 Guillocheau, F.: A major Late Jurassic fluid event at the basin/basement unconformity in western France:
1162 ⁴⁰Ar/³⁹Ar and K–Ar dating, fluid chemistry, and related geodynamic context, *Chemical Geology*, 322-323, 99-
1163 120, <https://doi.org/10.1016/j.chemgeo.2012.06.008>, 2012.

1164 Chen, M., Chen, G., An, P., Zhang, L., and Wang, Y.: In situ illite Rb–Sr dating indicates the coevality of Carlin-
1165 type gold deposits inside and around the isolated carbonate platform in western Guangxi, China, *Ore Geology*
1166 *Reviews*, 165, 105905, <https://doi.org/10.1016/j.oregeorev.2024.105905>, 2024.

1167 Cherniak, D. J. and Watson, E. B.: Pb diffusion in zircon, *Chemical Geology*, 172, 5-24,
1168 [https://doi.org/10.1016/S0009-2541\(00\)00233-3](https://doi.org/10.1016/S0009-2541(00)00233-3), 2001.

1169 Cherniak, D. J., Watson, E. B., Grove, M., and Harrison, T. M.: Pb diffusion in monazite: a combined RBS/SIMS
1170 study, *Geochimica et Cosmochimica Acta*, 68, 829-840, <https://doi.org/10.1016/j.gca.2003.07.012>, 2004.

1171 Chi, G., Li, Z., Chu, H., Bethune, K. M., Quirt, D. H., Ledru, P., Normand, C., Card, C., Bosman, S., Davis, W. J.,
1172 and Potter, E. G.: A SHALLOW-BURIAL MINERALIZATION MODEL FOR THE UNCONFORMITY-
1173 RELATED URANIUM DEPOSITS IN THE ATHABASCA BASIN, *Economic Geology*, 113, 1209-1217,
1174 <https://doi.org/10.5382/econgeo.2018.4588>, 2018.

1175 Chiarenzelli, J.: Petrogenesis and tectonic significance of the Guncoat and Nistowiak gneisses, Glennie Lake
1176 Domain, northern Saskatchewan, Unpublished Ph. D. thesis, University of Kansas, 229, 1989.

1177 Chiarenzelli, J., Aspler, L., Villeneuve, M., and Lewry, J.: Early Proterozoic Evolution of the Saskatchewan Craton
1178 and Its Allochthonous Cover, Trans-Hudson Orogen, *The Journal of Geology*, 106, 247-268,
1179 <https://doi.org/10.1086/516020>, 1998.

1180 Clauer, N., Środoń, J., Francu, J., and Šucha, V.: K–Ar dating of illite fundamental particles separated from illite-
1181 smectite, *Clay Minerals*, 32, 181-196, <https://doi.org/10.1180/claymin.1997.032.2.02>, 1997.

1182 Clauer, N., Mercadier, J., Patrier, P., Laverret, E., and Bruneton, P.: Relating unconformity-type uranium
1183 mineralization of the Alligator Rivers Uranium Field (Northern Territory, Australia) to the regional Proterozoic
1184 tectono-thermal activity: An illite K–Ar dating approach, *Precambrian Research*, 269, 107-121,
1185 <https://doi.org/10.1016/j.precamres.2015.08.007>, 2015.

1186 Cloutier, J., Kyser, K., Olivo, G. R., Alexandre, P., and Halaburda, J.: The Millennium Uranium Deposit, Athabasca
1187 Basin, Saskatchewan, Canada: An Atypical Basement-Hosted Unconformity-Related Uranium Deposit, *Economic*
1188 *Geology*, 104, 815-840, <https://doi.org/10.2113/gsecongeo.104.6.815>, 2009.

1189 Cloutier, J., Kyser, K., Olivo, G. R., and Alexandre, P.: Contrasting Patterns of Alteration at the Wheeler River
1190 Area, Athabasca Basin, Saskatchewan, Canada: Insights into the Apparently Uranium-Barren Zone K Alteration
1191 System, *Economic Geology*, 105, 303-324, <https://doi.org/10.2113/gsecongeo.105.2.303>, 2010.

1192 Cloutier, J., Kyser, K., Olivo, G. R., and Brisbin, D.: Geochemical, isotopic, and geochronologic constraints on
1193 the formation of the Eagle Point basement-hosted uranium deposit, Athabasca Basin, Saskatchewan, Canada and
1194 recent remobilization of primary uraninite in secondary structures, *Miner Deposita*, 46, 35-56,
1195 <https://doi.org/10.1007/s00126-010-0308-5>, 2011.

1196 Corrigan, D.: Paleoproterozoic crustal evolution and tectonics processes: Insights from the LITHOPROBE
1197 program in the Trans-Hudson orogen, Canada, *Tectonic Styles in Canada: The LITHOPROBE Perspective*, 49,
1198 237-284, 2012.

1199 Corrigan, D., Hajnal, Z., Németh, B., and Lucas, S. B.: Tectonic framework of a Paleoproterozoic arc-continent to
1200 continent-continent collisional zone, Trans-Hudson Orogen, from geological and seismic reflection studies, *Can.*
1201 *J. Earth Sci.*, 42, 421-434, <https://doi.org/10.1139/e05-025>, 2005.

1202 Corrigan, D., Pehrsson, S., Wodicka, N., and De Kemp, E.: The Palaeoproterozoic Trans-Hudson Orogen: a
1203 prototype of modern accretionary processes, *SP*, 327, 457-479, <https://doi.org/10.1144/SP327.19>, 2009.

1204 Creaser, R. and Stasiuk, L. D.: Depositional age of the douglas formation, Northern Saskatchewan, determined by
1205 RE-Os geochronology, *Bulletin of the Geological Survey of Canada*, 341-346, 2007.

1206 Cumming, G. L. and Krstic, D.: The age of unconformity-related uranium mineralization in the Athabasca Basin,
1207 northern Saskatchewan, *Can. J. Earth Sci.*, 29, 1623-1639, <https://doi.org/10.1139/e92-128>, 1992.

1208 Cuney, M. and Kyser, K.: *Geology and geochemistry of uranium and thorium deposits*, Mineralogical Association
1209 of Canada, 2015.

1210 DePaolo, D. J.: Trace element and isotopic effects of combined wallrock assimilation and fractional crystallization,
1211 *Earth and Planetary Science Letters*, 53, 189-202, [https://doi.org/10.1016/0012-821X\(81\)90153-9](https://doi.org/10.1016/0012-821X(81)90153-9), 1981.

1212 Derome, D., Cathelineau, M., Cuney, M., Fabre, C., Lhomme, T., and Banks, D. A.: Mixing of Sodic and Calcic
1213 Brines and Uranium Deposition at McArthur River, Saskatchewan, Canada: A Raman and Laser-Induced
1214 Breakdown Spectroscopic Study of Fluid Inclusions, *Economic Geology*, 100, 1529-1545,
1215 <https://doi.org/10.2113/gsecongeo.100.8.1529>, 2005.

1216 Davis, W., Gall, Q., Jefferson, C. W., and Rainbird, R.: Fluorapatite in the Paleoproterozoic Thelon Basin:
1217 Structural-stratigraphic context, in situ ion microprobe U–Pb ages, and fluid-flow history, *Geological Society of*
1218 *America Bulletin*, 123, 1056-1073, <https://doi.org/10.1130/B30163.1>, 2011.

1219 Dickin, A. P.: *Radiogenic Isotope Geology*, 3rd ed., Cambridge University Press,
1220 <https://doi.org/10.1017/9781316163009>, 2018.

1221 Dodson, M. H.: Closure temperature in cooling geochronological and petrological systems, *Contr. Mineral. and*
1222 *Petrol.*, 40, 259-274, <https://doi.org/10.1007/BF00373790>, 1973.

1223 Drake, H., Tillberg, M., Reinhardt, M., Whitehouse, M. J., and Kooijman, E.: In Situ Rb/Sr Geochronology and
1224 Stable Isotope Geochemistry Evidence for Neoproterozoic and Paleozoic Fracture-Hosted Fluid Flow and
1225 Microbial Activity in Paleoproterozoic Basement, SW Sweden, *Geochem Geophys Geosyst*, 24, e2023GC010892,
1226 <https://doi.org/10.1029/2023GC010892>, 2023.

- 1227 Eberlei, T., Habler, G., Wegner, W., Schuster, R., Körner, W., Thöni, M., and Abart, R.: Rb/Sr isotopic and
1228 compositional retentivity of muscovite during deformation, *Lithos*, 227, 161-178,
1229 <https://doi.org/10.1016/j.lithos.2015.04.007>, 2015.
- 1230 Eisele, J. and Isachsen, C. E.: Crustal Growth in Southern Arizona: U–Pb Geochronologic and Sm–Nd Isotopic
1231 Evidence for Addition of the Paleoproterozoic Cochise Block to the Mazatzal Province, *American Journal of*
1232 *Science*, 301, 773-797, <https://doi.org/10.2475/ajs.301.9.773>, 2001.
- 1233 Etheridge, M. A., Wall, V. J., and Vernon, R. H.: The role of the fluid phase during regional metamorphism and
1234 deformation, *Journal Metamorphic Geology*, 1, 205-226, <https://doi.org/10.1111/j.1525-1314.1983.tb00272.x>,
1235 1983.
- 1236 Evans, J., MILLAR, I., and NOBLE, S.: Hydration during uplift is recorded by reset Rb–Sr whole-rock ages,
1237 *Journal of The Geological Society - J GEOL SOC*, 152, 209-212, <https://doi.org/10.1144/gsjgs.152.2.0209>, 1995.
- 1238 Faulkner, D. R., Jackson, C. A. L., Lunn, R. J., Schlische, R. W., Shipton, Z. K., Wibberley, C. A. J., and Withjack,
1239 M. O.: A review of recent developments concerning the structure, mechanics and fluid flow properties of fault
1240 zones, *Journal of Structural Geology*, 32, 1557-1575, <https://doi.org/10.1016/j.jsg.2010.06.009>, 2010.
- 1241 Faure, G., Mensing, T. M., and Faure, G.: *Isotopes: principles and applications*, Third edition., John Wiley & Sons,
1242 Inc, Hoboken, New Jersey, 897 pp., 2013.
- 1243 Fayek, M. and Kyser, T. K.: Characterization of multiple fluid-flow events and rare-earth-element mobility
1244 associated with formation of unconformity-type uranium deposits in the Athabasca Basin, Saskatchewan, *The*
1245 *Canadian Mineralogist*, 35, 627-658, 1997.
- 1246 Fayek, M., Harrison, T. M., Ewing, R. C., Grove, M., and Coath, C. D.: O and Pb isotopic analyses of uranium
1247 minerals by ion microprobe and U–Pb ages from the Cigar Lake deposit, *Chemical Geology*, 185, 205-225,
1248 [https://doi.org/10.1016/S0009-2541\(01\)00401-6](https://doi.org/10.1016/S0009-2541(01)00401-6), 2002.
- 1249 Fayek, M. and Riciputi, L.: U and Pb isotope analysis of uranium minerals by ion microprobe and the
1250 geochronology of McArthur River and Sue Zone uranium deposits, Saskatchewan, Canada, *Canadian*
1251 *Mineralogist*, 40, 1553-1569, <https://doi.org/10.2113/gscanmin.40.6.1553>, 2002.
- 1252 Fraley, C. and Raftery, A. E.: Model-Based Clustering, Discriminant Analysis, and Density Estimation, *Journal of*
1253 *the American Statistical Association*, 97, 611-631, <https://doi.org/10.1198/016214502760047131>, 2002.
- 1254 Frey, M., Bossennec, C., Seib, L., Bär, K., Schill, E., and Sass, I.: Interdisciplinary fracture network
1255 characterization in the crystalline basement: a case study from the Southern Odenwald, SW Germany, *Solid Earth*,
1256 13, 935-955, <https://doi.org/10.5194/se-13-935-2022>, 2022.
- 1257 Furlanetto, F., Thorkelson, D. J., Daniel Gibson, H., Marshall, D. D., Rainbird, R. H., Davis, W. J., Crowley, J. L.,
1258 and Vervoort, J. D.: Late Paleoproterozoic terrane accretion in northwestern Canada and the case for circum-
1259 Columbian orogenesis, *Precambrian Research*, 224, 512-528, <https://doi.org/10.1016/j.precamres.2012.10.010>,
1260 2013.

- 1261 Furlanetto, F., Thorkelson, D. J., Rainbird, R. H., Davis, W. J., Gibson, H. D., and Marshall, D. D.: The
1262 Paleoproterozoic Wernecke Supergroup of Yukon, Canada: Relationships to orogeny in northwestern Laurentia
1263 and basins in North America, East Australia, and China, *Gondwana Research*, 39, 14-40,
1264 <https://doi.org/10.1016/j.gr.2016.06.007>, 2016.
- 1265 Galbraith, R. F.: Graphical Display of Estimates Having Differing Standard Errors, *Technometrics*, 30, 271-281,
1266 <https://doi.org/10.2307/1270081>, 1988.
- 1267 Galbraith, R. F.: The radial plot: Graphical assessment of spread in ages, *International Journal of Radiation*
1268 *Applications and Instrumentation. Part D. Nuclear Tracks and Radiation Measurements*, 17, 207-214,
1269 [https://doi.org/10.1016/1359-0189\(90\)90036-W](https://doi.org/10.1016/1359-0189(90)90036-W), 1990.
- 1270 Gerardin, M., Milesi, G., Mercadier, J., Cathelineau, M., and Bartier, D.: Development of an integrated analytical
1271 platform for clay mineral separation, characterization and K–Ar dating, *Geoscientific Instrumentation, Methods*
1272 *and Data Systems*, 13, 309-323, <https://doi.org/10.5194/gi-13-309-2024>, 2024.
- 1273 Glodny, J. and Grauert*, B.: Evolution of a hydrothermal fluid-rock interaction system as recorded by Sr isotopes:
1274 A case study from the Schwarzwald, SW Germany, *Miner Petrol*, 95, 163-178, [https://doi.org/10.1007/s00710-](https://doi.org/10.1007/s00710-008-0034-1)
1275 [008-0034-1](https://doi.org/10.1007/s00710-008-0034-1), 2009.
- 1276 Glodek, M., Schels, M., and Schwenker, F.: Ensemble Gaussian mixture models for probability density estimation,
1277 *Comput Stat*, 28, 127-138, <https://doi.org/10.1007/s00180-012-0374-5>, 2013.
- 1278 Glorie, S., Gilbert, S. E., Hand, M., and Lloyd, J. C.: Calibration methods for laser ablation Rb–Sr geochronology:
1279 comparisons and recommendation based on NIST glass and natural reference materials, *Geochronology*, 6, 21–36,
1280 <https://doi.org/10.5194/gchron-6-21-2024>, 2024.
- 1281 Grand’Homme, A., Janots, E., Bosse, V., Seydoux-Guillaume, A. M., and De Ascensão Guedes, R.: Interpretation
1282 of U-Th-Pb in-situ ages of hydrothermal monazite-(Ce) and xenotime-(Y): evidence from a large-scale regional
1283 study in clefts from the western alps, *Miner Petrol*, 110, 787-807, <https://doi.org/10.1007/s00710-016-0451-5>,
1284 2016.
- 1285 Gyomlai, T., Agard, P., Herviou, C., Jolivet, L., Monié, P., Mendes, K., and Iemmolo, A.: In situ Rb–Sr and ⁴⁰Ar-
1286 ³⁹Ar dating of distinct mica generations in the exhumed subduction complex of the Western Alps, *Contrib Mineral*
1287 *Petrol*, 178, 58, <https://doi.org/10.1007/s00410-023-02042-8>, 2023.
- 1288 Halter, G.: Zonalite des alterations dans l’environnement des gisements d’uranium associes a la discordance du
1289 proterozoique moyen (saskatchewan, canada), These de doctorat, Université Louis Pasteur (Strasbourg) (1971-
1290 2008), 1988.
- 1291 Hastie, T., Friedman, J., and Tibshirani, R.: *The Elements of Statistical Learning*, Springer New York, New York,
1292 NY, <https://doi.org/10.1007/978-0-387-21606-5>, 2001.
- 1293 Hobson, G. D., Canada, G. S. of, and MacAulay, H. A.: A Seismic Reconnaissance Survey of the Athabasca
1294 Formation, Alberta and Saskatchewan (part of 74), Department of Energy, Mines and Resources, 36 pp., 1969.

- 1295 Hoeve, J. and Sibbald, T. I. I.: On the genesis of Rabbit Lake and other unconformity-type uranium deposits in
1296 northern Saskatchewan, Canada, *Economic Geology*, 73, 1450-1473,
1297 <https://doi.org/10.2113/gsecongeo.73.8.1450>, 1978.
- 1298 Hogmalm, K. J., Zack, T., Karlsson, A. K.-O., Sjöqvist, A. S. L., and Garbe-Schönberg, D.: In situ Rb–Sr and K-
1299 Ca dating by LA-ICP-MS/MS: an evaluation of N₂O and SF₆ as reaction gases, *J. Anal. At. Spectrom.*, 32, 305-
1300 313, <https://doi.org/10.1039/C6JA00362A>, 2017.
- 1301 Holness, M.: PARNELL, J. (ed.) 1998. Dating and Duration of Fluid Flow and Fluid-Rock Interaction. Geological
1302 Society Special Publication no. 144. vi+284 pp. Price £69.00, US \$115.00 (hard covers); members' price £35.00,
1303 US \$58.00. ISBN 1 86239 019 3. -, *Geological Magazine*, 137, 705-712,
1304 <https://doi.org/10.1017/S0016756800274736>, 2000.
- 1305 Huang, C., Wang, H., Xie, L., Xu, L., Wu, S., Yang, Y., and Yang, J.: High-precision Rb–Sr isotope analysis with
1306 Neoma MS/MS: Enhancing in situ geochronology by laser ablation, *Spectrochimica Acta Part B: Atomic*
1307 *Spectroscopy*, 224, 107117, <https://doi.org/10.1016/j.sab.2025.107117>, 2025.
- 1308 Huang, Y., Qi, X., Wu, Q., Li, J., Ren, M., Duan, L., Xiong, T., Yang, Z., Zhao, Y., Ciren, L., Wei, W., Duan, J.,
1309 and Yan, M.: In Situ Rb-Sr Dates of Muscovite and Sulfur Isotope of Pyrite from the Yangshan Gold Deposit in
1310 Western Qinling, China, *Acta Geologica Sinica (Eng)*, 97, 1475-1489, <https://doi.org/10.1111/1755-6724.15091>,
1311 2023.
- 1312 Hueck, M., Wemmer, K., Ksienzyk, A. K., Kuehn, R., and Vogel, N.: Potential, premises, and pitfalls of interpreting
1313 illite argon dates - A case study from the German Variscides, *Earth-Science Reviews*, 232, 104133,
1314 <https://doi.org/10.1016/j.earscirev.2022.104133>, 2022.
- 1315 Jeanneret, P., Goncalves, P., Durand, C., Trap, P., Marquer, D., Quirt, D., and Ledru, P.: Tectono-metamorphic
1316 evolution of the pre-Athabasca basement within the Wollaston–Mudjatik Transition Zone, Saskatchewan, *Can. J.*
1317 *Earth Sci.*, 53, 231–259, <https://doi.org/10.1139/cjes-2015-0136>, 2016.
- 1318 Jeanneret, P., Goncalves, P., Durand, C., Poujol, M., Trap, P., Marquer, D., Quirt, D., and Ledru, P.:
1319 Geochronological constraints on the trans-Hudsonian tectono-metamorphic evolution of the pre-Athabasca
1320 basement within the Wollaston-Mudjatik Transition Zone, Saskatchewan, *Precambrian Research*, 301, 152-178,
1321 <https://doi.org/10.1016/j.precamres.2017.07.019>, 2017.
- 1322 Jefferson, C. W., Thomas, D. J., Gandhi, S. S., Ramaekers, P., Delaney, G., Brisbin, D., Cutts, C., Portella, P., and
1323 Olson, R. A.: Unconformity-associated uranium deposits of the Athabasca Basin, Saskatchewan and Alberta,
1324 <https://doi.org/10.4095/223744>, 2007.
- 1325 Jegal, Y., Zimmermann, C., Reisberg, L., Yeghicheyan, D., Cloquet, C., Peiffert, C., Gerardin, M., Deloule, E., and
1326 Mercadier, J.: Characterisation of Reference Materials for In Situ Rb-Sr Dating by LA-ICP-MS / MS, *Geostandard*
1327 *Geoanalytic Res*, 46, 645-671, <https://doi.org/10.1111/ggr.12456>, 2022.
- 1328 Jenkin, G. R. T., Ellam, R. M., Rogers, G., and Stuart, F. M.: An investigation of closure temperature of the biotite
1329 Rb–Sr system: The importance of cation exchange, *Geochimica et Cosmochimica Acta*, 65, 1141-1160,
1330 [https://doi.org/10.1016/S0016-7037\(00\)00560-3](https://doi.org/10.1016/S0016-7037(00)00560-3), 2001.

- 1331 Juhász, A., Tóth, T. M., Ramseyer, K., and Matter, A.: Connected fluid evolution in fractured crystalline basement
1332 and overlying sediments, Pannonian Basin, SE Hungary, *Chemical Geology*, 182, 91-120,
1333 [https://doi.org/10.1016/S0009-2541\(01\)00269-8](https://doi.org/10.1016/S0009-2541(01)00269-8), 2002.
- 1334 Kaczowka, A. J., Kyser, T. K., Kotzer, T. G., Leybourne, M. I., and Layton-Matthews, D.: Geometallurgical ore
1335 characterization of the high-grade polymetallic unconformity-related uranium deposit, *The Canadian Mineralogist*,
1336 59, 813-845, <https://doi.org/10.3749/canmin.2000050>, 2021.
- 1337 Kalt, A., Grauert, B., and Baumann, A.: Rb-Sr and U-Pb isotope studies on migmatites from the Schwarzwald
1338 (Germany): constraints on isotopic resetting during Variscan high-temperature metamorphism, *Journal*
1339 *Metamorphic Geology*, 12, 667-680, <https://doi.org/10.1111/j.1525-1314.1994.tb00050.x>, 1994.
- 1340 Karlstrom, K. E. and Bowring, S. A.: Early Proterozoic Assembly of Tectonostratigraphic Terranes in
1341 Southwestern North America, *J. Geol.*, 96, 561-576, 1988.
- 1342 Kister, P.: Mobilité des éléments géochimiques dans un bassin sédimentaire clastique, du Protérozoïque à nos
1343 jours : le bassin Athabasca (Saskatchewan, Canada), phdthesis, Institut National Polytechnique de Lorraine, 2003.
- 1344 Kister, P., Vieillard, P., Cuney, M., Quirr, D., and Laverret, E.: Thermodynamic constraints on the mineralogical
1345 and fluid composition evolution in a clastic sedimentary basin: the Athabasca Basin (Saskatchewan, Canada), *ejm*,
1346 17, 325-341, <https://doi.org/10.1127/0935-1221/2005/0017-0325>, 2005.
- 1347 Kohn, M.: Titanite Petrochronology, *Reviews in Mineralogy and Geochemistry*, 2017.
- 1348 Kotzer, T. G. and Kyser, T. K.: Fluid history of the Athabasca Basin and its relation to uranium deposits.
1349 Saskatchewan Energy and Mines, Saskatchewan Geological Survey Miscellaneous Report, 90, 153-157, 1990.
- 1350 Kotzer, T. G. and Kyser, T. K.: Petrogenesis of the Proterozoic Athabasca Basin, northern Saskatchewan, Canada,
1351 and its relation to diagenesis, hydrothermal uranium mineralization and paleohydrogeology, *Chemical Geology*,
1352 120, 45-89, [https://doi.org/10.1016/0009-2541\(94\)00114-N](https://doi.org/10.1016/0009-2541(94)00114-N), 1995.
- 1353 Kyser, K., Hiatt, E., Renac, C., Durocher, K., Holk, G., and Deckart, K.: Diagenetic fluids in Paleo-and Meso-
1354 Proterozoic sedimentary basins and their implications for long protracted fluid histories, *Mineralogical Association*
1355 *of Canada Short Course*, 28, 225-262, 2000.
- 1356 Kyser, K., Lahusen, L., Drever, G., Dunn, C., Leduc, E., and Chipley, D.: Using Pb isotopes in surface media to
1357 distinguish anthropogenic sources from undercover uranium sources, *Comptes Rendus. Géoscience*, 347, 215-226,
1358 2015.
- 1359 Larsen, R. T. and Sundvoll: Rb-Sr isotope systematics In the magmatic rocks of the Oslo Rift, 2008.
- 1360 Liebmann, J., Kirkland, C. L., Kelsey, D. E., Korhonen, F. J., and Rankenburg, K.: Lithological fabric as a proxy
1361 for Rb-Sr isotopic complexity, *Chemical Geology*, 608, 121041, <https://doi.org/10.1016/j.chemgeo.2022.121041>,
1362 2022.

- 1363 Liu, W., Zhang, X., Zhang, J., and Jiang, M.: Sphalerite Rb–Sr Dating and in situ Sulfur Isotope Analysis of the
1364 Daliangzi Lead-Zinc Deposit in Sichuan Province, SW China, *J. Earth Sci.*, 29, 573-586,
1365 <https://doi.org/10.1007/s12583-018-0785-5>, 2018.
- 1366 Macdonald, C. C.: Mineralogy and geochemistry of a precambrian regolith in the Athabasca Basin, 1980.
- 1367 Mao, G., Hua, R., Long, G., and Lu, H.: Rb-Sr Dating of Pyrite and Quartz Fluid Inclusions and Origin of Ore-
1368 forming Materials of the Jinshan Gold Deposit, Northeast Jiangxi Province, South China, *Acta Geologica Sinica*
1369 (Eng), 87, 1658-1667, <https://doi.org/10.1111/1755-6724.12166>, 2013.
- 1370 McLachlan, G. and Peel, D.: *Finite Mixture Models*, 1st ed., Wiley, <https://doi.org/10.1002/0471721182>, 2000.
- 1371 Martz, P.: Caractéristiques, chronologie et rôles des circulations fluides dans le bassin d’Athabasca et son socle :
1372 implications dans la formation et l’évolution du gisement d’uranium de Cigar Lake, These de doctorat, Université
1373 de Lorraine, 2017.
- 1374 Martz, P., Mercadier, J., Cathelineau, M., Boiron, M.-C., Quirt, D., Doney, A., Gerbeaud, O., De Wally, E., and
1375 Ledru, P.: Formation of U-rich mineralizing fluids through basinal brine migration within basement-hosted shear
1376 zones: A large-scale study of the fluid chemistry around the unconformity-related Cigar Lake U deposit
1377 (Saskatchewan, Canada), *Chemical Geology*, 508, 116-143, <https://doi.org/10.1016/j.chemgeo.2018.05.042>,
1378 2019a.
- 1379 Martz, P., Mercadier, J., Perret, J., Villeneuve, J., Deloule, E., Cathelineau, M., Quirt, D., Doney, A., and Ledru,
1380 P.: Post-crystallization alteration of natural uraninites: Implications for dating, tracing, and nuclear forensics,
1381 *Geochimica et Cosmochimica Acta*, 249, 138-159, <https://doi.org/10.1016/j.gca.2019.01.025>, 2019b.
- 1382 Matheney, R. K., Brookins, D. G., Wallin, E. T., Shafiqullah, M., and Damon, P. E.: Incompletely reset Rb • Sr
1383 systems from a Cambrian red-rock granophyre terrane, Florida Mountains, New Mexico, U.S.A., *Chemical*
1384 *Geology: Isotope Geoscience section*, 86, 29-47, [https://doi.org/10.1016/0168-9622\(90\)90004-V](https://doi.org/10.1016/0168-9622(90)90004-V), 1990.
- 1385 Melnykov, V. and Melnykov, I.: Initializing the EM algorithm in Gaussian mixture models with an unknown
1386 number of components, *Computational Statistics & Data Analysis*, 56, 1381-1395,
1387 <https://doi.org/10.1016/j.csda.2011.11.002>, 2012.
- 1388 Mcfarlane, C. and Markharrison, T.: Pb-diffusion in monazite: Constraints from a high-T contact aureole setting,
1389 *Earth and Planetary Science Letters*, 250, 376–384, <https://doi.org/10.1016/j.epsl.2006.06.050>, 2006.
- 1390 McGill, B. D., Marlat, J. L., Matthews, R. B., Sopuck, V. J., Homeniuk, L. A., and Hubregtse, J. J.: The P2 North
1391 uranium deposit, Saskatchewan, Canada, *Explor. Min. Geol.*, 2, 321–331, 1993.
- 1392 McLachlan, G. J., Lee, S. X., and Rathnayake, S. I.: *Finite Mixture Models*, *Annual Review of Statistics and Its*
1393 *Application*, 6, 355-378, <https://doi.org/10.1146/annurev-statistics-031017-100325>, 2019.
- 1394 Menier, A., Roy, R., Harrison, G., Zerff, R. W., and Kinar, D.: Relationship between rock physical properties and
1395 spectral mineralogy applied to exploration for an unconformity-related uranium deposit (Saskatchewan, Canada),
1396 *Can. J. Earth Sci.*, 57, 1349-1364, <https://doi.org/10.1139/cjes-2019-0080>, 2020.

1397 Mercadier, J., Cuney, M., Cathelineau, M., and Lacorde, M.: U redox fronts and kaolinisation in basement-hosted
1398 unconformity-related U ores of the Athabasca Basin (Canada): late U remobilisation by meteoric fluids, *Miner*
1399 *Deposita*, 46, 105-135, <https://doi.org/10.1007/s00126-010-0314-7>, 2011.

1400 Mercadier, J., Richard, A., and Cathelineau, M.: Boron- and magnesium-rich marine brines at the origin of giant
1401 unconformity-related uranium deposits: $\delta^{11}\text{B}$ evidence from Mg-tourmalines, *Geology*, 40, 231-234,
1402 <https://doi.org/10.1130/G32509.1>, 2012.

1403 Młynarska, M., Barnes, C. J., Zack, T., Majka, J., and Mazur, S.: In situ white mica Rb/Sr geochronology of the
1404 Leszczyńiec metaigneous complex, West Sudetes: evidence of upper plate deformation at the onset of Variscan
1405 collision, *Int J Earth Sci (Geol Rundsch)*, 113, 319-333, <https://doi.org/10.1007/s00531-023-02373-8>, 2024.

1406 Muñoz-Montecinos, J., Giuliani, A., Oesch, S., Volante, S., Peters, B., and Behr, W.: In situ rubidium-strontium
1407 geochronology of white mica in young metamafic and metasomatic rocks from Syros: testing the limits of laser-
1408 ablation triple-quadrupole inductively coupled plasma mass spectrometer mica dating using different anchoring
1409 approaches, *Geochronology*, 6, 585-605, <https://doi.org/10.5194/gchron-6-585-2024>, 2024.

1410 Ng, R., Alexandre, P., Kyser, K., Cloutier, J., Abdu, Y. A., and Hawthorne, F. C.: Oxidation state of iron in alteration
1411 minerals associated with sandstone-hosted unconformity-related uranium deposits and apparently barren alteration
1412 systems in the Athabasca Basin, Canada: Implications for exploration, *Journal of Geochemical Exploration*, 130,
1413 22-43, <https://doi.org/10.1016/j.gexplo.2013.02.009>, 2013.

1414 Nguyen, H. and Mclachlan, G.: Maximum likelihood estimation of Gaussian mixture models without matrix
1415 operations, *Advances in Data Analysis and Classification*, 9, <https://doi.org/10.1007/s11634-015-0209-7>, 2015.

1416 Obin, T.: Mobilités du carbone et du soufre dans l'environnement du Bassin de l'Athabasca (Saskatchewan,
1417 Canada) et impact(s) sur la formation des gisements d'uranium de type discordance, *These de doctorat, Université*
1418 *de Lorraine*, 2025.

1419 Olierook, H. K. H., Rankenburg, K., Ulrich, S., Kirkland, C. L., Evans, N. J., Brown, S., McInnes, B. I. A., Prent,
1420 A., Gillespie, J., McDonald, B., and Darragh, M.: Resolving multiple geological events using in situ Rb–Sr
1421 geochronology: implications for metallogenesis at Tropicana, Western Australia, *Geochronology*, 2, 283-303,
1422 <https://doi.org/10.5194/gchron-2-283-2020>, 2020.

1423 Oummouch, A., Essaifi, A., Zayane, R., Maddi, O., Zouhair, M., and Maacha, L.: Geology and Metallogenesis of
1424 the Sediment-Hosted Cu-Ag Deposit of Tizert (Igherm Inlier, Anti-Atlas Copperbelt, Morocco), *Geofluids*, 2017,
1425 7508484, <https://doi.org/10.1155/2017/7508484>, 2017.

1426 Pacquet, A. and Weber, F.: Pétrographie et minéralogie des halos d'altération autour du gisement de Cigar Lake et
1427 leurs relations avec les minéralisations, *Can. J. Earth Sci.*, 30, 674-688, <https://doi.org/10.1139/e93-055>, 1993.

1428 Pagel, M.: Cadre géologique des gisements d'uranium dans la structure de Carswell (Saskatchewan, Canada).
1429 Etudes des phases fluides, Thèse de 3ème cycle, Université de Nancy, Nancy, France, 1975a.

1430 Pagel, M.: Détermination des conditions physico-chimiques de la silicification diagénétique des grès Athabasca
1431 (Canada) au moyen des inclusions fluides, *Comptes Rendus Académie Sci. Paris, Série D*, 280, 2301–2304, 1975b.

1432 Paton, C., Hellstrom, J., Paul, B., Woodhead, J., and Hergt, J.: Iolite: Freeware for the visualisation and processing
1433 of mass spectrometric data, *J. Anal. At. Spectrom.*, 26, 2508-2518, <https://doi.org/10.1039/C1JA10172B>, 2011.

1434 Pehrsson, S., Eglinton, B., Rainbird, R., Regis, D., Ramaekers, P., and Jefferson, C.: Extent and significance of
1435 the Racklan-Forward Orogen in Canada: far-field interior reactivation during Nuna assembly, *SP*, 531, 47-75,
1436 <https://doi.org/10.1144/SP531-2022-307>, 2023.

1437 Percival, J. B. and Kodama, H.: Sudoite from cigar lake, Saskatchewan, *The Canadian Mineralogist*, 27, 633-641,
1438 1989.

1439 Philippe, S., Lancelot, J. R., Clauer, N., and Pacquet, A.: Formation and evolution of the Cigar Lake uranium
1440 deposit based on U–Pb and K–Ar isotope systematics, *Can. J. Earth Sci.*, 30, 720-730, <https://doi.org/10.1139/e93-058>, 1993.

1442 Powell, J. W., Percival, J. B., Potter, E. G., Van Der Lelij, R., and Xie, R.: Mineralogy and K–Ar geochronology
1443 of clay alteration associated with uranium mineralization in the Patterson Lake Corridor, Saskatchewan, *GEEA*,
1444 22, geochem2021-061, <https://doi.org/10.1144/geochem2021-061>, 2022.

1445 Qiu, E., Larson, K. P., Camacho, A., and Zhang, Y.: Reassessing the timing of high-strain deformation in the
1446 Strangways Metamorphic Complex, Central Australia, by in situ mica Rb–Sr and titanite U–Pb geochronology,
1447 *JGS*, 181, jgs2023-163, <https://doi.org/10.1144/jgs2023-163>, 2024.

1448 Rabiei, M., Chi, G., Normand, C., Davis, W. J., Fayek, M., and Blamey, N. J. F.: Hydrothermal Rare Earth Element
1449 (Xenotime) Mineralization at Maw Zone, Athabasca Basin, Canada, and Its Relationship to Unconformity-Related
1450 Uranium Deposits, *Economic Geology*, 112, 1483-1507, <https://doi.org/10.5382/econgeo.2017.4518>, 2017.

1451 Rainbird, R. H., Stern, R. A., Rayner, N., Jefferson, C. W., and Delaney, G.: Age, provenance, and regional
1452 correlation of the Athabasca Group, Saskatchewan and Alberta, constrained by igneous and detrital zircon
1453 geochronology, *Bulletin-Geological Survey of Canada*, 588, 193, 2007.

1454 Ramaekers, P., Jefferson, C. W., Yeo, G. M., Collier, B., Long, D. G. F., Drever, G., McHardy, S., Jiricka, D., Cutts,
1455 C., and Wheatley, K.: Revised geological map and stratigraphy of the Athabasca Group, Saskatchewan and Alberta,
1456 *Bulletin-Geological Survey of Canada*, 588, 155, 2007.

1457 Rasmussen, B., Fletcher, I. R., and McNaughton, N. J.: Dating low-grade metamorphic events by SHRIMP U–Pb
1458 analysis of monazite in shales, *Geol*, 29, 963, [https://doi.org/10.1130/0091-7613\(2001\)029%253C0963:DLGMEB%253E2.0.CO;2](https://doi.org/10.1130/0091-7613(2001)029%253C0963:DLGMEB%253E2.0.CO;2), 2001.

1460 Rasmussen, B., Sheppard, S., and Fletcher, I. R.: Testing ore deposit models using in situ U–Pb geochronology of
1461 hydrothermal monazite: Paleoproterozoic gold mineralization in northern Australia, *Geology*, 34, 77-80,
1462 <https://doi.org/10.1130/G22058.1>, 2006.

1463 Rasmussen, B., Zi, J.-W., and Muhling, J. R.: Tectonic fluid expulsion: U–Pb evidence for punctuated
1464 hydrothermal fluid flow and hydraulic fracturing during orogenesis, *Earth and Planetary Science Letters*, 604,
1465 117997, <https://doi.org/10.1016/j.epsl.2023.117997>, 2023.

1466 Redaa, A., Farkaš, J., Gilbert, S., Collins, A. S., Wade, B., Löhr, S., Zack, T., and Garbe-Schönberg, D.: Assessment
1467 of elemental fractionation and matrix effects during in situ Rb–Sr dating of phlogopite by LA-ICP-MS/MS:
1468 implications for the accuracy and precision of mineral ages, *J. Anal. At. Spectrom.*, 36, 322-344,
1469 <https://doi.org/10.1039/D0JA00299B>, 2021.

1470 Redaa, A., Farkaš, J., Hassan, A., Collins, A. S., Gilbert, S., and Löhr, S. C.: Constraints from in-situ Rb–Sr dating
1471 on the timing of tectono-thermal events in the Umm Farwah shear zone and associated Cu-Au mineralisation in
1472 the Southern Arabian Shield, Saudi Arabia, *Journal of Asian Earth Sciences*, 224, 105037,
1473 <https://doi.org/10.1016/j.jseaes.2021.105037>, 2022.

1474 Reynolds, R. C. and Thomson, C. H.: Illite from the Potsdam Sandstone of New York: A Probable
1475 Noncentrosymmetric Mica Structure, *Clays and clay miner.*, 41, 66-72,
1476 <https://doi.org/10.1346/CCMN.1993.0410107>, 1993.

1477 Ribeiro, B. V., Kirkland, C. L., Finch, M. A., Faleiros, F. M., Reddy, S. M., Rickard, W. D. A., and Hartnady, M.
1478 I. H.: Microstructures, geochemistry, and geochronology of mica fish: Review and advances, *Journal of Structural*
1479 *Geology*, 175, 104947, <https://doi.org/10.1016/j.jsg.2023.104947>, 2023a.

1480 Ribeiro, B. V., Kirkland, C. L., Kelsey, D. E., Reddy, S. M., Hartnady, M. I. H., Faleiros, F. M., Rankenburg, K.,
1481 Liebmann, J., Korhonen, F. J., and Clark, C.: Time-strain evolution of shear zones from petrographically
1482 constrained Rb–Sr muscovite analysis, *Earth and Planetary Science Letters*, 602, 117969,
1483 <https://doi.org/10.1016/j.epsl.2022.117969>, 2023b.

1484 Richard, A., Banks, D. A., Mercadier, J., Boiron, M.-C., Cuney, M., and Cathelineau, M.: An evaporated seawater
1485 origin for the ore-forming brines in unconformity-related uranium deposits (Athabasca Basin, Canada): Cl/Br and
1486 $\delta^{37}\text{Cl}$ analysis of fluid inclusions, *Geochimica et Cosmochimica Acta*, 75, 2792-2810,
1487 <https://doi.org/10.1016/j.gca.2011.02.026>, 2011.

1488 Richard, A., Cauzid, J., Cathelineau, M., Boiron, M. -C., Mercadier, J., and Cuney, M.: Synchrotron XRF and
1489 XANES investigation of uranium speciation and element distribution in fluid inclusions from unconformity-related
1490 uranium deposits, *Geofluids*, 13, 101-111, <https://doi.org/10.1111/gfl.12009>, 2013.

1491 Richard, A., Montel, J.-M., Leborgne, R., Peiffert, C., Cuney, M., and Cathelineau, M.: Monazite Alteration in
1492 $\text{H}_2\text{O} \pm \text{HCl} \pm \text{NaCl} \pm \text{CaCl}_2$ Fluids at 150 °C and psat: Implications for Uranium Deposits, *Minerals*, 5, 693-706,
1493 <https://doi.org/10.3390/min5040518>, 2015.

1494 Rösel, D. and Zack, T.: LA-ICP-MS/MS Single-Spot Rb-Sr Dating, *Geostandard Geoanalytic Res*, 46, 143-168,
1495 <https://doi.org/10.1111/ggr.12414>, 2022.

1496 Saito, T., Qiu, H.-N., Shibuya, T., Li, Y.-B., Kitajima, K., Yamamoto, S., Ueda, H., Komiya, T., and Maruyama,
1497 S.: Ar–Ar dating for hydrothermal quartz from the 2.4 Ga Ongeluk Formation, South Africa: implications for
1498 seafloor hydrothermal circulation, *R Soc Open Sci*, 5, 180260, <https://doi.org/10.1098/rsos.180260>, 2018.

1499 Schneider, D. A., Heizler, M. T., Bickford, M. E., Wortman, G. L., Condie, K. C., and Perilli, S.: Timing constraints
1500 of orogeny to cratonization: Thermochronology of the Paleoproterozoic Trans-Hudson orogen, Manitoba and

1501 Saskatchewan, Canada, *Precambrian Research*, 153, 65-95, <https://doi.org/10.1016/j.precamres.2006.11.007>,
1502 2007.

1503 Scott Anderson, F., Levine, J., and Whitaker, T. J.: Rb–Sr resonance ionization geochronology of the Duluth
1504 Gabbro: A proof of concept for in situ dating on the Moon, *Rapid Communications in Mass Spectrometry*, 29,
1505 1457-1464, <https://doi.org/10.1002/rcm.7253>, 2015.

1506 Şengün, F., Bertrandsson Erlandsson, V., Hogmalm, J., and Zack, T.: In situ Rb–Sr dating of K-bearing minerals
1507 from the orogenic Akçaabat gold deposit in the Menderes Massif, Western Anatolia, Turkey, *Journal of Asian Earth*
1508 *Sciences*, 185, 104048, <https://doi.org/10.1016/j.jseaes.2019.104048>, 2019.

1509 Schmitz, B., Biermanns, P., Hueck, M., Wemmer, K., Schmid, S. M., Onuzi, K., Reicherter, K., and Ustaszewski,
1510 K.: Kinematics and Age of the Orogen-Perpendicular Shkoder-Peja Normal Fault in North Albania Constrained
1511 by Fault-Slip Data, Raman Spectroscopy and K–Ar Fault-Gouge Dating, *Tectonics*, 44, e2024TC008660,
1512 <https://doi.org/10.1029/2024TC008660>, 2025.

1513 Skirrow, R. G., Mercadier, J., Armstrong, R., Kuske, T., and Deloule, E.: The Ranger uranium deposit, northern
1514 Australia: Timing constraints, regional and ore-related alteration, and genetic implications for unconformity-
1515 related mineralisation, *Ore Geology Reviews*, 76, 463-503, <https://doi.org/10.1016/j.oregeorev.2015.09.001>, 2016.

1516 Sibson, R. H.: Conditions for fault-valve behaviour, *SP*, 54, 15-28,
1517 <https://doi.org/10.1144/GSL.SP.1990.054.01.02>, 1990.

1518 Sims, P. K. and Peterman, Z. E.: Early Proterozoic Central Plains orogen: A major buried structure in the north-
1519 central United States, *Geology*, 14, 488-491, [https://doi.org/10.1130/0091-7613\(1986\)14%253C488:EPCPOA%253E2.0.CO;2](https://doi.org/10.1130/0091-7613(1986)14%253C488:EPCPOA%253E2.0.CO;2), 1986.

1521 Skipton, D. R., St-Onge, M. R., Schneider, D. A., and McFarlane, C. R. M.: Tectonothermal Evolution of the
1522 Middle Crust in the Trans-Hudson Orogen, Baffin Island, Canada: Evidence from Petrology and Monazite
1523 Geochronology of Sillimanite-bearing Migmatites, *Journal of Petrology*, 57, 1437-1462,
1524 <https://doi.org/10.1093/petrology/egw046>, 2016.

1525 Tian, J., Wang, J., Tian, T., Wang, L., Wang, Y., Yu, X., Zhang, W., Ren, T., and Sun, B.: In-Situ Geochemical and
1526 Rb–Sr Dating Analysis of Sulfides from a Gold Deposit Offshore of Northern Sanshandao, Jiaodong Peninsula,
1527 North China: Implications for Gold Mineralization, *Minerals*, 14, 456, <https://doi.org/10.3390/min14050456>,
1528 2024.

1529 Tichomirowa, M., Käßner, A., Sperner, B., Lapp, M., Leonhardt, D., Linnemann, U., Münker, C., Ovtcharova, M.,
1530 Pfänder, J. A., Schaltegger, U., Sergeev, S., von Quadt, A., and Whitehouse, M.: Dating multiply overprinted
1531 granites: The effect of protracted magmatism and fluid flow on dating systems (zircon U–Pb: SHRIMP/SIMS, LA-
1532 ICP-MS, CA-ID-TIMS; and Rb–Sr, Ar–Ar) - Granites from the Western Erzgebirge (Bohemian Massif, Germany),
1533 *Chemical Geology*, 519, 11-38, <https://doi.org/10.1016/j.chemgeo.2019.04.024>, 2019.

1534 Tran, H., Ansdell, K., Bethune, K., Ashton, K., and Hamilton, M.: Provenance and tectonic setting of
1535 Paleoproterozoic metasedimentary rocks along the eastern margin of Hearne craton: Constraints from SHRIMP

1536 geochronology, Wollaston Group, Saskatchewan, Canada, *Precambrian Research*, 167, 171-185,
1537 <https://doi.org/10.1016/j.precamres.2008.08.003>, 2008.

1538 Toma, J., Creaser, R. A., Card, C., Stern, R. A., Chacko, T., and Steele-MacInnis, M.: Re-Os systematics and
1539 chronology of graphite, *Geochimica et Cosmochimica Acta*, 323, 164-182,
1540 <https://doi.org/10.1016/j.gca.2022.02.012>, 2022.

1541 Toma, J., Creaser, R. A., Card, C., Pana, D., Dufrane, A., and Li, L.: Nuna supercontinent assembly linked to
1542 carbon cycling in shear zones 1.9-1.7 billion years ago, *Nat. Geosci.*, 17, 1038-1045,
1543 <https://doi.org/10.1038/s41561-024-01519-w>, 2024.

1544 Velde, B. and Christophe, R.: Smectite to illite conversion and K-AR ages, *Clay Minerals*, 31, 25-32, 1996.

1545 Vermeesch, P.: IsoplotR: A free and open toolbox for geochronology, *Geoscience Frontiers*, 9, 1479-1493,
1546 <https://doi.org/10.1016/j.gsf.2018.04.001>, 2018.

1547 Villa, I. M.: Isotopic closure, *Terra Nova*, 10, 42-47, <https://doi.org/10.1046/j.1365-3121.1998.00156.x>, 1998.

1548 Villa, I. M.: Dating deformation: the role of atomic-scale processes, *JGS*, 179, jgs2021-098,
1549 <https://doi.org/10.1144/jgs2021-098>, 2022.

1550 Viswanathan, H. S., Ajo-Franklin, J., Birkholzer, J. T., Carey, J. W., Guglielmi, Y., Hyman, J. D., Karra, S., Pyrak-
1551 Nolte, L. J., Rajaram, H., Srinivasan, G., and Tartakovsky, D. M.: From Fluid Flow to Coupled Processes in
1552 Fractured Rock: Recent Advances and New Frontiers, *Reviews of Geophysics*, 60, e2021RG000744,
1553 <https://doi.org/10.1029/2021RG000744>, 2022.

1554 Walawender, M. J., Gastil, R. G., Clinkenbeard, J. P., McCormick, W. V., Eastman, B. G., Wernicke, R. S.,
1555 Wardlaw, M. S., Gunn, S. H., and Smith, B. M.: Chapter 1: Origin and evolution of the zoned La Posta-type
1556 plutons, eastern Peninsular Ranges batholith, southern and Baja California, in: *Geological Society of America*
1557 *Memoirs*, vol. 174, Geological Society of America, 1-18, <https://doi.org/10.1130/MEM174-p1>, 1990.

1558 Walter, B., Géraud, Y., Bartier, D., Kluska, J.-M., Diraison, M., Morlot, C., and Raisson, F.: Petrophysical and
1559 mineralogical evolution of weathered crystalline basement in western Uganda: Implications for fluid transfer and
1560 storage, *Bulletin*, 102, 1035-1065, <https://doi.org/10.1306/0810171610917171>, 2018.

1561 Wang, C., Alard, O., Lai, Y.-J., Foley, S. F., Liu, Y., Munnikhuis, J., and Wang, Y.: Advances in in-situ Rb-Sr dating
1562 using LA-ICP-MS/MS: applications to igneous rocks of all ages and to the identification of unrecognized
1563 metamorphic events, *Chemical Geology*, 610, 121073, <https://doi.org/10.1016/j.chemgeo.2022.121073>, 2022.

1564 Weinberg, R. F., Wolfram, L. C., Nebel, O., Hasalová, P., Závada, P., Kylander-Clark, A. R. C., and Becchio, R.:
1565 Decoupled U-Pb date and chemical zonation of monazite in migmatites: The case for disturbance of isotope
1566 systematics by coupled dissolution-precipitation, *Geochimica et Cosmochimica Acta*, 269, 398-412,
1567 <https://doi.org/10.1016/j.gca.2019.10.024>, 2020.

1568 Willigers, B. J. A., Mezger, K., and Baker, J. A.: Development of high precision Rb-Sr phlogopite and biotite
1569 geochronology; an alternative to ⁴⁰Ar/³⁹Ar tri-octahedral mica dating, *Chemical Geology*, 213, 339-358,
1570 <https://doi.org/10.1016/j.chemgeo.2004.07.006>, 2004.

1571 Woodhead, J. D. and Hergt, J. M.: Strontium, Neodymium and Lead Isotope Analyses of NIST Glass Certified
1572 Reference Materials: SRM 610, 612, 614, *Geostandards Newsletter*, 25, 261-266, <https://doi.org/10.1111/j.1751->
1573 908X.2001.tb00601.x, 2001.

1574 Worden, J.M., Cumming, G.L., and Baadsgaard, H.: Geochronology of host rocks and mineralization of the
1575 Midwest uranium deposit, northern Saskatchewan, In: Sibbald, T.I., Petruk, W. (Eds.), *Geology of Uranium*
1576 *Deposits*, Canadian Institute of Mining and Metallurgy, 32, 67-72, 1985.

1577 Yardley, B. W. D.: Quartz veins and devolatilization during metamorphism, *JGS*, 140, 657-663,
1578 <https://doi.org/10.1144/gsjgs.140.4.0657>, 1983.

1579 Yardley, B. W. D. and Bodnar, R. J.: Fluids in the Continental Crust, *GeochemPersp*, 3, 1-127,
1580 <https://doi.org/10.7185/geochempersp.3.1>, 2014.

1581 Yeo, G. M. and Delaney, G.: The Wollaston Supergroup, stratigraphy and metallogeny of a Paleoproterozoic
1582 Wilson cycle in the Trans-Hudson Orogen, Saskatchewan, <https://doi.org/10.4095/223746>, 2007.

1583 Zack, T. and Hogmalm, K. J.: Laser ablation Rb/Sr dating by online chemical separation of Rb and Sr in an oxygen-
1584 filled reaction cell, *Chemical Geology*, 437, 120-133, <https://doi.org/10.1016/j.chemgeo.2016.05.027>, 2016.

1585 Zametzer, A., Kirkland, C. L., Barham, M., Hartnady, M. I. H., Bath, A. B., and Rankenburg, K.: Episodic alteration
1586 within a gold-bearing Archean shear zone revealed by in situ biotite Rb–Sr dating, *Precambrian Research*, 382,
1587 106872, <https://doi.org/10.1016/j.precamres.2022.106872>, 2022.

1588